INVESTIGATIONS ON STRUCTURE AND PROPERTIES OF Ge-As-Se CHALCOGENIDE GLASSES

Ting Wang

April 2017

A thesis submitted for
The degree of
Doctor of Philosophy of
The Australian National University

The Laser Physics Centre
Research School of Physics & Engineering
The Australian National University

STATEMENT

I declare that the work presented in this thesis is, to the best of my knowledge, the result of original research. The thesis has not been submitted for a degree or diploma to any other university or institution. Part of the research included in this thesis has been performed jointly with Professor Pierre Lucas.

Signed

Ting Wang

ACKNOWLEDGEMENTS

I would like to sincerely thank my supervisor and advisors, Professor Barry Luther-Davis, Dr. Rongping Wang and Dr. Xin Gai for their guidance, advice and thoughtful comments throughout this work.

I would like to express my thanks to Dr. Zhiyong Yang, Dr. Duk-Yong Choi, Dr. Steve Madden, Dr. Vu Khu for sharing their knowledge and expertise in glass science. I would also like to thank Professor Ian Jackson, Mr Sukanta Debbarma and Mrs Maryla Krolikowska for their help in experiments. Particularly thanks to Professor Pierre Lucas and Mr Ozgur Gulbiten for providing useful samples, valuable suggestions and great assistance on the interpretation of the thermal data.

Thanks to all students who work in the laser physics center: Yi Yu, Pan Ma, Kunlun Yan, Joseph Sudhakar Paulraj and Yue Sun. Thanks to my parents, for their encouragement and great support during my PhD.

TABLE OF CONTENTS

TABLE OF CONTENTS i

LIST OF FIGURES iii

LIST OF TABLES viii

LIST OF ABBREVIATIONS ix

ABSTRACT x

Chapter 1 Introduction 1

- 1.1 Motivation 1
- 1.2 Objectives of the study 3
- 1.3 Outline of the thesis 4

Chapter 2 Background 7

- 2.1 Introduction 7
- 2.2 Structural theories and models of chalcogenide glasses 9
  - 2.2.1 Short-range order 9
  - 2.2.2 Medium-range order 12
  - 2.2.3 Structural relaxation 16
- 2.3 Physical properties of chalcogenide glasses 19
  - 2.3.1 Thermal properties 19
  - 2.3.2 Mechanical properties 21
  - 2.3.3 Optical properties 22
  - 2.3.4 Electrical properties 28
- 2.4 Applications of chalcogenide glasses 32
  - 2.4.1 Optical applications 32
  - 2.4.2 Electronic applications 37
- 2.5 Summary 39

Chapter 3 Structural Study of Ge-As-Se Glasses 40

- 3.1 Introduction 40
- 3.2 Sample preparation and experiments 44
- 3.3 Results 49

3.3.1 Raman scattering spectra of Ge-As-Se glasses 49

3.3.2 EXAFS spectra of Ge-As-Se glasses 56

3.4 Discussion 60

3.5 Conclusions 63

Chapter 4 Thermal Properties of Ge-As-Se Glasses 64

4.1 Introduction 64

4.2 Experiments 67

4.3 Results 68

4.4 Discussion 73

4.4.1 Liquid, fragility and stoichiometry 73

4.4.2 Fragility and structural relaxation in glasses 77

4.4.3 Absence of an intermediate phase 80

4.5 Conclusions 82

Chapter 5 Elastic Properties of Ge-As-Se Glasses 83

5.1 Introduction 83

5.2 Experiments 86

5.3 Results 88

5.4 Discussion 93

5.5 Conclusions 96

Chapter 6 Optical Properties of Ge-As-Se Glasses 98

6.1 Introduction 98

6.2 Experiments 103

6.3 Results 107

6.4 Discussion 117

6.4.1 Linear optical properties of Ge-As-Se glasses 117

6.4.2 Nonlinear optical properties of Ge-As-Se glasses 119

6.5 Conclusions 124

Chapter 7 Conclusions and Future Work 125

7.1 Summary of results 125

7.2 Suggestions for future work 129

Publications 131

References 132

LIST OF FIGURES

Figure 2.1. Schematic illustration of coordination polyhedra and relevant parameters. i - origin atom; j, k - nearest neighbors around atoms of type i. 10

Figure 2.2. Correlations between pairs of dihedral angles for neighboring bonds in covalent networks. Dihedral angle ϕ is a structural parameter which defined as the relative angle of rotation between two connected polyhedra units. θ represents bond angle 14

Figure 2.3. Enthalpy as a function of temperature for glass-forming process. 18

Figure 2.4. Transmission spectra for several oxide and chalcogenide glasses (2-3 mm thick) 22

Figure 2.5. Schematic diagram of the absorption curve of amorphous materials........ 24

Figure 2.6. Schematic of two photon absorption. 28

Figure 2.7. Characterization of chalcogenide glasses as glasses and semiconductors in comparison with other materials. As shown on the horizontal axis, the atom bonding structure becomes more rigid in the order of organic polymers, chalcogenide and organic glasses. Semiconductor properties, *e.g.* carrier mobility, become better in the order of organic, glassy, amorphous and crystalline semiconductors. 29

Figure 2.8. Schematic density of states N(E) for amorphous semiconductors. (a) The Davis-Mott model; (b) The modified Davis-Mott model; (c) The Cohen-Fritzsche-Ovshinsky (CFO) model; (d) The small polaron model. E_c and E_v represent the energies which separate the ranges where the states are localized and extended. E_f represents Fermi energy. 30

Figure 3.1. Schematic diagram of the x-ray absorption process 43

Figure 3.2. Normal setup used for preparing sealed quartz ampoules under vacuum. 45

Figure 3.3 Schematic of EXAFS experiment setup. 46

Figure 3.4. Glass formation domain of the $Ge_xAs_ySe_{100-x-y}$ ternary system showing the 19 compositions investigated by Raman spectroscopy. The red, blue and magenta dots

correspond to compositions with high, intermediate and low Se content, respectively. Five stoichiometric compositions are depicted by black dots.......................................47

Figure 3.5. Normalized Raman spectra of non-stoichiometric bulk glasses. The vertical dashed lines (from left to right) are drawn to indicate the Raman shift at 197 cm^{-1}, 230 cm^{-1}, 240 cm^{-1} and 255 cm^{-1}. 49

Figure 3.6. Normalized Raman spectra of glasses with stoichiometric compositions. The vertical dashed lines (from left to right) are drawn to indicate Raman shift at 197 cm^{-1}, 213 cm^{-1} and 230 cm^{-1}..50

Figure 3.7. Decomposed Raman spectra for $Ge_{10}As_{10}Se_{80}$ and $Ge_{21}As_{30}Se_{49}$ glasses. Black lines represent experimental data, red lines are fitted spectra and the rest colored lines are the decomposed Gaussian curves. 52

Figure 3.8. Raman vibrational modes (a) and relative intensity of two bands (b) as a function of departure from stoichiometry in atomic percent of selenium for Se-rich glasses. Band at 235 cm^{-1} and 250 cm^{-1} correspond to contributions from helical Se-chains and meandering Se-chains respectively..52

Figure 3.9. Relative intensities of corner-sharing and edge-sharing $GeSe_{4/2}$ as a function of Germanium content. The inset is the ratio of the scattering intensity at 195 - 215 cm^{-1} to that at 227 cm^{-1} as a function of Ge/As ratio. The dotted line is a linear fitting result..54

Figure 3.10. Relative intensities of three vibrational modes as a function of Germanium content for Se-poor glasses derived from the decomposed Raman spectra. 54

Figure 3.11. Decomposed Raman spectra for $Ge_{18.75}As_{17.5}Se_{63.75}$ and $Ge_{31.25}As_{2.5}Se_{66.25}$ glasses. Black lines represent experimental data, red lines are fitted spectra and the rest colored lines are the decomposed Gaussian curves.........................55

Figure 3.12 Relative intensities of structural units containing homopolar bonds as a function of Ge/As ratio for stoichiometric glasses..55

Figure 3.13. Magnitudes of the Fourier transform without phase correction of k^3-weighted EXAFS spectra at (a) Ge *K*-edge, (b) As *K*-edge and (c) Se *K*-edge..........57

Figure 3.14. Backtransformed first shell of Fourier transform k^3-weighted EXAFS spectra at (a) Ge, (b) As and (c) Se *K*-edge and experimental fit. Solid lines represent

experimental data and dot lines correspond to fitting results..58

Figure 4.1. Typical DSC curve for a multicomponent chalcogenide glass..................66

Figure 4.2. Glass formation domain of the $Ge_xAs_ySe_{100-x-y}$ ternary system showing the 34 compositions investigated in this study, color-coded according to their mean coordination number. Five stoichiometric compositions are marked as solid circles with horizontal lines through them. 68

Figure 4.3. (a) DSC curves of a $Ge_{6.25}As_{32.5}Se_{61.25}$ glass obtained at different heating rates after cooling at the same rate from far above T_g. (b) Plot of ln Q as a function of $1000/T_g$, showing the linear regression used to obtain E_a for the following glass compositions: $Ge_{10}As_{10}Se_{80}$ ($<r> = 2.30$), $Ge_{10}As_{20}Se_{70}$ ($<r> = 2.40$), $Ge_{17.5}As_{11}Se_{71.5}$ ($<r> = 2.46$) and $Ge_{22.5}As_5Se_{72.5}$ ($<r> = 2.50$). 70

Figure 4.4. T_g as a function of mean coordination number at heating/cooling rate of 10K/min. 70

Figure 4.5. E_a (a) as a function of mean coordination number and (b) as a function of departure from stoichiometry in atomic percent of selenium. 72

Figure 4.6. Fragility index as a function of (a) mean coordination number and (b) departure from stoichiometry in atomic percent of selenium. 72

Figure 4.7. (a) Schematic illustration of an energy landscape; (b) Schematic illustration of the topographic distinction between energy landscapes for strong and fragile glass formers. The potential energy increases in the vertical direction, and the horizontal direction represents all configurational coordinates. 76

Figure 4.8. (a) Schematic representation of three hypothetical glass formers based on a modified VTF equation with *m* ranging from 16 to 200; (b) Variation of the equilibrium excess entropy below T_g in comparison to the value frozen at T_g showing the build up of the driving force for relaxation for glass formers of different *m*. 79

Figure 5.1. The schematic illustrations for the pulse echo overlap ultrasonic method. 86

Figure 5.2. Density (a) and molar volume (b) of $Ge_xAs_ySe_{100-x-y}$ glasses as a function of mean coordination number. The red, green, cyan, blue, magenta, violet, orange and wine dots correspond to $<r> = 2.30, 2.40, 2.50, 2.55, 2.60, 2.70, 2.72$ and 2.80,

respectively. Black dots correspond to random compositions. Open dots with crosses and with horizontal lines correspond to $Ge_xAs_{10}Se_{90-x}$ and $Ge_xAs_{20}Se_{80-x}$ system respectively. Open stars correspond to average density for all the glasses over an <*r*> space of 0.1. The solid lines are a guide for the eyes. 89

Figure 5.3. The shear modulus, Young's modulus and bulk modulus of $Ge_xAs_ySe_{100-x-y}$ glasses. The solid lines correspond to polynomial least-squares fitting results. 90

Figure 5.4. The shear modulus, Young's modulus and bulk modulus of $Ge_xAs_{10}Se_{90-x}$ and $Ge_xAs_{20}Se_{80-x}$ glasses. 92

Figure 5.5. Poisson's ratio of $Ge_xAs_ySe_{100-x-y}$ glasses as a function of mean coordination number. Dashed lines are guides to the eyes. 92

Figure 6.1. Schematic of Z-scan setup 101

Figure 6.2. Schematic of prism coupler measurement for bulk material. 104

Figure 6.3. Transmission curves as a function of wavelength for (a) $Ge_xAs_{10}Se_{90-x}$ and (b) $Ge_xAs_{20}Se_{80-x}$ glasses. The insert graph shows a close-up view of the data........... 108

Figure 6.4. Linear refractive index (n_0) of $Ge_xAs_ySe_{100-x-y}$ glasses as a function of mean coordination number at 1550 nm. The red, green, blue, cyan, dark yellow, magenta, pink, violet, orange and wine dots correspond to <*r*> = 2.30, 2.40, 2.45, 2.50, 2.55, 2.60, 2.70, 2.65, 2.70, 2.72 and 2.80, respectively. Black dots correspond to random compositions. Open dots with crosses and with horizontal lines correspond to $Ge_xAs_{10}Se_{90-x}$ and $Ge_xAs_{20}Se_{80-x}$ system respectively. Open stars correspond to average linear refractive index for all the glasses over an <*r*> space of 0.1. The solid line is a guide for the eyes. 108

Figure 6.5. Linear refractive index of $Ge_xAs_ySe_{100-x-y}$ glasses as a function of the ratio of As content to Ge content. The solid line is a guide for the eyes. 111

Figure 6.6. Normalized transmittance obtained from closed aperture and open aperture Z-scan measurement for $Ge_{11.5}As_{24}Se_{64.5}$ for different intensities at 1550 nm. The open circles and squares are experimental data and the solid lines are theoretical fitting..... 113

Figure 6.7. Nonlinear refractive index (n_2) as a function of mean coordination number (<*r*>) for $Ge_xAs_ySe_{100-x-y}$ system. Open stars correspond to average values of nonlinear refractive index over an <*r*> space of 0.1. The solid line is a guide for the eyes. 113

Figure 6.8. Plots of $(\alpha h\nu)^{1/2}$ versus $h\nu$ for five films. 114

Figure 6.9. (a) Typical open aperture traces and their corresponding fit to a numerical model for $Ge_{12.5}Sb_{20}Se_{67.5}$ for different intensities at a wavelength of 1250 nm. (b) The inverse of transmittance for $Ge_{12.5}Sb_{20}Se_{67.5}$ is plotted against irradiance at different wavelengths. Theoretical fits are shown in solid lines. 114

Figure 6.10. Plot of n_2 (a) and β (b) as a function of normalized photon energy for the glasses listed in Table 6.3. The solid lines are a guide for the eyes. 117

Figure 6.11. (a) The variation of the third order nonlinear susceptibility ($\chi^{(3)}$) as a function of linear susceptibility ($\chi^{(1)}$). Solid line is the theoretical fitting curve basing on Equation (6.8). (b) Plot of the nonlinear refractive index (n_2) as a function of linear refractive index (n_0) and the theoretical fitting curve according to Equation (6.9). 120

Figure 6.12. (a) Normalized nonlinear refractive index, $n_2 n_0^2 (E_g^{opt})^4$, plotted as a function of normalized photon energy. (b) Normalized two photon absorption, $\beta n_0^2 (E_g^{opt})^3$, plotted as a function of normalized photon energy. The solid line is fitting according to Dinu's model and the dashed line is Sheik- Bahae's model 123

LIST OF TABLES

Table 2.1. Typical time scale of the nonlinear response for several physical processes. 27

Table 2.2. Active and passive applications of chalcogenide glass optical fibers. 33

Table 3.1. Compositions and respective mean coordination number (<*r*>), the extent of Se-rich/Se-poor for $Ge_xAs_ySe_{100-x-y}$ glasses investigated by Raman spectroscopy. 48

Table 3.2. Assignment of Raman modes for $Ge_xAs_ySe_{100-x-y}$ glasses. 51

Table 3.3. Ge, As and Se *K*-edge EXAFS structural parameters (the coordination number *N*, the bond length *R* and Debye-Waller factor σ^2) for $Ge_xAs_ySe_{100-x-y}$ glasses..60

Table 4.1. Compositions and respective mean coordination number (<*r*>), glass transition temperature (T_g), activation energies (E_a) and fragility index (*m*) for $Ge_xAs_ySe_{100-x-y}$ glasses..71

Table 5.1. Compositions and respective mean coordination number (<*r*>), density (ρ), elastic moduli and molar volume (V_m) of $Ge_xAs_ySe_{100-x-y}$ glasses..................................91

Table 6.1. Nonlinear properties of chalcogenide glasses 102

Table 6.2. Compositions and respective mean coordination number (<*r*>), linear refractive index (n_0), As/Ge ratio and nonlinear refractive index (n_2) of all glass samples. 109

Table 6.3. Compositions, optical bandgap (E_g^{opt}), nonlinear optical properties (n_2, β and FOM) of five selected chalcogenide glasses. 116

LIST OF ABBREVIATIONS

CONM	Chemically Ordered Network Model
DFWM	Degenerate Four-wave Mixing
DSC	Differential Scanning Calorimetry
EXAFS	Extended X-ray Absorption Fine Structure
FOM	Figure of Merit
FSDP	First Sharp Diffraction Peak
IP	Intermediate Phase
LP	Lone-pair
LRO	Long-range Order
MIR	Mid-infrared
MRO	Medium-range Order
MZI	Mach-Zehnder interferometry
MDSC	Temperature-modulated Differential Scanning Calorimetry
NQR	Nuclear Quadrupole Resonance
RDF	Radial Distribution Function
RCNM	Random Covalent Network Model
SC	Supercontinuum
SRO	Short-range Order
SBS	Stimulated Brillouin Scattering
TS	Threshold Switching
THG	Third-harmonic Generation
TPA	Two Photon Absorption
VTF	Vogel-Fulcher-Tamman
XPM	Cross Phase Modulation
XPS	X-ray Photoelectron Spectroscopy

ABSTRACT

Germanium-Arsenic-Selenium chalcogenide glasses are considered as good candidates for photonic applications due to their excellent transparency in the infrared range and high optical nonlinearities. A deep understanding of composition-structure-property relationship in Ge-As-Se ternary system is thus becoming increasingly important, which can serve as a guideline for materials selection.

In this work, the structure and various physical properties of $Ge_xAs_ySe_{100-x-y}$ bulk glasses have been systematically investigated. Raman spectra and EXAFS measurements reveal that chemically ordered network model can be applied to Selenium-rich glasses, but fails to explain bonding characterization of Selenium-poor compositions. Atomic arrangements are more sensitive to the changes in chemical compositions.

A tight association between the fragility and the deviation from stoichiometry has been found in the Ge-As-Se system by differential scanning calorimetry. It is shown that chemical compositions with the lowest values of fragility index are far less likely to incur structural relaxation. Those strong glasses are normally chosen as ideal materials for fabrication of stable photonic devices.

The variation of density and elastic modulus as a function of mean coordination number both show two transition thresholds, which correlate with floppy-to-rigid phase transition and 2D-to-3D structure transition respectively. The results provide clear evidence that some physical properties of Ge-As-Se chalcogenide glasses are significantly determined by their mean coordination numbers, but could be further tuned by the chemical compositions.

The detailed optical investigation shows that the generalized Miller's rule is a simple but effective approach to estimate the nonlinearities of a broad variety of chalcogenide glasses. Nonlinear properties of these materials exhibit strong dependence upon their optical bandgap in the near infrared. It seems that the highest nonlinearity at telecommunications wavelengths is predictable in chalcogenide glasses.

Chapter 1

Introduction

1.1 Motivation

Over the past several decades, the study of amorphous materials whose structures are characterized by the lack of periodic long-range order has drawn much attention in the field of condensed matter physics. Amorphous materials used in electronic through to photonic devices play an increasingly fundamental role in modern technologies. Among these, glasses are the primary materials employed in the vast majority of optical systems due to their broad optical transparency, lower production costs and their versatility. Chalcogenide glasses are a family of non-oxide inorganic glasses and have found a progressively wide utilization in civil, medical and military areas, including RW-DVDs, biochemical sensors and thermal imaging devices [1]. More importantly, their high optical nonlinearities and wide transparency windows in the infrared make these glasses excellent materials for photonic applications [2]. Since the practical significance of the chalcogenide platform is steadily growing, it is of vital importance to investigate their various physical properties including thermal, mechanical and optical behaviors of various chalcogenide glass systems, since this is critical to the discovery of optimized chemical compositions for the future specific engineering applications.

Typical chalcogenide glass systems, $As_2S(Se)_3$ and $GeS(Se)_2$ for example, have been extensively studied [3-6] and successfully used to fabricate optical fibers and planar waveguides [2,7-11]. However, these binary glasses suffer from significant drawbacks such as low glass transition temperatures or limited nonlinearities. It has been found, however, that more desirable materials for future photonic devices which have better thermal and optical properties can be obtained by adding a third element to these binary compounds [12,13]. Among those, the Ge-As-Se system is of particular interest because it has an extremely large glass forming region [14,15], and this is ideal for clarifying the fundamental composition-structure-property relationship in ternary chalcogenide glasses. Additionally, the Ge-As-Se system exhibits stronger covalent bond nature due to the similarity of the atomic mass, the atomic radius and the electronegativity of the constituent elements [16]. This characteristic provides a good opportunity to test the validity of structural theories for covalently-bonded glasses, such as the rigidity percolation model [17,18].

While certain Ge-As-Se compositions have been identified as a potential candidate for various applications [19-21], general knowledge of the glass structure for this system is still not well established. Traditional X-ray diffraction techniques are limited in providing the most precise structural information due to the absence of periodic atomic arrangements in amorphous materials. In addition, the formation of chemical bonds in such chalcogenide glasses is very sensitive to the preparation methods and the form of the materials. In view of these, a systematic study of Ge-As-Se chalcogenide bulk glasses has been conducted in this work. Bulk glass samples have been chosen because they are more stable, easier to fabricate and have better consistency compared, for example, with material in the form of thin films. It is expected that the results of the compositional dependence of different physical properties of bulk glasses will be helpful in understanding the evolution of the microstructure of Ge-As-Se ternary glasses as well as identifying novel materials with optimum properties for the fabrication of GeAsSe-based photonic devices.

1.2 Objectives of the study

This work builds upon previous experience in studying structural and physical properties of chalcogenide glasses. A detailed investigation focuses on the basic, long-lasting and controversial arguments in chalcogenide glass materials science. This work is particularly aimed at answering following questions:

1. How do chemical compositions and structures affect variations of different physical properties within Ge-As-Se system?
2. Which factor, chemical effects or topological effects, is more effective in controlling the diverse physical properties of ternary Ge-As-Se glasses?
3. Is it possible to predict any property changes in Ge-As-Se glass family?
4. What would be the probable applications of these bulk materials in the coming decades?

By investigating a large number of compositions within the glass-forming range, the information about correlation between microstructures, compositions and corresponding physical properties can be elucidated, which would give an insight into the tunability of the characteristics of Ge-As-Se ternary chalcogenide glass system and aids the selection of the best materials for specific applications.

1.3 Outline of the thesis

This thesis describes the characterization of structural, thermal, elastic and optical properties of Ge-As-Se bulk chalcogenide glass prepared by conventional melt-quenching method. The layout is divided into seven chapters.

After a brief introduction to the motivation and objectives behind this work in **Chapter 1**, Chapter **2** introduces essential background knowledge of chalcogenide glasses which will be referred to in the following chapters, including a summary of their research history, the structural theories and models, some important physical parameters for chalcogenide glasses, as well as primary applications of these materials.

Chapter 3 focuses on the structural study of selected Ge-As-Se glasses using Raman spectroscopy and Extended X-ray Absorption Fine Structure (EXAFS) spectroscopy. The fabrication procedure of the glass samples and a list of all studied compositions are provided. The validity of several structural models was also demonstrated. An attempt is also made to estimate the possible bond arrangement and compositional effects in this system of glasses.

Chapter 4 reports the thermodynamic properties of a variety of Ge-As-Se glasses. The compositional dependences of the glass transition temperature T_g, the activation energy for structural enthalpy relaxation E_a and the fragility index m were measured by Differential Scanning Calorimetry (DSC). The resulting trends are used to rationalize previous empirical observations on both relaxation and photostability for this family of glasses.

Chapter 5 discusses the mechanical properties of several groups of Ge-As-Se glasses. After directly measuring densities ρ as well as velocities of longitudinal and transverse sound waves respectively, the shear modulus G, Young's modulus E, bulk modulus K and Poisson's ratio v were calculated. The results are used to examine topological and chemical threshold behavior of the Ge-As-Se glass system, which provide important information about microstructure and mechanical strength.

Chapter 6 characterizes the linear and nonlinear optical properties of a series of Ge-As-Se glasses at 1550 nm. The linear refractive index n_0, the nonlinear refractive index n_2 and the nonlinear absorption coefficient β are presented. The spectral dispersion of the nonlinearities of five specific chalcogenide compositions - As_2S_3, $Ge_{11.5}As_{24}Se_{64.5}$, $Ge_{15}Sb_{10}Se_{75}$, $Ge_{15}Sb_{15}Se_{70}$ and $Ge_{12.5}Sb_{20}Se_{67.5}$ along with their optical bandgaps E_g^{opt} were also investigated from 1150 nm to 1686 nm. The results have been used to quantify trends in the value of nonlinearity as the composition of the glass is changed. The measured dispersion compared with the predictions of two widely discussed models for scaling of the nonlinearity of direct and indirect semiconductors. These provide direct insight into optimizing chalcogenide glass for third order nonlinear photonics.

Finally, **Chapter 7** gives a short conclusion and some suggestions for future work.

Chapter 2

Background

2.1 Introduction

Chalcogenide glasses are an important class of amorphous solids and contain at least one of the chalcogen elements from Group 16 of the Periodic Table. These elements, namely Sulphur (S), Selenium (Se) and Tellurium (Te) (but excluding Oxygen), are normally covalently bonded to network formers mostly from Group 14 (Si, Ge) and Group 15 (P, As and Sb) to form binary, ternary or quaternary glass systems. The resulting glasses are regarded as semiconductors with a bandgap that ranges between 1 and 3 eV [22]. They have outstanding properties as infrared optical materials because the large masses of their constituent atoms cause the vibrational energies of the chemical bonds to be low and this leads to broad transparency that extends across much of the middle infrared (up to ~ 20 μm for Te-based glasses) [23]. Their chemical bonds are highly polarizable and, therefore, they also possess large linear and nonlinear refractive indices [24] and this is advantageous for some of the current applications in photonics [25]. A widely studied characteristic of the chalcogenides is their photosensitivity - the tendency for the chemical bonds to change when exposed to light at a wavelength close to their band edge. This can result in changes in the macroscopic properties of the material such as the band-gap and refractive index which, like the photosensitive effects in Silica-Germania glasses, can be used to inscribe optical structures into glass films (*e.g.* diffraction gratings) which again can be used in some specific photonic devices [24].

In contrast with oxide glasses, which have a long history, it was only at the end of 19th century that vitreous selenium and arsenic sulfide and selenide were first synthesized. They did not immediately attract much scientific interest but this changed in the last century when, at the beginning of the 1950s, Frerichs reported the optical properties of As_2S_3 and related glasses highlighting their potential as infrared optical materials [26,27]. This stimulated research into the chemical and physical properties of As_2S_3 glass for optical elements [28]. From the 1960s, the range of glass compositions had been extended to include ternary systems that resulted in infrared optical materials with higher softening temperatures and longer wavelength cut-off [29,30]. Meanwhile, the distinctive semiconducting features of chalcogenide glasses had been discovered in Russia [31,32] and this eventually led to chalcogenides emerging as attractive candidates for solar cells, most notably the Copper-Indium-Gallium-Selenide (CIGS) system which remains the subject of commercial development today [33].

In 1968, the pioneering work of Ovshinsky led to the invention of phase change memories based on reversible switching of the structure of some chalcogenides between the amorphous and polycrystalline states [34]. During the period from the 1970s to 1980s, chalcogenide glasses were, thus, being developed for memory devices based on this switching effect; for xerography based on their photoconductive properties [35,36]; and for infrared optics. Today most of these applications remain the subject of on-going research or commercial development, and in particular they motivate the search for a better understanding of structure-property relations for this diverse range of glasses [7,37-39].

2.2 Structural theories and models of chalcogenide glasses

A necessary prerequisite to fully understand the correlation between the physical properties and composition of amorphous chalcogenide materials is the determination of their chemical bonding on the atomic scale. Unfortunately, this is neither simple nor easy in these noncrystalline materials because the spatial arrangement of the atoms lacks order. In fact, the atomic arrangement in amorphous chalcogenides falls somewhere between that of an ideally periodic and a completely random structure. As a result, it is necessary to characterize the structural properties based on the different length scales: short-range order (SRO) in the range 2 - 5 Å; medium-range order (MRO) in the range 5 - 20 Å; and long-range order (LRO) for length ≥ 20 Å (no long-range order present in the amorphous materials by definition) [40].

2.2.1 Short-range order

The short-range order of chalcogenide glasses which are covalently-bonded amorphous materials showing highly directional bonding can be described by coordination polyhedra (Figure 2.1). In other words, topological SRO can be determined by three parameters, which are the number of nearest neighbors (N); the nearest neighbor bond length (R) and the bond angle (θ). These short-range parameters can be obtained by calculating the radial distribution function (RDF) from X-ray diffraction patterns. Furthermore, chemical SRO, involving the formation of homopolar bonds or the formation of nonbridging ligands, cannot be neglected when the glass compositions are non-stoichiometric or more complex, such as systems containing modifier ions [41,42].

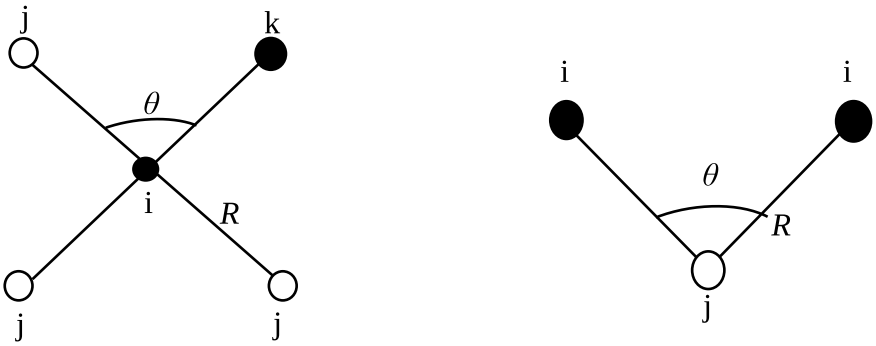

Figure 2.1. Schematic illustration of coordination polyhedra and relevant parameters. i - origin atom; j, k - nearest neighbors around atoms of type i.

Given the above-mentioned parameters which are used to describe topological and chemical SRO, some structural models concerning the atomic bonding within a short distance have been proposed [43,44]. Two well-known models are the random covalent network model (RCNM) and the chemically ordered network model (CONM), both of which developed from Zachariasen’s pioneering random network theory for oxide glasses [45]. They also both assume that the coordination number (r) of constituent atoms in covalent chalcogenide glasses satisfy the 8-N rule [46], where N is the number of valence electrons of a particular atom and then r = 8 - N. In the RCNM [47,48], the types of bond follows a statistical distribution, viz., their abundance is determined only by their coordination number and the fraction of each type of atom and the probability of forming each kind of bond is supposed to be equal. In contrast, the CONM takes preferential ordering effects into consideration [49]. It favors the atomic arrangement that leads to the lowest energy which means, for example, that the formation of heteropolar bonds (formed between two different atoms) is preferred over homopolar bonds (formed between two identical atoms). This chemical ordering is maximized at the stoichiometric compositions, also known as the chemical thresholds of the system at which only heteropolar bonds are expected to present. It should be noted that the connectivity between different coordination polyhedra are not considered in these two models; therefore, they are not really suitable for explaining the medium-range structure in chalcogenide glasses.

Phillips proposed a mechanical model after considering the combinational effects of short-range order and network structure [50]. In this model, the mean coordination number ($<r>$) was introduced as:

$$<r> = \sum_i x_i r_i \tag{2.1}$$

where x_i is the concentration of atom i; r_i is the coordination number of atom i which obeys the 8-N rule. Two types of interatomic forces, *i.e.* bond-stretching forces (α) and bond-bending forces (β), serve as mechanical constraints which are described by valence force fields. The total number of topological (rigid) constraints per atom is then calculated as $N_{co} = \alpha + \beta$. Mechanical equilibrium is attained when the number of constraints equals to the number of degree of freedom per atom ($N_d = 3$) in a three dimensional structure, in which case the glass-forming tendency is optimized where the glass network is defined as ideally constrained or isostatic. If $N_{co} < N_d$, the network is defined as underconstrained or floppy; if $N_{co} > N_d$, the network is defined as overconstrained or rigid. This idea was further improved by Thorpe on the basis of zero frequency modes [51]. For a *r*-coordinated atom ($r \geq 2$), the number of bond-stretching constraints is $r/2$ (each bond constraint is shared by two atoms) and the number of bond-bending (angular) constraints is $2r - 3$ rather than $r(r - 1)/2$ as given by Phillips. (A two-coordinated atom has only one angular constraint. Adding each additional bond will generate two more constraints.) Under these circumstances, for a network with mean coordination number $<r>$, the total number of topological constraints per atom can be written as:

$$N_{co} = \frac{<r>}{2} + (2<r> - 3) \tag{2.2}$$

Combining Phillips' and Thorpe's concepts, an important value, $<r> = 2.40$, also known as rigidity percolation threshold, is therefore obtained. For glasses having low $<r>$, the rigid regions are isolated in the network. The volume of these rigid regions increase with increasing $<r>$ until $<r> = 2.40$, where rigid regions percolate through the glass matrix and the structure is believed to become stable. Several studies of the physical properties of chalcogenide glasses have supported this Philips-Thorpe rigidity percolation theory [52-54]. These models contain no complicated calculations or quantum mechanisms, but still provide a solid foundation for understanding the structural character of chalcogenide glasses.

2.2.2 Medium-range order

Medium-range order has received increasing attention in terms of its importance of understanding the physical properties of chalcogenide glasses. To date, no clear consensus exists over the definition of MRO, but in principle, MRO refers to the structural arrangement beyond the nearest-neighbor atoms. In practice, Elliott divided MRO into three subclasses, corresponding to progressively increasing length scales [40]. Short range MRO (≤ 5 Å) involves the type of connection between the coordination polyhedra which are used to define SRO, as well as their relative orientation. Such orientational correlation can be well-described by a structural parameter known as dihedral angle (ϕ, see Figure 2.2). At the next length scale (5 - 10 Å), intermediate range MRO is associated with five-body correlations, in other words, triplet correlations between adjacent polyhedral as shown in Figure 2.2. It normally features the emergence of larger structural aggregation, *e.g.* rings or clusters of atoms. Lastly, long range MRO (10 - 20 Å) correlates with the local dimensionality of a covalently-bonded amorphous network. The difference in dimension arises from either the type of connection between coordination polyhedra or network depolymerization. There is a consensus that the characteristics of medium-range order can be reflected by the presence of the first sharp diffraction peak in X-ray diffraction patterns, but the actual atomic configuration is still dubious. The boson peaks in the low wavenumbers of Raman scattering spectra (between 10 cm^{-1} and 100 cm^{-1}) can also provide structural information in MRO. This spectral feature has universality in amorphous materials. The behavior of the broad peak reflects the density of states. The structural correlation range (SCR = 2σ), a characteristic micro-region which is possible to signify certain medium-range structures, can be described by [55]:

$$2\sigma \approx \frac{v}{\pi c \omega_{\max}} \tag{2.3}$$

where v is the velocity of sound in the studied glasses, c is the velocity of light and $\omega_{\max}$

is the frequency of the maximum intensity of the boson peak.

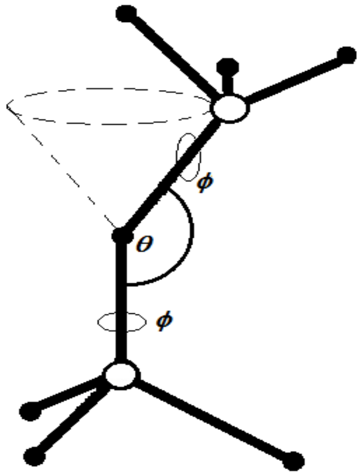

Figure 2.2. Correlations between pairs of dihedral angles for neighboring bonds in covalent networks. Dihedral angle ϕ is a structural parameter which defined as the relative angle of rotation between two connected polyhedra units. θ represents bond angle [40].

In contrast with SRO, the essence of MRO remains a highly controversial topic because there are no widely-applicable experimental probes which can directly specify structural information on such a scale. One possible method for studying medium-range structure is to firstly propose a structural model, then verify its applicability by interpreting structural data and macroscopic properties, through which the model could be confirmed, require modification, or be completely discarded.

The distorted layer model, proposed by Vaipolin and Porai-Koshit, was first applied to amorphous $As_2S(Se)_3$ [56]. The model is based on the notion that glasses consist of layered structures with finite thickness similar to those in their crystalline counterparts but corrugated. The deformed layers are bonded together by Van der Waals forces. This concept was further developed by Phillips, who put forward a chalcogenide-bordered raft model [57]. In 1989, Tanaka extended the Phillips-Thorpe models to include the influence of inter-cluster forces on medium-range order [58]. The constraint is expressed as $N_{co} = \langle r \rangle/2 + (\langle r \rangle - 1)$, where the first variable on the right-hand side of the equation represents radial constraints, the angular constraints are calculated as $\langle r \rangle - 1$ due to the assumption of medium-range configuration. Another structural phase transition was observed at a critical mean coordination number ($\langle r \rangle = 2.67$), wherein two-dimensional layer structures change to a three-dimensional cross-linked network.

During this century, knowledge of the MRO in chalcogenide glasses has deepened, which is reflected by the progress of the concept of the polymeric polymorphous-crystalloid structure of glass and the introduction of the micro-paracrystalline model. The micro-paracrystalline model [59] indicate that the most stable crystallographic planes are preserved in the chalcogenides but with ill-defined packing, which gives rise to structural effects of medium-range order. The main concept of polymeric polymorphous-crystalloid structure can be demonstrated as follows [60]:

1. The formation of a vitreous substance involves the process of generation, mutual transformation and copolymerization of structural fragments of various polymorphous modifications (PMs) of a crystal substance without LRO (crystalloids). The crystalloid is a fragment of a crystalline structure consisting of a group of atoms connected by chemical bonds.

2. In every non-crystalline substance there are two or more SROs, two or more intermediate-range (medium) orders (IROs), and there is no LRO.

3. Glass structure is not absolutely continuous, and there are separate broken chemical

bonds and other structural defects.

Also worth mentioning is the discovery of the intermediate phase (IP) in chalcogenide glasses [61]. Temperature-modulated Differential Scanning Calorimetry (MDSC) and Raman scattering experiments show that with increasing <*r*>, glasses actually undergo two phase transitions instead of one fixed at <*r*> = 2.40 as predicted by the Phillips-Thorpe models. Two phase transitions, also known as the rigidity and stress transition, separate the glass network into three zones: floppy; rigid but unstressed; and stressed rigid. Glass compositions located between these two transitions are defined as the intermediate phase, which is assumed to be self-organized and non-aging. It has been found that IP in binary Ge_xSe_{1-x} glasses is over an <*r*> range of 2.40 - 2.50 [62], while it appears over a range of <*r*> between 2.27 and 2.42 in $Ge_xAs_xSe_{1-2x}$ glasses [63]. The width of intermediate phase (a limited compositional region where the network is elastically rigid but stress-free) depends on the chemical compositions and reflects glass structure at short-range as well as medium-range distances [64]. Although there is some evidence from numerical simulations and experimental measurements to support this theory [64], the existence of the IP is still open to question in chalcogenide glasses [65].

2.2.3 Structural relaxation

The glass-forming process (Figure 2.3) involves fast cooling of a liquid and a commensurate increase in the viscosity of that liquid. If a glass-forming liquid is cooled rapidly enough, crystallization can be avoided as the temperature is lowered below the melting point T_m. A supercooled liquid is thus obtained. When the temperature approaches the glass transition temperature (T_g), the time for structural rearrangements in the liquid becomes roughly analogous with the experimental time scale (a macroscopic parameter which is inversely proportional to the rate of cooling) due to the sharp increase in the viscosity of the liquid. Therefore, the system starts to diverge from thermal equilibrium and the liquid starts to undergo a glass transition. At a temperature well below T_g, the structural movements are completely frozen and a glass is eventually formed. Glasses are in a state of thermodynamic non-equilibrium. If an external thermodynamic driving force, *e.g.* the temperature, is changed, a glass in the transformation region tends to evolve towards the equilibrium state by the reorientation of molecular clusters. This temperature-sensitive slow process is commonly referred to as structural relaxation. Structure relaxation can occur when glasses are heated, cooled or held isothermally at a temperature near or below T_g, and is manifested by time-dependent changes in macroscopic physical properties, such as heat capacity (C_p), enthalpy (H) and volume (V) [66].

Whilst no single universal explanation has been found concerning the mechanism of structural relaxation, several kinds of models have been suggested to describe this phenomenon. The Vogel-Fulcher-Tamman (VTF) equation [67] successfully interprets the relationship between relaxation time (τ) and temperature for many glass-forming systems. This temperature dependence of the structural relaxation time has also been derived from a free-volume model [68]. The Gibbs-Dimarzio theory [69] and a modified Adam-Gibbs model [70] describe structural relaxation from a thermodynamic perspective. Kinetic models, such as the order parameter model [71] and the kinetic Ising model [72], link the evolution of physical properties with time in amorphous materials. The Tool-Narayanaswamy-Moynihan (TNM) model [73] is one of the most widely used phenomenological models, which indicates that the structural relaxation time depends not only on temperature but also on the instantaneous structure of the glass characterized by the fictive temperature (T_f), which corresponds to the temperature of the undercooled liquid having the same structural state as the glass. This model is able to predict the physical properties of glasses subjected to any thermal history. It has been found that structural relaxation is closely correlated with changes in the glass structure, and therefore studying this process could be helpful in selecting the optimum glass compositions with predictable macroscopic properties for different technical applications.

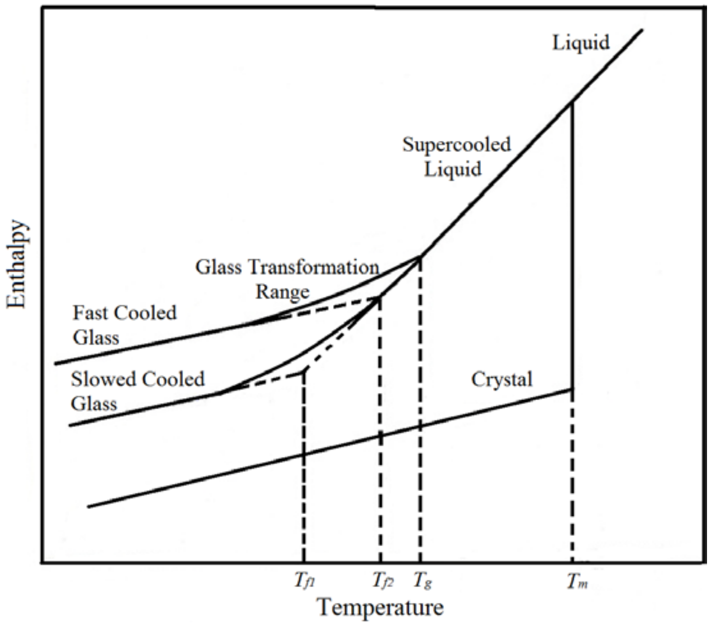

Figure 2.3. Enthalpy as a function of temperature for glass-forming process.

2.3 Physical properties of chalcogenide glasses

2.3.1 Thermal properties

Thermal properties are one of the most widely studied topics in glass science. They can reveal details of the glass structure and have a fundamental role in determining the practicability of a given chalcogenide glass composition for a specific application. They cover a wide range of aspects, including the glass transition and the stability to devitrification.

The glass transition is perhaps the most common and important thermal property of an amorphous material. Although the glass transition has generally been accepted as a relaxation phenomenon instead of a phase transition, the nature of the glass transition is still ambiguous [74-77]. A lot of attention has been paid to the measurement and understanding of the glass transition temperature [78]. The glass transition temperature is that at which a state transformation (supercooled liquid $\leftrightarrow$ glassy solid) takes place in the material. Additionally, some other physical properties, such as the volume and hardness, also undergo a dramatic change at this point. It is widely acknowledged that T_g is not a thermal constant because it varies in magnitude depending upon the particular experimental conditions – the quenching rate of the liquid, for example. To better explore the underlying correlation of T_g with other chemical or physical factors, some empirical relations have been proposed. According to Kauzmann, the glass transition temperature can be estimated as [79]:

$$T_g \approx (2/3)\ T_m \tag{2.4}$$

where T_m is the melting temperature of corresponding crystalline phase (refers to a phase transition in which converts crystalline solid to liquid polymer). An empirical relationship between T_g and mean coordination number: $\ln T_g \approx 1.6 <r> + 2.3$ was first obtained for the covalent glasses in [80]. Following this, a modified Gibbs-DiMarzio equation including the effect of cross-linking was derived for multicomponent chalcogenide glasses as in [81]:

$$T_g = \frac{T_0}{[1-\beta(<r>-2)]} \tag{2.5}$$

where T_0 is the T_g of the non-cross-linked parent chain and β is a system constant. In addition, the linear dependence of T_g and the overall bond energy $<E>$ (related to mean coordination number, the type of bonds, the degree of cross-linking and the bond energy), which can be expressed as $T_g \approx 311(<E> - 0.9)$, demonstrated that the arrangement of the chemical bond is the main factor determining T_g in chalcogenide glasses [82].

When an amorphous solid is heated, it is likely to crystallize. Glass compositions with a low tendency to crystallize are useful for the fabrication of optical fiber, because if crystalline phases are formed in an amorphous matrix they are likely to lead to large scattering losses. By contrast, crystallization is the essential mechanism applied to optical storage devices and to the creation of glass-ceramics. As the viscosity decreases with increasing temperature, the mobility of atoms in a glassy solid will be enhanced. Meanwhile, rearrangement of the chemical bonds between the atoms may also occur, which can lead to crystallization of the glass at a characteristic crystallization temperature (T_c). Similar to glass transition, crystallization is a kind of structural relaxation but exothermic in nature. The difference between the glass transition temperature and the crystallization temperature $\Delta T = T_c - T_g$ can be used to measure the resistance to devitrification of a glassy alloy. As a rule of thumb, $\Delta T = 100$ K is regarded as the minimum requirement for a glass to have good thermal stability.

2.3.2 Mechanical properties

The density (ρ) is an important parameter as it can reflect the atomic structure of a glass. Precise determination of the density is also an essential prerequisite for determining the elastic properties of chalcogenide glasses. The density is normally measured by the Archimedes' method [83]. The accuracy of the data so-obtained can be improved by eliminating air bubbles when the sample is immersed in the liquid; by increasing the sample size; and by using beakers (for the immersion liquid) with a large diameter to minimize edge effects.

The elastic properties are sensitive to both the SRO and MRO in glass materials. The elastic moduli can serve as an indicator of the atomic packing density and the physical strength of each component. By measuring the velocity of the longitudinal sound wave (V_l) and the velocity of transverse sound wave (V_t) along with the density of the glass (ρ), the Young's modulus (E), the shear modulus (G), the bulk modulus (K) and Poisson's ratio (v) can be calculated from the following relationships [84]:

$$E = \rho \frac{3V_l^2 - 4V_t^2}{(V_l/V_t)^2 - 1} \tag{2.6}$$

$$G = \rho V_t^2 \tag{2.7}$$

$$K = \frac{E}{3(1-2\nu)} \tag{2.8}$$

$$\nu = \frac{E}{2G} - 1 \tag{2.9}$$

2.3.3 Optical properties

Chalcogenide glasses are historically known for their high transmittance in the near- and mid-infrared (MIR). The MIR cut-off (Figure 2.4) is determined by the particular chalcogen element that the glass contains and is approximately 11 μm, 15 μm and 20 μm for sulphides, selenides and tellurides, respectively [23]. The linear optical properties of chalcogenide glasses comprise the linear refractive index (n_0); the absorption coefficient (α); and optical bandgap (E_g^{opt}).

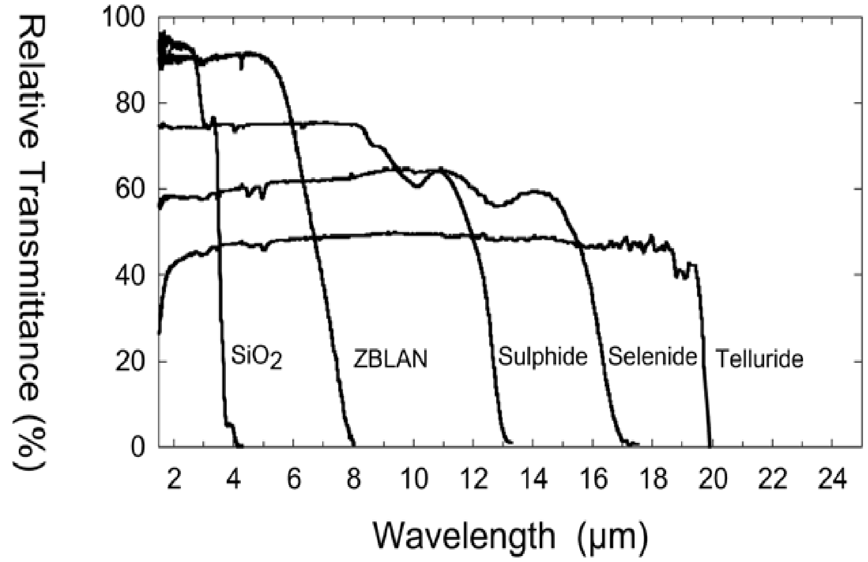

Figure 2.4. Transmission spectra for several oxide and chalcogenide glasses (2-3 mm thick) [23].

The refractive index of a glass is defined as the ratio of the speed of light in vacuum to the speed of light in the glass and this varies with the wavelength of the incident light. Since the refractive index is one of the most basic but important factors when designing an optical system, there have been many experimental and theoretical attempts to find the relationship between n_0 and other properties of glassy materials. It has been found that it is possible to predict values of the refractive index using some simple mathematical expressions. The Gladstone-Dale equation [85], $(n - 1) / \rho = K$ = Constant, is one of the simplest empirical equations that has been used to estimate the refractive index of oxide glasses (n) from their densities (ρ). According to the Wemple-DiDomenico single-oscillator model [86], the dispersion of the refractive index is related to photon energy through the relationship: $n^2 - 1 = E_d E_0 \big/ (E_0^2 - \hbar^2\omega^2)$, where E_d is the dispersion energy, E_0 is the single oscillator energy, and $\hbar\omega$ is the photon energy. Chalcogenide glasses possess relatively large refractive index, normally between 2 to 3. A high refractive index is useful for applications that involve integrated photonic devices since it permits the fabrication of waveguides with a large index contrast between the light core and the surrounding cladding which allows the light to be tightly confined within a small waveguide to enhance the optical intensity and permits the waveguide to be bent with a small radius.

The optical absorption is one of the intrinsic optical properties that determines the transmittance of device made from a chalcogenide glass. The absorption coefficient can be calculated from the transmission spectra of a sample using the following relation:

$$\alpha = \frac{1}{d}\ln\left(\frac{1}{T}\right) \tag{2.10}$$

where d is the thickness of the sample and T is the transmission. A typical absorption curve can be separated into three regions (shown in Figure 2.5). In general, the region of high absorption (Region A, $\alpha \geq 10^4$ cm^{-1}) corresponds to transition across the bandgap of the material where the absorption is governed by Tauc law [87]:

$$\alpha h\upsilon = B(h\upsilon - E_g^{opt})^n \tag{2.11}$$

where $h\nu$ is the incident photon energy, B is the proportional constant, $E_g{}^{opt}$ is the optical band gap and n is the parameter corresponding to the nature of transition. In amorphous solids, in the second intermediate absorption region (Region B, 1 cm^{-1} $\leq \alpha \leq 10^4$ cm^{-1}) exists due to the presence of disorder and defects with the absorption following an exponential dependence, the so-called Urbach relation [88] where:

$$\alpha = \alpha_0 \exp(h\nu / E_U) \tag{2.12}$$

where α_0 is a constant, E_U is the Urbach energy. For weak absorption coefficient (Region C, $\alpha \leq 1$ cm^{-1}), the absorption depends on the preparation, purity and thermal history of the material [89].

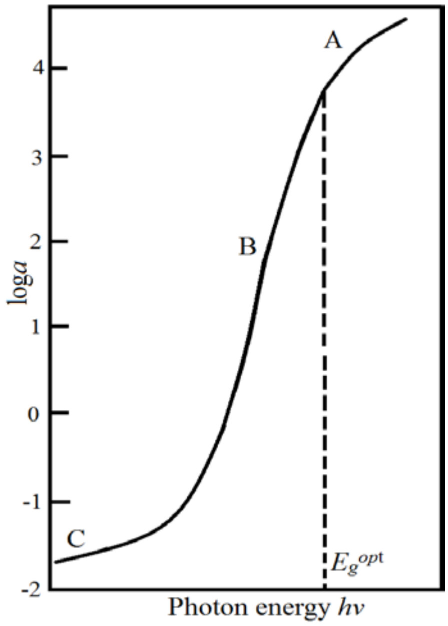

Figure 2.5. Schematic diagram of the absorption curve of amorphous materials.

The optical bandgap can be depicted as a barrier beyond which an exciton will gain enough energy jumping from the valence band to the conduction band by absorbing a photon. Exciton is an electron and a hole combined together to form a neutral pair by Coulomb interaction. It is believed that excitons contribute to the occurrence of photoluminescence which is of great interest to the application of optoelectronic devices in amorphous solids [90,91]. The optical bandgap is normally at a lower energy than the electrical bandgap, since the former refers to the threshold for photons to be absorbed, while the latter is the threshold for separating the electron and hole. For chalcogenide glasses, there is little interaction between electrons and holes, therefore, the optical and electronic bandgaps are deemed essentially identical. The optical bandgap of chalcogenide glasses varies from 0.7 eV to 3 eV [92]. According to Tauc law, the optical bandgap can be obtained by plotting $(\alpha hv)^{1/n}$ as a function hv. The exponent n indicates the type of electronic transition responsible for the absorption, n = 1/2, 2, 3/2 and 3 corresponds to the direct allowed transition; indirect allowed transition; forbidden transition; and indirect forbidden transitions, respectively. It should be noted that because of the existence of the Urbach tail, measurement of the optical bandgap from a Tauc plot can only be done reliably by using a thin (a few microns thick) sample.

The value of the optical bandgap can be theoretically calculated from Shimakawa’s empirical relation [93]:

$$E_g^{opt}(AB)(Y) = YE_g^{opt}(A) + (1-Y)E_g^{opt}(B) \tag{2.13}$$

where Y is the volume fraction of element A, and $E_g^{opt}(A)$ and $E_g^{opt}(B)$ are the optical gaps for elements A and B, respectively. The volume fraction Y is converted from atomic composition by using atomic weights and the densities.

In addition to their linear optical properties, chalcogenide glasses are also known to exhibit large nonlinear optical effects. Optical nonlinearities characterize the nonlinear response of an optical material to an applied optical field [94]. In this case, the induced polarization (*P*) will not depend linearly upon the electric field strength (*E*), but can be described by the relationship:

$$P = \chi^{(1)}E + \chi^{(2)}E^2 + \chi^{(3)}E^3 + ... \tag{2.14}$$

where $\chi^{(n)}$ denotes the *n*th-order optical susceptibility of the material. The first-order or linear optical susceptibility $\chi^{(1)}$ is related to the linear optical properties of the material, namely, linear refractive index (n_0) and linear absorption (α_0). The second-order nonlinear optical susceptibility $\chi^{(2)}$ is a third-rank tensor and can produce second-order nonlinear optical interactions, such as second-harmonic generation (SHG), sum- and difference-frequency generation (SFG and DFG). $\chi^{(2)}$ is only present in materials that lack inversion symmetry. As glasses are centrosymmetric materials, the lowest order nonlinear response would arise from the third-order nonlinear optical susceptibility $\chi^{(3)}$. $\chi^{(3)}$ is comprised of both real and imaginary component ($\chi^{(3)} = \chi_R^{(3)} + i\chi_{\mathrm{Im}}^{(3)}$). The real part of the third-order optical response leads to the changes in the refractive index, which can be represented as:

$$n = n_0 + n_2 I \tag{2.15}$$

where n_0 is the linear refractive index, n_2 is the coefficient of the intensity-dependent refractive index (Kerr nonlinear coefficient) and *I* is the intensity of incident light. A simple and empirical relation for predicting nonlinearity of a material implies that glasses with a higher linear refractive index (n_0) will also have a correspondingly high value of nonlinear refractive index (n_2) [94]. Some of the physical processes, such as electronic polarization, molecular orientation and thermal effects are responsible for the nonlinear refraction. Their effects can be distinguished by the typical time scale for the nonlinear response as listed in Table 2.1.

Table 2.1. Typical time scale of the nonlinear response for several physical processes [94].

Mechanism	Response time (sec)
Electronic polarization	10^{-15}
Molecular orientation	10^{-12}
Electrostriction	10^{-9}
Saturated atomic absorption	10^{-8}
Thermal effects	10^{-3}

Nonlinear absorption, related to the imaginary part of $\chi^{(3)}$, describes the change in transmittance of a material as a function of light intensity. While there are several mechanisms that give rise to nonlinear absorption including higher order multi-photon absorption and free carrier absorption, so far reports show that the main mechanism of nonlinear optical loss in chalcogenide glasses can be attributed to two photon absorption (TPA) if the photon energy is greater than half the bandgap of the glass [95-98]. Two-photon absorption is proportional to the intensity of the incident light. Similar to the refractive index, the case of two photon absorption can be written as:

$$\alpha = \alpha_0 + \alpha_2 I \tag{2.16}$$

where α_0 and α_2 stand for the linear absorption coefficient and two photon absorption coefficient respectively. TPA is a nonlinear process (Figure 2.6) where two photons are absorbed simultaneously to excite a transition between the valence and conduction band of the material. It imposes a serious limitation on the potential usefulness of third-order nonlinear chalcogenide glasses, therefore, the relative performance of such material can be assessed by a figure of merit (FOM) [12]:

$$\text{FOM} = n_2 / \beta\lambda \tag{2.17}$$

where β is TPA coefficient and λ is the optical wavelength. FOM characterizes the nonlinear phase shift obtainable in the materials over a distance limited by two-photon absorption. Generally speaking, figure of merit should be maximized and FOM of >10 is required for efficient all-optical devices.

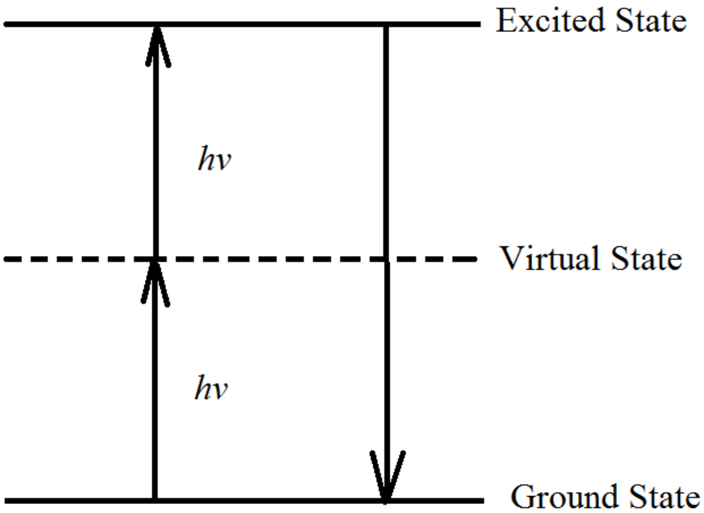

Figure 2.6. Schematic of two photon absorption.

2.3.4 Electrical properties

Chalcogenide glasses typically have electrical bandgaps (E_g^e) in the range of 1 - 3 eV, and accordingly they are regarded as semiconductors (Figure 2.7). As a consequence, the temperature dependence of the d.c. conductivity (σ_{dc}) can be written as:

$$\sigma_{dc} = \sigma_0 \exp(-E_a/kT) \tag{2.18}$$

where σ_0 is the pre-exponential constant with values between 10^2 - 10^4 Ω^{-1} cm^{-1} and E_a is the activation energy. At room temperature, E_a is approximately half of the optical band gap energy and the intrinsic d.c. conductivity in most chalcogenide glasses is low. Compositions containing tellurium normally have the smallest E_g^e and the highest conductivity, whereas those containing sulfur tend to show the opposite behavior.

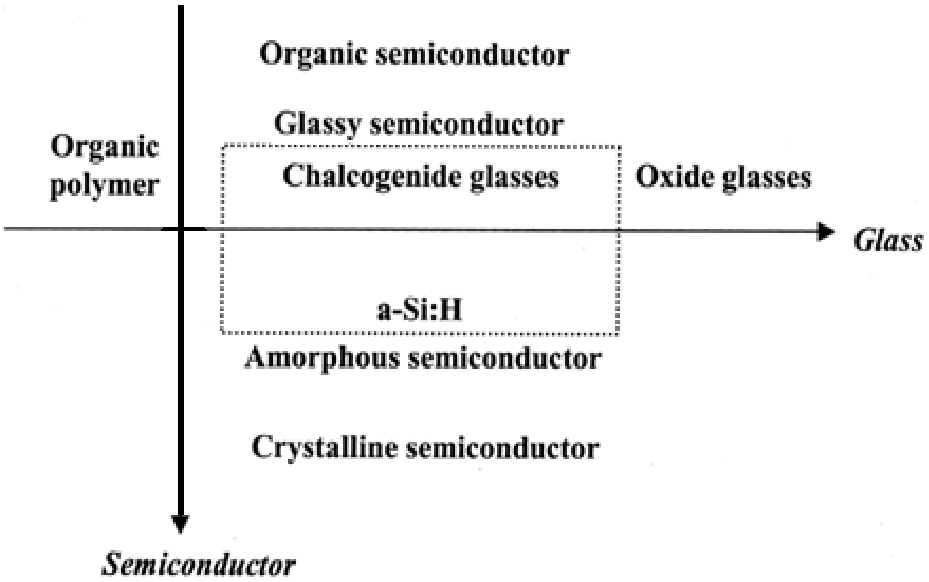

Figure 2.7. Characterization of chalcogenide glasses as glasses and semiconductors in comparison with other materials [1]. As shown on the horizontal axis, the atom bonding structure becomes more rigid in the order of organic polymers, chalcogenide and organic glasses. Semiconductor properties, *e.g.* carrier mobility, become better in the order of organic, glassy, amorphous and crystalline semiconductors.

Unlike crystalline semiconductors, the inherent structural disorder in amorphous materials leads to the existence of localized states. These localized states do not occupy all the energy continuum in the band, but form a tail above the valence band and below the conduction band [99]. Electrons in these localized states are trapped and this results in low carrier mobility. Several models have been proposed for the band structure of amorphous semiconductors on the basis of this concept (Figure 2.8).

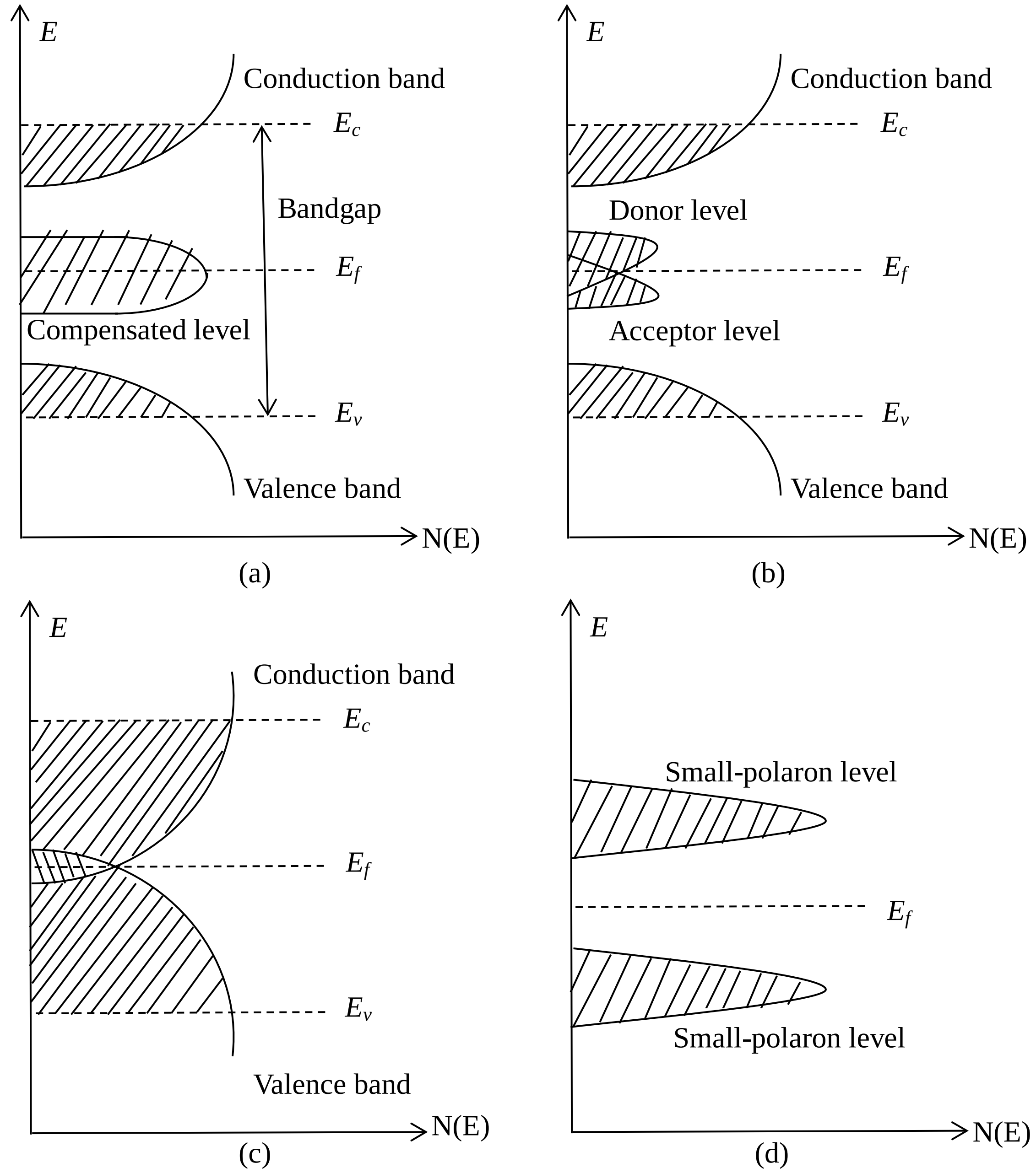

Figure 2.8. Schematic density of states N(E) for amorphous semiconductors. (a) The Davis-Mott model; (b) The modified Davis-Mott model; (c) The Cohen-Fritzsche-Ovshinsky (CFO) model; (d) The small polaron model. E_c and E_v represent the energies which separate the ranges where the states are localized and extended. E_f represents Fermi energy.

According to the Davis-Mott model [99], tails of localized states are relatively narrow and extend to a depth of several tenths of an electron volt within the bandgap. There is a band of compensated levels near the center of the bandgap, originating from defects such as dangling bonds, vacancies, etc. In a modified Davis-Mott model [100], the center band is split into overlapped donor and acceptor levels. The Fermi level is still pinned close to the middle of the bandgap. The Cohen-Fritzsche-Ovshinsky (CFO) model [101] assumes the localized band tails overlap in the middle of bandgap. This results in an appreciable density of states at the Fermi level and cause the Fermi level to be pinned near midgap. In contrast to above mentioned models, the small-polaron model suggests that the charge carriers in some amorphous semiconductors might form small polarons [102]. These carriers reside within two narrowed bands of small-polaron levels. The position of the Fermi level would then be shifted away from the middle of the bandgap. Kastner emphasizes the importance of unshared electron pairs in chalcogenide semiconductors [103]. These unshared or lone-pair (LP) electrons form a band that symmetrically splits the bonding (σ) and antibonding (σ^*) bands with respect to this reference energy. Both the σ and LP bands are occupied and the role of conduction band is played by the LP band instead of the bonding band.

The electrical switching behavior of chalcogenide glasses was firstly discovered in 1968 [104]. These semiconducting glasses exhibit a transition from high resistivity (OFF state) to low resistivity (ON state) at an applied voltage (threshold voltage V_{TH}). Primarily, there are two types of switching effect. In threshold switching, the ON state will rapidly switch back to the OFF state when the voltage is reduced below V_{TH} or turned off. In memory switching, the ON state remains even when the voltage returns to zero. The return to the initial OFF state can only be triggered by a current pulse. Broadly speaking, materials with compositions near the center of glass-forming region are more likely to exhibit threshold switching, while memory switching is usually observed in materials near the boundary of that region where crystallization is easier.

2.4 Applications of chalcogenide glasses

2.4.1 Optical applications

Chalcogenide glasses have been used in optical systems for the mid-infrared (MIR) for over 50 years and a wide range of lenses and bulk optical components are now commercially available. After being exposed to the optical or other electromagnetic irradiation, they may undergo significant changes in structure and physical properties. These photo-induced effects are either reversible or irreversible, which provide a great opportunity of developing devices for many practical applications [105]. For example, in xerography, thin films of amorphous selenium or arsenic triselenide works as a photoreceptor based on their photoconductivity [15]. The photodissolution effect in chalcogenides is desirable for high-resolution photoresists and optical storage [37].

More recently, interest has grown in the use of chalcogenides to create infrared optical fibers and waveguides. The applications of chalcogenide glass optical fibers can be essentially divided into two categories: “active” and “passive”. For “active” applications, the light propagating through the fiber is modified by processes other than those due to loss, for example, using the fiber nonlinearity or by mechanisms that produce optical gain. In “passive” applications, the fiber acts only as a conduit for light. In the latter case a potential application, due to the wide transmission window in the mid-infrared region, is to chemical and biochemical remote sensing, including detection of chemicals, pollution monitoring and identification of biomolecules [106]. Another important passive application involves the delivery of laser power for surgical purposes, which provides more precise method for tissue cutting or ablation. Some applications based on chalcogenide glass fibers are listed in Table 2.2 [23,38].

“Active” applications have been the major focus of our team, with the primary aim being to apply chalcogenide waveguides or fibers to optical communications technology taking particular advantage of the favorable nonlinear optical properties of these materials. The background for this research is the large bandwidths and low operating powers that may be used for future advances in optical communications technology. Currently electronics dominates optical communications networks and is used for buffering, error correction, regeneration and routing of data, *etc*, while optics provides only the backbone for data transport. The dominance of electronics introduces two limitations: firstly the bandwidth of the electronics is relatively small and this imposes an upper limit on the data rate that can be employed. Secondly the network contains many points where conversion between the optical and electrical domains (OE conversion) is required and this can result in wasted power. To a degree both these problems can be reduced by eliminating some of the electronics and replacing it with all-optical devices.

Table 2.2. Active and passive applications of chalcogenide glass optical fibers.

	Applications	Potential areas
Rare-earth doped fibers (A)	Fiber laser and amplifiers Infrared scene simulation Chemical sensing Grating (1.5 μm)	Telecommunications, Medical science, Spectroscopy and Military
Nonlinear effects (A)	Optical switching Raman amplification Second harmonic generation Frequency mixing	
Laser power delivery (P)	Atmospheric region (2 - 5 μm) 2.94 μm (Er:YAG) 5.4 μm (CO) 10.6 μm (CO_2) Medical free electron laser (2 -10 μm)	Military Industry, and Medical science
Chemical/biological sensing (P)	Aqueous, non-aqueous, and toxic chemicals Polymers, paints, and pharmaceuticals Condition based maintenance Cone penetrometer systems Active polymer coatings Medical diagnostics	Environmental pollution monitoring, Military and civil vehicles, and Pharmaceutical industry
Temperature monitoring (P)	Grinding ceramics	Biomedical
Thermal and Hyper-spectral imaging (P)	Coherent fiber bundles	Military and biomedical
Microscopy (P)	Imaging and Spectroscopy	Spectroscopy
Fiber multiplexing (P)	Fiber couplers	Telecommunications and Optical systems

The early research into all-optical devices focused on creating optical switches that utilized the fast third order nonlinear optical response of the material used to fabricate optical fibers or waveguides. In this context, chalcogenide glasses stand out because they combine the highest third order nonlinearity of any of the glasses with values switching in the 1990s using a nonlinear optical loop mirror made of an As_2S_3 based comparable with silicon in the telecommunications band, together with high refractive index and low nonlinear absorption [24]. Asobe *et al*. first demonstrated all-optical fiber [107 , 108]. Since then all-optical demultiplexing of high-speed time-division multiplexed (OTDM) data stream into lower-speed (10 Gb/s) signal at a receiver was demonstrated at 160 Gb/s and 640 Gb/s signal using As_2S_3 planar waveguides [109,110]. In addition, error-free demultiplexing of a 1.28 Tb/s signal down to 10 Gb/s by four-wave mixing (FWM) with negligible system penalty ($<$ 0.5 dB) was achieved in a dispersion-engineered As_2S_3 planar waveguide [111], proving the feasibility of compact chalcogenide waveguide devices for Tb/s applications.

All-optical signal regeneration is also possible [112,113] as well as all-optical wavelength conversion both of which can eliminate some of the need for OE conversion. Techniques such as four wave mixing or cross phase modulation (XPM) have been applied to perform all-optical wavelength conversion in chalcogenide devices [114,115]. Recently, non-phase-matched wavelength conversion via XPM at high bit rates (10 Gb/s) has been demonstrated in a 5 cm As_2S_3 chalcogenide rib waveguide over a wavelength range of 25 nm near 1550 nm [116].

Chalcogenides glasses can also be good hosts for rare earth doping because of their low photon energies [117] suggesting that they could be used to create on-chip optical amplifiers allowing the development of low loss circuits for all-optical signal processing. Chalcogenide films can be deposited on arbitrary substrates by physical vapour deposition and readily patterned using CMOS compatible processes [118] and hence complex circuits containing different amplifying and nonlinear elements appear feasible. Fiber and waveguide amplifiers have been demonstrated in rare earth doped chalcogenide glasses [118- 123]. It was reported that an internal gain of 6.7 dB can be obtained in a 2.4 cm long Er^{3+}-doped gallium lanthanum sulfide (GLS) chalcogenide waveguide device at 1550 nm.

Stimulated Brillouin scattering (SBS) is a nonlinear process that involves coherent light scattering off acoustic waves [94] and has been extensively investigated in fibers for applications including Brillouin lasers [124,125], sensors [126,127] and Brillouin amplifiers [128,129]. Chalcogenide glass waveguides have been recently shown to be very effective structures for on-chip SBS devices [130,131]. For example, an on-chip reconfigurable narrowband microwave photonic filter with high Q has been demonstrated in chalcogenide (As_2S_3) rib waveguide [132]; as well as a Brillouin dynamic grating (BDG) [133] and a narrow linewidth Brillouin laser [134]. These demonstrations suggest there are new opportunities for integration of chip-scale SBS-based chalcogenide devices to achieve all-optical signal processing relevant not only to telecommunications but also more generally to radio frequency signal processing.

Chalcogenide glasses are also prominent materials for applications in nonlinear optics. Supercontinuum (SC) generation in the mid-infrared has recently received particular attention due to its applications ranging from spectroscopy to metrology [21,135]. High nonlinearities make chalcogenide glasses good nonlinear media to generate broad SC spectrum. The successful SC generation has been demonstrated in the As_2Se_3 fiber taper, As_2S_3 planar waveguide and other chalcogenide devices [136,137].

2.4.2 Electronic applications

Electrical switching phenomena in chalcogenide glasses have been widely used to produce electronic devices. The most important applications are two types of switches: threshold switches and memory (bistable) switches [15]. The threshold switch is an example of a negative resistance two-terminal device, which is believed to be electronic in essence. It has been noticed that almost all chalcogenides containing arsenic show threshold switching (TS), and multicomponent chalcogenide glasses, such as the quaternary system Si-Ge-As-Te, are normally suitable for manufacturing threshold switching devices due to high degree of stability because of their cross-linked structure [138,139]. The typical sandwich structures of TS devices start with the bottom metal electrode onto which a thin layer of chalcogenide film is deposited and end with the top metal electrode. Early devices were used as electronic relays, oscillators and multivibrators but they can equally be applied in logic circuits [140]. With the advent of integrated circuits, threshold devices were employed in memory and display applications. For example, the function of the threshold switch in a display panel is to control the excitation supplied to an a.c. electroluminescent light emitting element. In the modern age, the threshold switch has been utilized in semiconductor memories as a selection device for controlling the flow or direction current. Recently, a new three terminal device based on the threshold switch has also been reported [140]. Memory switching in chalcogenide glasses is generally believed to be dominated by a thermal process, which involves phase changes from amorphous to crystalline state to store information. In the early 1970s, an electrically alterable nonvolatile memory with 256-bit capacity was produced based on chalcogenide glasses [141]. Starting from the 1990s, progress has been made towards developing new, thermally optimized phase change memory devices with increased crystallization speed and reduced programming power [142-144]. It is expected that new phase change memories could replace flash memories in the market to meet the needs for low-cost and quicker storage although it has proven difficult to achieve the desired combination of fast switching and high stability as cell sizes are reduced.

In addition, chalcogenide glasses, such as CdTe and $Cu(In,Ga)Se_2$ (CIGS), are used as absorber layers in thin film solar cell [145]. The highest power conversion efficiency of 21% has been attained to date, which beats the record of polycrystalline silicon solar cell devices in the current photovoltaic industry [146]. Some chalcogenide systems have already proven their potential as fast ion conductors, and all-solid batteries have been developed using these materials as solid-state electrolyte [147].

2.5 Summary

Several milestones in the development of chalcogenide glasses and their structural, thermal, mechanical, optical and electrical properties have been reviewed. The applications of these materials in specific field have also been presented. However, these only represent a fraction of the capability of chalcogenide glasses. Therefore, for the purpose of realizing full potential of these unique glasses, mastering the knowledge of composition-structure-property relationships will become particularly important.

Chapter 3

Structural Study of Ge-As-Se Glasses

3.1 Introduction

Information on the short-range order in chalcogenide glasses is absolutely invaluable in establishing useful correlations between structural and macroscopic properties. This is particularly important for fabricating planar chalcogenide glass devices in order to realize their full potential for photonic applications. Two major approaches, computer simulations and experimental observations, have been employed to investigate the structure of glassy materials. Computer simulations, such as Molecular Dynamics (MD) and Reverse Monte Carlo (RMC) algorithms have been successfully and quite widely used to quantitatively explore the geometric characteristics of the chalcogenide systems [148,149]. These methods can provide detailed structural images, but the calculation processes are tedious and complicated and the credibility of the results relies heavily upon the chosen parameters and computational capacity. On the other hand, the rapid developments of experimental techniques, such as Nuclear Quadrupole Resonance (NQR), High-resolution X-ray Photoelectron Spectroscopy (XPS) and Mössbauer Spectroscopy, have improved markedly the measurement of the steric features of chalcogenide glasses. Golovchak *et al*. investigated binary Ge_xSe_{100-x} $(0 \leq x \leq 30)$ and As_xSe_{100-x} $(x \leq 40)$ chalcogenide glass family using High-resolution XPS. The results have shown that, edge-sharing $GeSe_{4/2}$ tetrahedral units exist in Se-rich Ge_xSe_{100-x} (x >

10) glasses and there is no evidence for intermediate phase in all compositions; As-As homopolar bond exists in the stoichiometric composition $As_{40}Se_{60}$ and the formation of double As=Se bonds is not observed in the structure of Se-rich As_xSe_{100-x} glasses [150,151]. Combining NQR and Electron Paramagnetic Resonance (EPR) spectroscopy, Bolebrukh *et al.* have found that structural transition from a two-dimensional to three-dimensional structure occurs at $<r>$ = 2.45 for the Ge-As-Se system [152]. The Mössbauer studies support the idea of physical threshold behavior at $<r>$ =2.40 as predicted by the rigidity percolation model [153]. Although various spectroscopic methods have been used to probe the structure of chalcogenide glasses, the explanations of spectra are sometimes controversy due to limited knowledge.

Over the last few decades, Raman spectroscopy has become a powerful experimental tool for studying the local structure of glassy materials [154-156]. Raman spectroscopy involves scattering of an incident light beam by an optical-mode lattice vibration. Since this inelastic scattering process involves the interaction of a photon with vibrational, rotational and other low frequency states in condensed matter, the analysis of Raman spectra can provide real structural information on the sample by carefully choosing the excitation light. In general, the intensities of the various peaks are associated with vibrational modes of particular structural units, and the changes in the shape and position of these peaks reflect the evolution of the structure. It has been found that, for Ge_xSe_{100-x} glasses, the 250 cm^{-1} and 230 cm^{-1} peak are characteristic of ring-shaped selenium and chain-like selenium respectively, while the peaks located at 215 cm^{-1} and 195 cm^{-1} are assigned to edge-sharing and corner-sharing $GeSe_{4/2}$ tetrahedral breathing modes respectively [157,158]. As for As_xSe_{100-x} glasses, one peak situated around 230 cm^{-1} is associated with the vibrational mode of $AsSe_{3/2}$ pyramidal units. The appearance of several distinct peaks centered around 240 cm^{-1} and 250 cm^{-1} are contributions of As_4Se_3 and As_4Se_4 cage-like clusters [156,159].

Another important experimental technique that has been successfully used to probe structural information of amorphous materials is Extended X-ray Absorption Fine Structure (EXAFS) spectroscopy [160-162]. The EXAFS spectrum appears as an oscillating part of the X-ray Absorption Spectrum (XAS) extending from 50 eV up to 1000 eV beyond the absorption edge of a particular atom. It involves a process (Figure 3.1) in which an incident X-ray beam with sufficient energy when incident on a material ejects a core electron from the absorbing atom. This ejected photoelectron exhibits wave-particle duality and can be scattered by neighboring atoms which are also called backscattering atoms. The scattered photoelectron can return to the absorbing atom, which gives rise to an interference effect between the outgoing photoelectron wave and the backscattered wave. The regions of constructive and destructive interference are respectively seen as local maxima and minima leading to the characteristic oscillations in the EXAFS spectrum [163]. The variation of the EXAFS spectrum is specific to each element and sensitive mostly to short-range order, hence EXAFS spectroscopy can provide information on the local environment of a specific atom in terms of its coordination number, the type of neighboring atoms as well as the interatomic distances. Early EXAFS studies on chalcogenide glasses in the Ge-Se and As-Se systems have confirmed the Pauling covalent radii and the 8-*N* rule for the constituent atoms [164].

The average nearest-neighbor distances obtained for binary Ge_xSe_{100-x} and As_xSe_{100-x} glasses are as follows: the Ge-Se bond is around 2.365 Å and the As-Se bond is around 2.40 Å [160,162]. Homopolar bonds were also identified in the two aforementioned systems depending on the composition. The bond length was about 2.35 Å for Se-Se bond, slightly shorter than 2.45 Å for the Ge-Ge bond, and approximately 2.40 Å for the As-As bond [160,165]. Sen *et al.* have reported the EXAFS spectra of $Ge_xAs_ySe_{1-x-y}$ glasses with x:y = 1:1 and 1:2 and found that chemical order is largely preserved in stoichiometric and Se-rich $Ge_xAs_ySe_{1-x-y}$ glasses [41]. On the contrary, chemical order is strongly violated in the case of Se-poor $Ge_xAs_ySe_{1-x-y}$ glasses where the chalcogen deficiency is compensated by the formation of As-As homopolar bonds at low and intermediate levels of Se deficiency. The Ge atoms take part in homopolar bonding only in strongly Se-poor glasses.

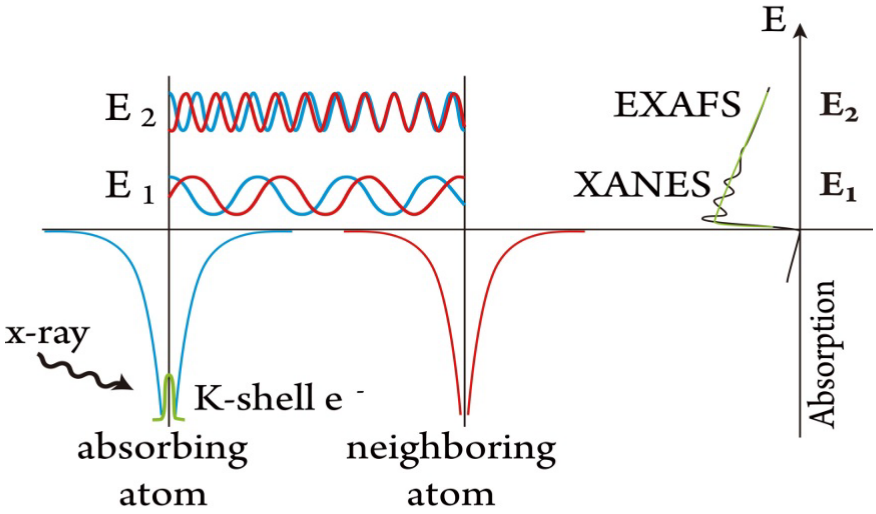

Figure 3.1. Schematic diagram of the x-ray absorption process [166].

It has become unambiguous in recent years that glass compositions with stable physical properties are essential for integrated photonic devices. However, the chemical bond within chalcogenide glasses can rearrange when the materials are exposed to light or heat, which can cause changes in the structure, density, and optical and electrical properties [167]. This effect, in addition to physical aging phenomenon [168], can undermine the long-term stability and reliability of fabricated devices under certain thermal, mechanical or optical conditions. Hence, a fundamental understanding of their structures will be helpful in choosing the best compositions with reliable and predicable properties over the glass-forming ranges for applications in photonics. In this chapter, the local structure of some ternary $Ge_xAs_ySe_{100-x-y}$ chalcogenide glasses is investigated by Raman and EXAFS spectroscopy. The validity of several structural models is further examined. An attempt is also made to estimate the possible bond arrangement and compositional effects in this system of glasses.

3.2 Sample preparation and experiments

Bulk $Ge_xAs_ySe_{100-x-y}$ chalcogenide glasses were prepared by the conventional melt-quenching technique. Since chalcogenide glasses are extremely sensitive to impurities, such as oxygen or hydrogen, all synthesis processes were carried out in an oxygen-free and water-free environment. The raw starting materials used in this study were Germanium, Arsenic and Selenium metals with 99.999% purity. These elements with a total mass of 15 g were weighed inside a dry nitrogen glove box and loaded into a pre-cleaned quartz ampoule. The loaded ampoule was evacuated under vacuum (10^{-6} Torr) at 110 °C for 4 h to remove surface moisture from the raw materials. The ampoule was then sealed under vacuum using an oxygen-hydrogen torch. The procedure of preparing sealed quartz ampoules under vacuum is schematically depicted in Figure 3.2.

The sealed ampoule was then introduced into a rocking furnace and gradually heated to a temperature between 900 and 950 °C, depending on the glass composition. In order to avoid compositional heterogeneity and facilitate reactions between the different elements, the furnace was rocked slowly throughout melting. The melt was thereby homogenized for a period of not less than 30 hours, after which the ampoule was removed from the rocking furnace at a predetermined temperature and quenched in water. To reduce the internal stress resulting from the quenching step, the resulting glass boule was subsequently annealed at a temperature 30 °C below its estimated glass transition temperature, T_g, then slowly cooled to room temperature. Following this, the bulk glass was removed from the broken ampoule, sectioned and parallel polished to about 2 mm thickness for further testing. The amorphous nature of each glass was verified by using X-ray diffraction (XRD) and no sharp peaks were observed for any composition. The optical quality was checked by a handheld digital microscope (Dino-Lite). Glass defects such as bubbles or inclusions were not found in the samples.

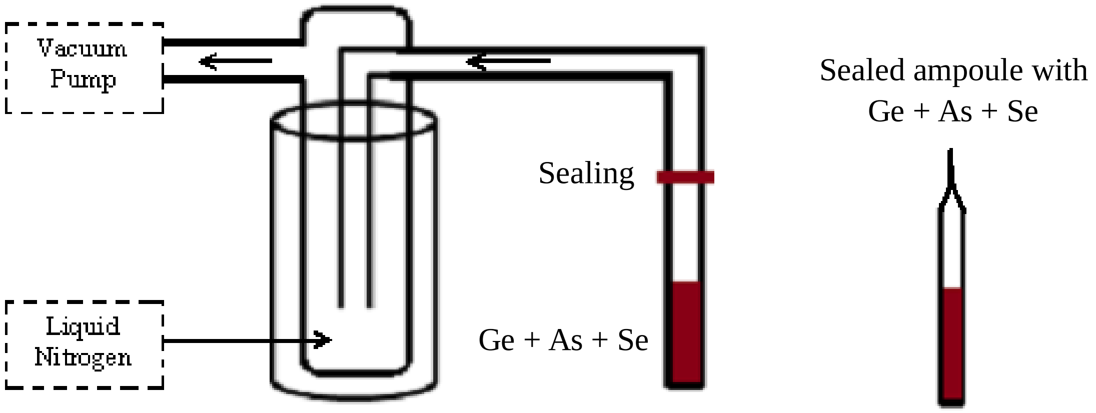

Figure 3.2. Normal setup used for preparing sealed quartz ampoules under vacuum.

Raman spectral measurements were conducted using a T64000 micro-Raman spectrometer (HORIBA Jobin Yvon). The Raman spectra were collected over the range from 150 - 500 cm^{-1} using a 830 nm laser source. In order to achieve a good signal to noise ratio and avoid photo-induced effect, the Raman spectra of samples after being irradiated by higher laser power were checked against those of fresh samples measured at lower laser intensities. Provided that there was no difference between these two spectra, the experimental conditions were considered to have been optimized and photo-induced effects were generally suppressed.

The typical experimental setup for an EXAFS measurement is shown in Figure 3.3. EXAFS spectra of the Ge, As and Se K-edge (11103, 11867 and 12658 eV, respectively) were recorded at 1W1B-XAFS beam line of the Beijing Synchrotron Radiation Facility in transmission mode. Samples of bulk glasses were ground into powders with particle sizes of about 30 μm. These powdered samples then were spread evenly on adhesive tape for the measurement. The beam line was equipped with a Si (111) monochromator. The EXAFS data were collected at room temperature using ionization chambers filled with mixtures of nitrogen and argon gases. The processing and analysis of EXAFS data were carried out by a standard technique using IFEFFIT software package [169].

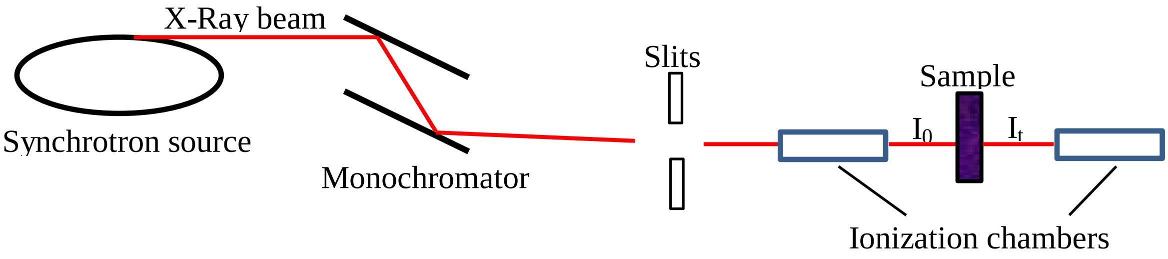

Figure 3.3 Schematic of EXAFS experiment setup.

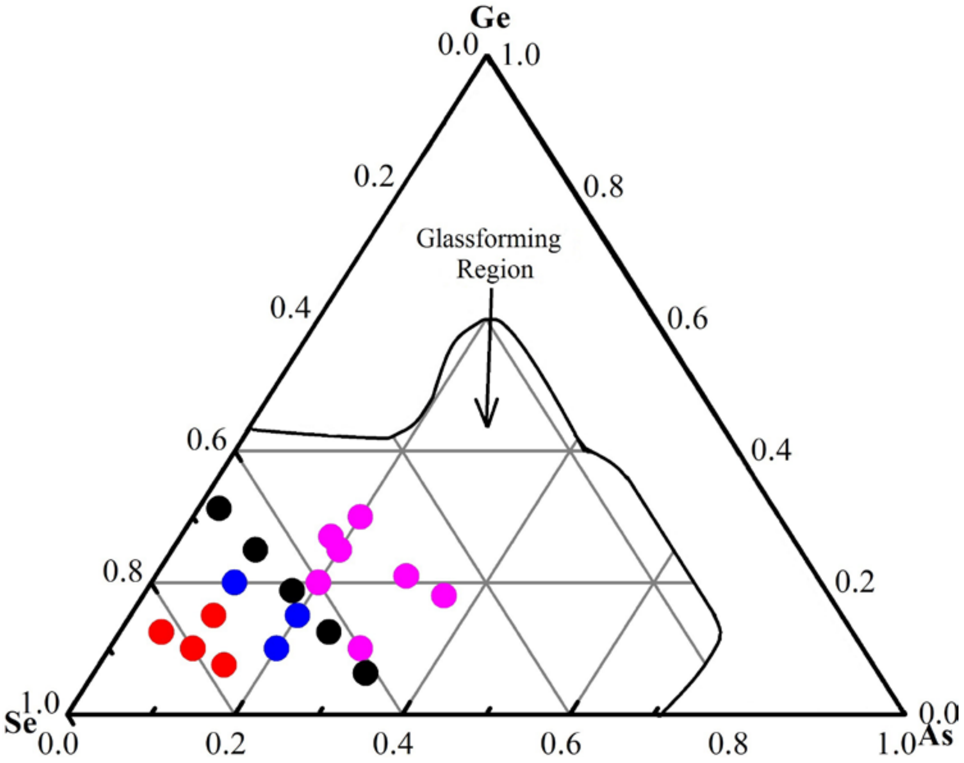

Figure 3.4. Glass formation domain of the $Ge_xAs_ySe_{100-x-y}$ ternary system showing the 19 compositions investigated by Raman spectroscopy. The red, blue and magenta dots correspond to compositions with high, intermediate and low Se content, respectively. Five stoichiometric compositions are depicted by black dots.

The structure of 19 bulk $Ge_xAs_ySe_{100-x-y}$ glasses including stoichiometric compositions (equivalent to $(GeSe_2)_x(As_2Se_3)_{100-x}$) was investigated using Raman scattering spectroscopy. The non-stoichiometric compositions can be categorized as follows: (1) 4 compositions with high Se content (Se ≥ 75 at%, depicted by red dots in Figure 3.4) (2) 3 compositions with intermediate Se content (70 ≤ Se ≤ 65 at%, depicted by blue dots in Figure 3.4) (3) 7 compositions with low Se content (Se ≤ 60 at%, depicted by magenta dots in Figure 3.4). In addition, for non-stoichiometric compositions, the departure from stoichiometry can be quantified as the degree to which the glasses are Se-rich or Se-poor according to (Se-rich/-poor) % = (100 - x - y) - 2x - 1.5y = 100 - 3x - 2.5y. The chemical compositions of the glasses are listed in Table 3.1 and illustrated in Figure 3.4. The local coordination environment of five glass samples with same mean coordination number (<*r*> = 2.50) were also investigated by EXAFS.

Table 3.1. Compositions and respective mean coordination number (<*r*>), the extent of Se-rich/Se-poor for $Ge_xAs_ySe_{100-x-y}$ glasses investigated by Raman spectroscopy.

Compositions Ge-As-Se (at%)	<*r*>	Se-rich/-poor (at%)
12.5-5-82.5	2.30	+50
10-10-80	2.30	+45
7.5-15-77.5	2.30	+40
15-10-75	2.40	+30
10-20-70	2.40	+20
20-10-70	2.50	+15
15-20-65	2.50	+5
10-30-60	2.50	-5
20-20-60	2.60	-10
25-20-55	2.70	-25
27-18-55	2.72	-26
21-30-49	2.72	-38
18-36-46	2.72	-44
30-20-50	2.80	-40
7.5-35-57.5	2.50	-10
6.25-32.5-61.25	2.45	0
12.5-25-62.5	2.50	0
18.75-17.5-63.75	2.55	0
25-10-65	2.60	0
31.25-2.5-66.25	2.65	0

3.3 Results

3.3.1 Raman scattering spectra of Ge-As-Se glasses

The normalized Raman spectra for non-stoichiometric $Ge_xAs_ySe_{100-x-y}$ bulk glasses are shown in Figure 3.5. For samples with high Se content (Se ≥ 75 at%, high level of Se-rich), the whole spectra typically consist of a peak at about 197 cm^{-1} and a main band centered around 255 cm^{-1}. At intermediate Se content (70 ≤ Se ≤ 65 at%, intermediate level of Se-rich), no obvious changes in the position are observed for the first Raman band (197 cm^{-1}); while the second one (255 cm^{-1}) becomes broader accompanied by a downward shift of the center. For the third set (Se ≤ 60 at%, Se-poor), the peak located at 197 cm^{-1} shifts towards lower wavenumbers with decreasing Se concentration, another principal band decreases in intensity and a weak shoulder appears in the range of 280 - 300 cm^{-1}.

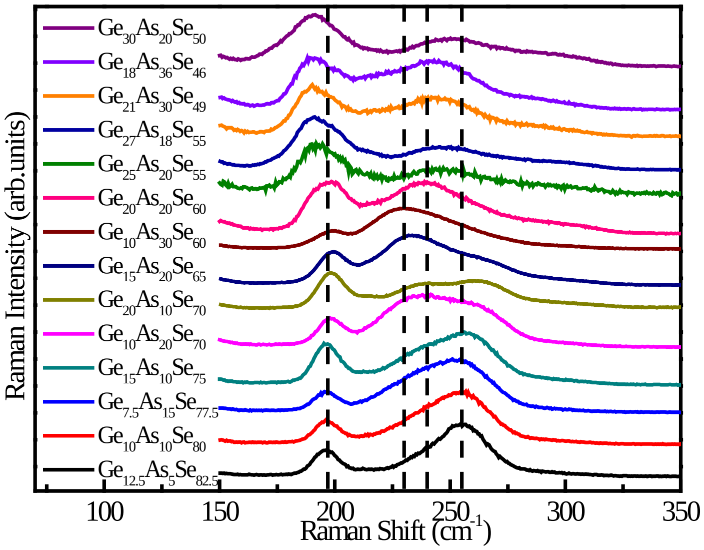

Figure 3.5. Normalized Raman spectra of non-stoichiometric bulk glasses. The vertical dashed lines (from left to right) are drawn to indicate the Raman shift at 197 cm^{-1}, 230 cm^{-1}, 240 cm^{-1} and 255 cm^{-1}.

Figure 3.6 shows Raman spectra of glasses with stoichiometric compositions. In comparison with the non-stoichiometric cases, a distinct band appears near 230 cm^{-1} in all five samples. With increasing Ge/As ratio, the relative intensity of this band becomes extremely weak and it shifts to higher wavenumbers, while the intensity of other band at 197 cm^{-1} rises steadily. This is simultaneously accompanied by the emergence of a shoulder at 213 cm^{-1}.

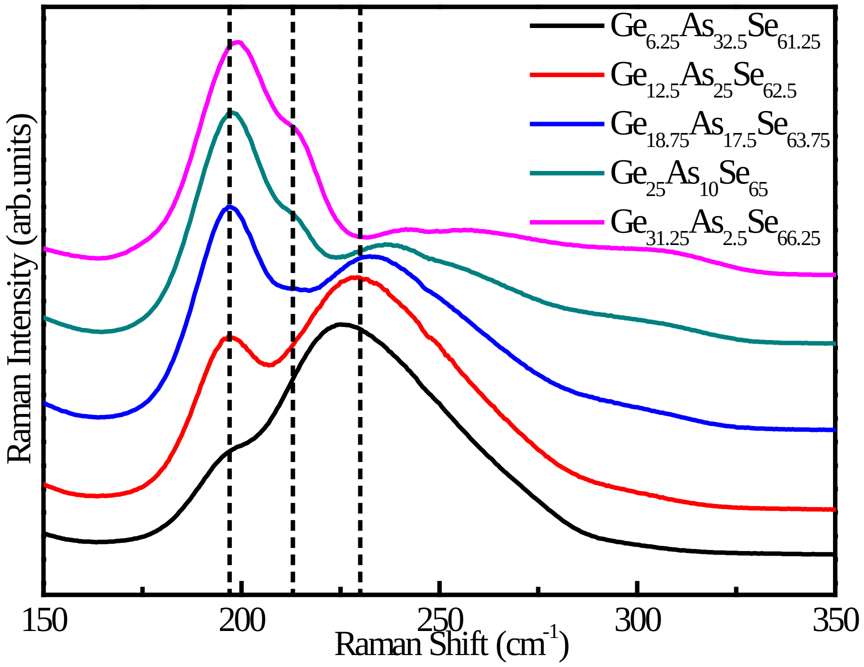

Figure 3.6. Normalized Raman spectra of glasses with stoichiometric compositions. The vertical dashed lines (from left to right) are drawn to indicate Raman shift at 197 cm^{-1}, 213 cm^{-1} and 230 cm^{-1}.

In order to obtain more detailed information on the structural evolution as a function of the composition, the Raman spectra were further decomposed into several Gaussian curves whose positions and areas indicate the vibrational frequencies of each structural unit and their relative intensity contribution to the total spectra. Table 3.2 summarizes the contributions of the main structural units to the Raman scattering spectra in Ge_xSe_{100-x} and As_xSe_{100-x} glass according to previous studies. These assignments of

Raman mode can be used to perform the peak-fitting analyses for $Ge_xAs_ySe_{100-x}$ glasses, since Ge, As and Se atoms are of similar atomic radii and weights, substituting one element in small amount for another will not cause significant changes in the vibrational frequencies but only broaden the bands in the amorphous phase. Figure 3.7 shows examples of decomposed Raman spectra for two typical Se-rich and Se-poor compositions, respectively.

Table 3.2. Assignment of Raman modes for $Ge_xAs_ySe_{100-x-y}$ glasses.

Raman Shift (cm^{-1})	Assignment	Reference
193 - 200	corner-sharing $GeSe_{4/2}$ tetrahedra symmetric stretching	[157,170]
215	edge-sharing $GeSe_{4/2}$ tetrahedra vibration	[158,170]
224 - 230	$AsSe_{3/2}$ pyramids symmetric stretching	[156,170 ,171]
235	Se_n chains vibration	[171]
250 - 260	Se_8 fragments or rings vibration	[171]
170, 270	Ge-Ge bond vibration	[170,172]
190	As-As bond vibration	[171,173]
248	As-Se bond vibration	[170,172]
285 - 300	$GeSe_{4/2}$ tetrahedra asymmetric vibration	[172]

Figure 3.8(a) shows decomposed Raman vibrational frequencies as a function of the departure from stoichiometry for the Se-rich glasses. The position of each peak is essentially in agreement with results shown in Table 3.2. The band located between 252 cm^{-1} and 258 cm^{-1} is attributed to stretching vibration of “meandering” Se chains including both Se_n polymeric chains and Se ring-like fragments. The band at 235 - 240 cm^{-1} is related to a small fraction of helical Se chains exclusively. Decreasing Se content will lead to a progressive growth in the intensity of the 235 cm^{-1} band and a simultaneous reduction in the intensity of the 255 cm^{-1} band (Figure 3.8(b)).

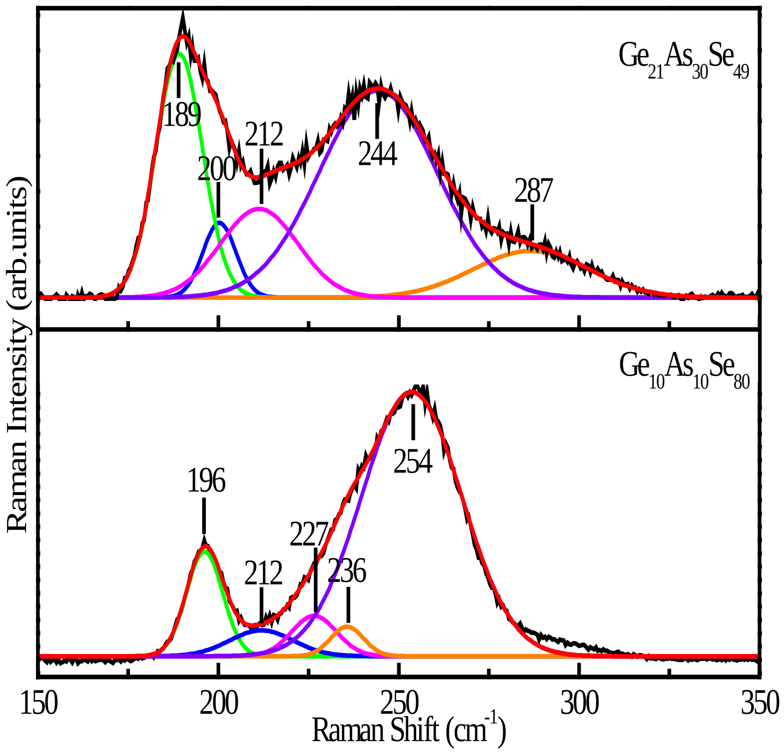

Figure 3.7. Decomposed Raman spectra for $Ge_{10}As_{10}Se_{80}$ and $Ge_{21}As_{30}Se_{49}$ glasses. Black lines represent experimental data, red lines are fitted spectra and the rest colored lines are the decomposed Gaussian curves.

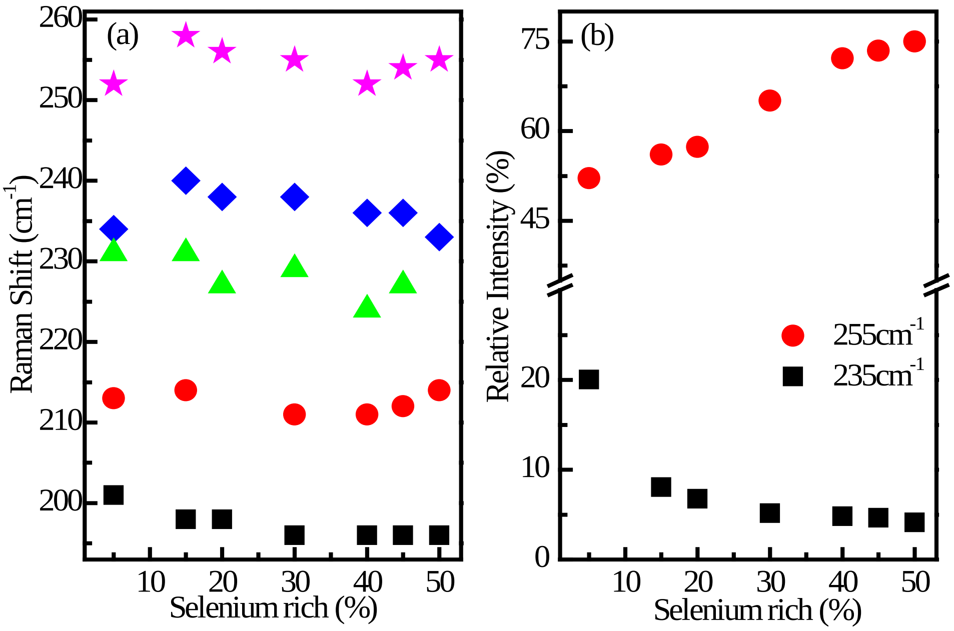

Figure 3.8. Raman vibrational modes (a) and relative intensity of two bands (b) as a function of departure from stoichiometry in atomic percent of selenium for Se-rich glasses. Band at 235 cm^{-1} and 250 cm^{-1} correspond to contributions from helical Se-chains and meandering Se-chains respectively.

The intensities of the corner-sharing and edge-sharing $GeSe_{4/2}$ both increase with increasing Ge content for Se-rich glasses (Figure 3.9). As shown in the insert of Figure 3.9, the relative change of the scattering intensity covering 195 - 215 cm^{-1}, which relate to Ge-Se bond vibrations to that at 227 cm^{-1}, is roughly proportional to the change of the Ge/As ratio, which confirms the existence of $AsSe_{3/2}$ pyramidal units.

For Se-poor glasses (the third sub-set having lower Se content), the band near 255 cm^{-1} disappears. Instead, a new Raman feature peaking near 247 cm^{-1} appears. The shoulder appears in the region 280 - 290 cm^{-1} which is attributed to the asymmetric vibration mode of $GeSe_{4/2}$ tetrahedra. The presence of a distinct Raman peak at 189 cm^{-1} indicates the formation of As-As homopolar bonds in the glassy matrix. The changes in the relative intensity of three vibration groups are roughly consistent with the variation of Ge content (Figure 3.10). With increasing Ge content, the contributions of As-Se heteropolar bonds and As-As homopolar bonds decrease and increase, respectively.

For stoichiometric compositions as shown in Figure 3.11, the changes in two main Raman bands at around 195 - 199 cm^{-1} and 226 - 242 cm^{-1} respectively verify that corner-sharing $GeSe_{4/2}$ tetrahedra and $AsSe_{3/2}$ pyramids are fundamental structural units. The positions of these peaks gradually shift towards higher wavenumber with increasing Se concentration. The weak bands situated around 300cm^{-1} can be assigned to the asymmetric vibration modes of $GeSe_{4/2}$ tetrahedra. The contribution from the band at 257 - 262 cm^{-1} is associated with the vibration of Se-Se homopolar bond. In addition, the broader shoulders, situated in the 183 - 186 cm^{-1} and 278 - 288 cm^{-1} regions, indicate the presence of structural units containing As-As and Ge-Ge homopolar bonds in the stoichiometric glasses containing higher Ge/As ratio as shown in Figure 3.12.

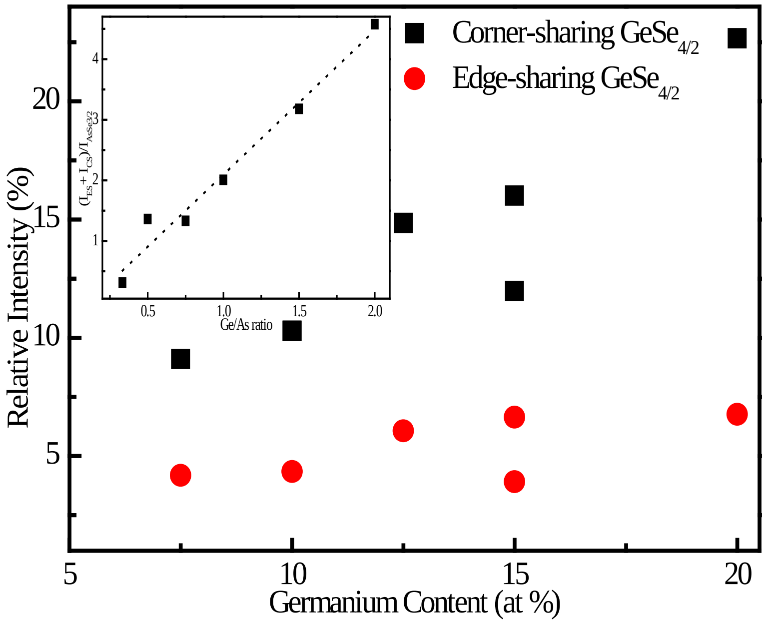

Figure 3.9. Relative intensities of corner-sharing and edge-sharing $GeSe_{4/2}$ as a function of Germanium content. The inset is the ratio of the scattering intensity at 195 - 215 cm^{-1} to that at 227 cm^{-1} as a function of Ge/As ratio. The dotted line is a linear fitting result.

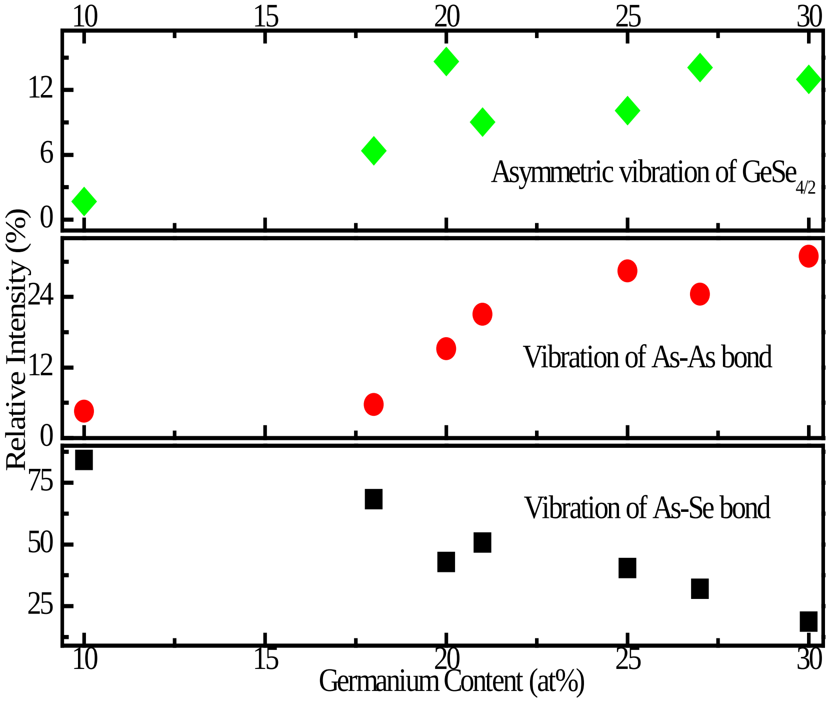

Figure 3.10. Relative intensities of three vibrational modes as a function of Germanium content for Se-poor glasses derived from the decomposed Raman spectra.

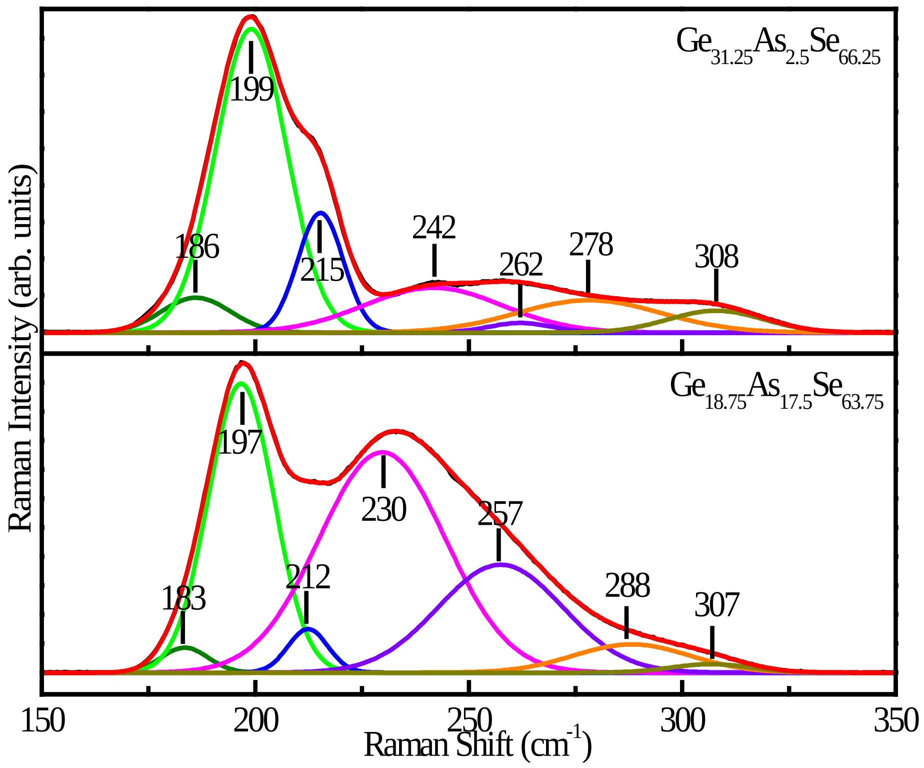

Figure 3.11. Decomposed Raman spectra for $Ge_{18.75}As_{17.5}Se_{63.75}$ and $Ge_{31.25}As_{2.5}Se_{66.25}$ glasses. Black lines represent experimental data, red lines are fitted spectra and the rest colored lines are the decomposed Gaussian curves.

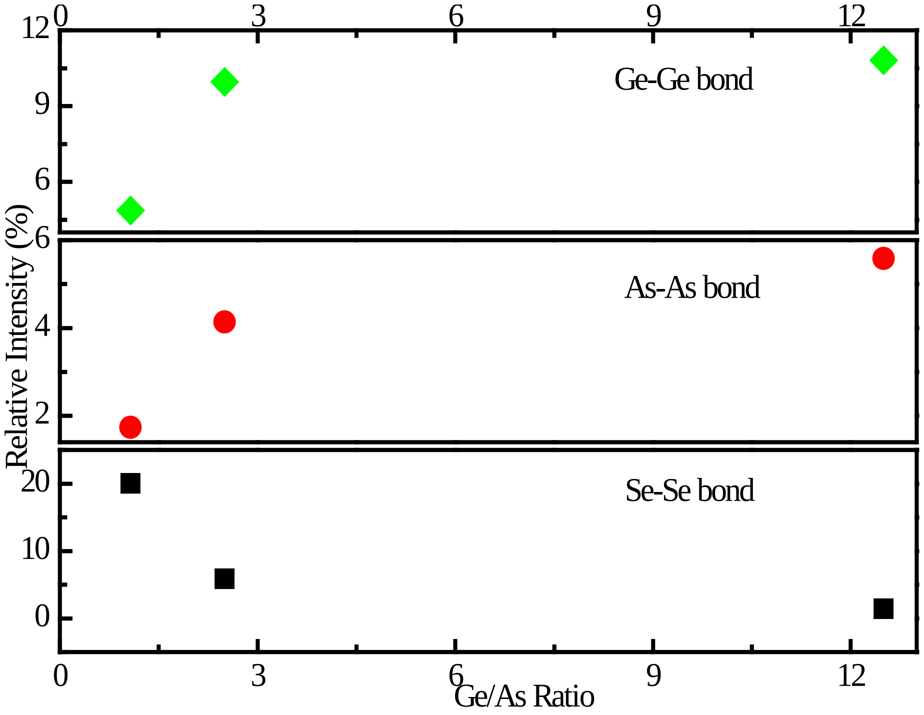

Figure 3.12 Relative intensities of structural units containing homopolar bonds as a function of Ge/As ratio for stoichiometric glasses.

3.3.2 EXAFS spectra of Ge-As-Se glasses

After removal of the background and normalization, the EXAFS data were converted from energy space, *E,* to momentum space, *k*. The EXAFS oscillations were k^3-weighted to compensate for the reduction in amplitude at higher *k* values, and to minimize the chemical effects on the signal in the lower *k* region. Subsequently, the spectra were Fourier transformed to *R*-space by applying a Hanning window function within the *k* range between 3.1 and 12 $Å^{-1}$. The main peak in the spectrum was inverse Fourier transformed through a Hanning window function with the width of 2 Å from 1 Å to 3 Å. Eventually, the structural parameters, *e.g.* the coordination number (*N*), the average interatomic distance (*R*) and the Debye-Waller factor σ^2 were extracted from fitting of the experimental data to the theoretical EXAFS formula in *k*-space.

The Fourier transform of the k^3-weighted EXAFS spectra for $Ge_xAs_ySe_{100-x-y}$ glasses with the same mean coordination number ($<r>$ = 2.50) for the Ge, As and Se *K*-edge are shown in Figure 3.13. In the Fourier transform EXAFS spectra, the position of the peaks are related to the distance between the absorbing atom and the neighboring atom while the amplitude of the peaks are related to coordination environments (*e.g.* the numbers and types of the neighboring atoms, the scattering power of these atoms). Apparently, all the compositions preserve short-range order primarily to the first shell, since Ge, As and Se *K*-edge EXAFS spectra all show a single peak within 3 Å. No significant shift is observed in the position of these peaks. With increasing Se content, there is an increase in the peak intensity at Ge and As K-edge, whereas there is a decrease in the peak

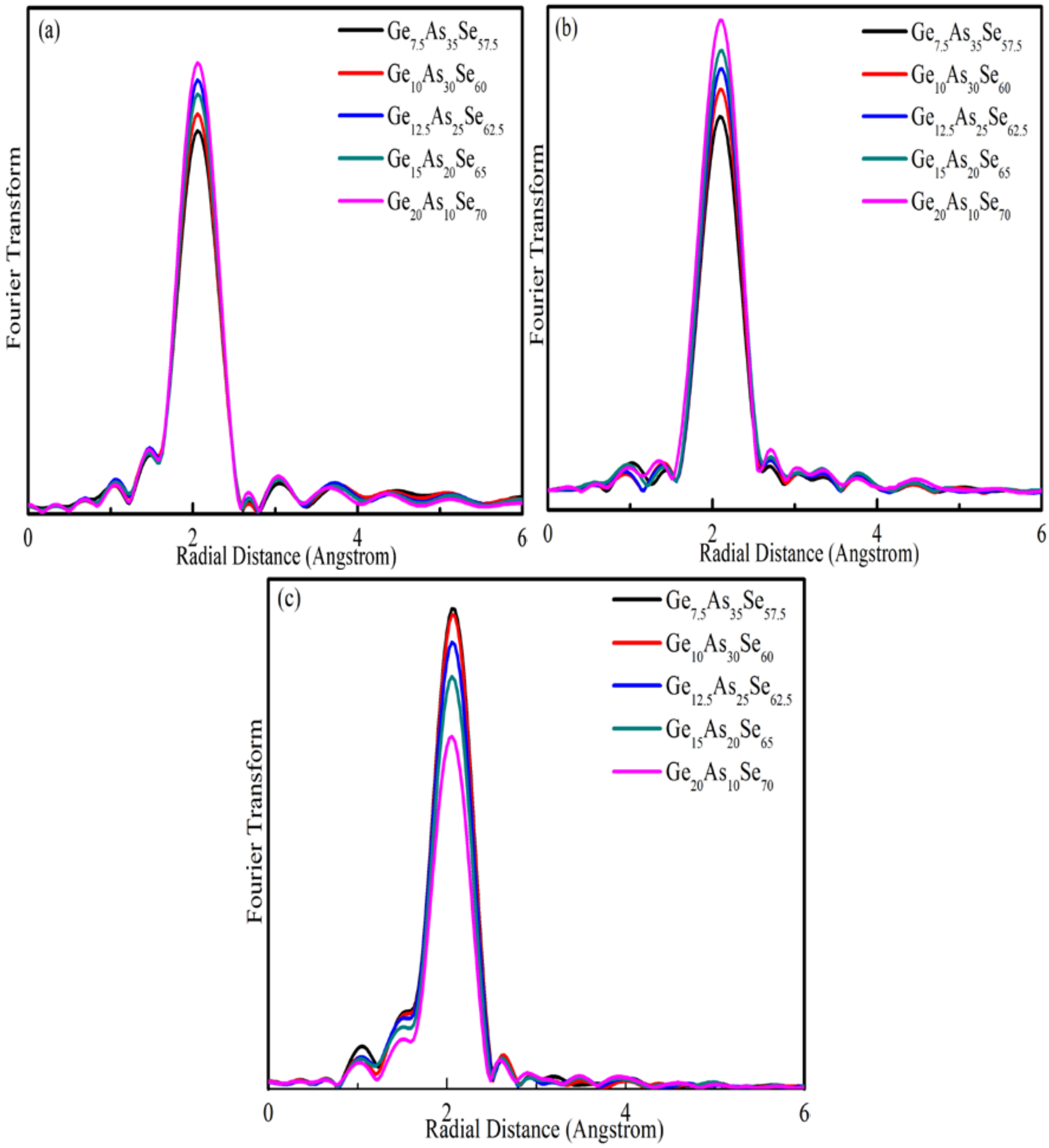

Figure 3.13. Magnitudes of the Fourier transform without phase correction of k^3-weighted EXAFS spectra at (a) Ge *K*-edge, (b) As *K*-edge and (c) Se *K*-edge.

intensity at Se K-edge. The decrease in the intensity of the Fourier transform first peak can be related to an increase of the Debye-Waller factor, which indicates an increase in the structural disorder around Se atoms. In order to obtain more precise structural information, the peaks in the Fourier transform k^3-weighted EXAFS spectra are backtransformed from *R*-space into *k*-space, and the resulting filtered EXAFS function is then analysed by non-linear least squares fitting to obtain structural parameters of interest. Figure 3.14 shows backtransformed first shell of Fourier transform k^3-weighted EXAFS spectra at Ge, As and Se K-edge and the fittings to these data which are generally in good agreement. The structural parameters for the first coordination shell of the Ge, As and Se atoms obtained from the fitting procedure are given in Table 3.3.

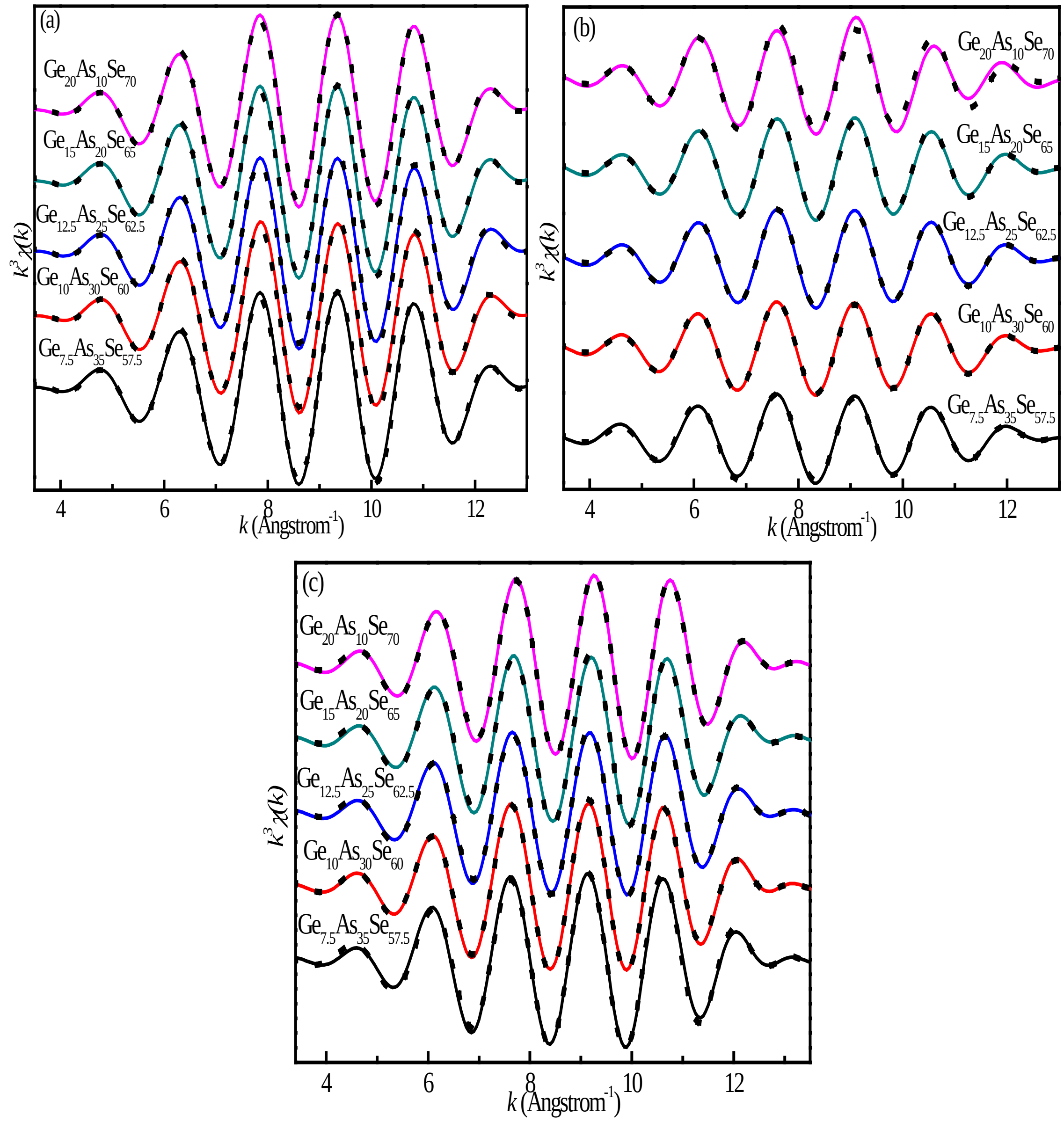

Figure 3.14. Backtransformed first shell of Fourier transform k^3-weighted EXAFS spectra at (a) Ge, (b) As and (c) Se *K*-edge and experimental fit. Solid lines represent experimental data and dot lines correspond to fitting results.

Although these glasses have same mean coordination number, their chemical compositions change from being as low as 10 at% Se-poor, to stoichiometric, and up to 15 at% Se-rich, and these can be used to investigate the proportion of different structural units and bonding trend in the glasses. According to the fitting results, the nearest coordination number of Ge atoms is fixed at 4. The overwhelming majority of Se atoms are bound to Ge atoms showing negligible Ge-As bonds in the compositional range studied. The nearest neighbor bond lengths of Ge remained approximately constant, within experimental error, no matter whether they are deduced from Ge-edge data or from the data for the neighboring Se atoms. These are consistent with previous study [41]. In the case of the As *K*-edge EXAFS spectra, two types of bonds (As-Se and As-As) were also deduced. As can be seen from Table 3.3, changes in the coordination number for As atoms indicate that the role of homopolar bonds becomes obvious with increasing As content. The larger Debye-Waller factors also imply increased local distortion. All Arsenic atoms are always 3-fold coordinated, which is in accordance with trigonal pyramidal configuration. The average nearest neighbor bond length for As atoms decreases slightly from 2.42(0) Å to 2.41(4) Å with decreasing As content, resulting from the formation of homopolar bonds in As-rich glasses. A similar behavior was detected from the local structural information of Se atoms. The nearest coordination number for Se atoms in all glasses remained approximately constant at 2. The average nearest neighbor distance for Se atoms decreases significantly from 2.40(4) Å for $Ge_{7.5}As_{35}Se_{57.5}$ to 2.38(0) Å for $Ge_{20}As_{10}Se_{70}$, due to the contribution of a certain amount of Se-Se bonds in the samples. Se-Se bonds have not been identified in the stoichiometric composition, which may partially due to the resolution limit of EXAFS method.

Table 3.3. Ge, As and Se *K*-edge EXAFS structural parameters (the coordination number *N*, the bond length *R* and Debye-Waller factor σ^2) for $Ge_xAs_ySe_{100-x-y}$ glasses.

	$Ge_{7.5}As_{35}Se_{57.5}$ (+10)			$Ge_{10}As_{30}Se_{60}$ (+5)			$Ge_{12.5}As_{25}Se_{62.5}$ (0)			$Ge_{15}As_{20}Se_{65}$ (-5)			$Ge_{20}As_{10}Se_{70}$ (-15)		
	N	*R*(Å)	σ^2(Å)	*N*	*R*(Å)	σ^2(Å)	*N*	*R*(Å)	σ^2(Å)	*N*	*R*(Å)	σ^2(Å)	*N*	*R*(Å)	σ^2(Å)
Ge-Se	3.84	2.37(7)	0.005	3.73	2.37(8)	0.005	3.91	2.37(5)	0.004	3.94	2.37(3)	0.004	3.96	2.37(2)	0.003
Ge-As	0.16	2.42(8)	0.009	0.27	2.42(9)	0.007	0.08	2.42(7)	0.006	0.06	2.42(5)	0.005	0.04	2.42(3)	0.004
As-Se	2.56	2.41(9)	0.007	2.64	2.41(5)	0.005	2.79	2.41(4)	0.005	2.95	2.41(4)	0.004	3.0	2.41(4)	0.004
As-As	0.45	2.42(6)	0.006	0.36	2.42(8)	0.006	0.21	2.42(5)	0.004	0.05	2.42(1)	0.004	-	-	-
Se-Ge	0.51	2.38(3)	0.006	0.65	2.37(2)	0.004	0.81	2.37(4)	0.002	0.85	2.36(5)	0.004	1.08	2.37(3)	0.003
Se-As	1.49	2.41(6)	0.004	1.36	2.41(8)	0.005	1.19	2.41(9)	0.003	0.75	2.42(0)	0.007	0.38	2.41(5)	0.006
Se-Se	-	-	-	-	-	-	-	-	-	0.42	2.37(5)	0.002	0.55	2.36(9)	0.004

3.4 Discussion

The coordination environments of Ge, As and Se atoms all obey the 8-*N* rule, implying that the system is a covalently bonded solid. Previous study on the non-reversing heat flow ΔH_{nr} of ternary $Ge_xAs_xSe_{1-2x}$ glasses indicates the existence of the intermediate phase with the presence of quasi-tetrahedral $Se{=}As(Se_{1/2})_3$ structural units [63]. However, the EXAFS data in this work show no evidence for the four-fold coordinated As atoms in addition to the absence of Se=As double bond vibration mode in the Raman spectra. In view of these facts, the claim that $Se{=}As(Se_{1/2})_3$ building blocks can be formed in ternary Ge-As-Se glasses seems to be disputed.

According to the random covalent network model (RCNM), six possible bond types, namely Ge-Se, As-Se, Ge-As, Ge-Ge, As-As, Se-Se bonds should coexist in the Ge-As-Se ternary system. However, based on the Raman and EXAFS spectra results presented in this chapter, only Ge-Se, As-Se and Se-Se bonds could appear in the Se-rich glasses which is not fully consistent with above mentioned structural model. Thus, the chemically ordered network model (CONM) that considering the differences in bond energy seems to become more suitable for explaining the structure evolution of these glasses.

It has been found that when small amount of four-coordinated Ge and three-coordinated As atoms having higher connectivity are added into one dimensional amorphous Se, these elements are randomly dispersed in the glassy matrix. Based on the relationship proposed by Pauling [174], Ge-Se bonds have the highest bond energy among all the possible bonds of the $Ge_xAs_ySe_{100-x-y}$ system. In other words, Ge-Se bonds are expected to form first in the glassy structure until all the Ge atoms are consumed. Since the number of heteropolar bonds should be maximized and the bonds are expected to form in the sequence of decreasing bond energy (Ge-As are weakly polar bonds), it naturally implies that the bonding between As atoms and the residual Se atoms would then become dominant. The long Se chains or ring-like Se segments are thus broken by forming finite $GeSe_{4/2}$ tetrahedral and $AsSe_{3/2}$ pyramidal structural units. Further increasing Ge and As contents will result in a decrease in the number of the Se-Se homopolar bonds (Se-rich < 20 at%) where the glass structure can be described as a continuous network of $GeSe_{4/2}$ tetrahedra and $AsSe_{3/2}$ pyramids separated by short Se chains.

The structure of stoichiometric glasses become complicated and a violation of chemical order is observed in these compositions. CONM assumes that a completely chemical order should occur at the stoichiometric composition where only heteropolar bonds can be formed. However, there are some discrepancies between the theory and experiment as a small amount of homopolar bonds (Ge-Ge, As-As and Se-Se) can be found in the Raman spectra. As a matter of fact, the existence of Se-Se bonds in the stoichiometric binary glasses, such as $GeSe_2$ and As_2Se_3, has been supported by several experimental methods and simulation analysis, even though the estimated ratio of Se involved in the homopolar bonds varies largely [175- 178]. For the Ge-As-Se system, the existence of homopolar bonds seems closely related to the Ge/As ratio. It appears that the number of homopolar bonds can be effectively reduced in ternary stoichiometric compositions by controlling the ratio of Ge/As at a low value (Ge/As < 1).

For the Se-poor glasses, the Raman results indicate that the vibration feature corresponding to Se-Se bonds disappear, whereas the contribution of As-rich fragments containing As-As homopolar bonds become evident in all samples. Since Se atoms always preferentially bond to Ge atoms, the configurational disorder will gradually become high around As atoms when there are insufficient Se atoms to produce stable $AsSe_{3/2}$ pyramidal units. Se deficiency is then balanced by the appearance of As-rich clusters in the form of either polymeric Se_2As-$AsSe_2$ structural units or monomeric cage-like As_4Se_4 molecules [179]. Note that no sharp Raman peaks indicative of As_4Se_4 molecules are observed in these glasses, which suggests that As_4Se_4 molecules do not exist as isolated monomers in the structure. It appears that As-rich phases still connect to the other structural units and function as a part of the network backbone. The absence of Ge-Ge homopolar bonds in Se-poor glasses is supported by Raman and EXAFS spectra. This result is consistent with previous studies [41,180]. It also reinforces the idea that Se deficiency causes the formation of As-As homopolar bonds in the first place, Ge-Ge homopolar bonds only start to appear in extremely Se-poor (> 50 at%) glasses.

3.5 Conclusions

The short-range structural characteristics of $Ge_xAs_ySe_{100-x-y}$ bulk glass have been investigated by Raman spectra and X-ray absorption fine structure spectroscopy (EXAFS). It has been found that the chemically ordered network model can be used to effectively describe the structure of Se-rich glasses, which is mainly composed of $GeSe_{4/2}$ tetrahedra and $AsSe_{3/2}$ pyramids connected by the Se chain fragments with various lengths. The existence of homopolar bonds has been confirmed in the stoichiometric glasses with high Ge/As ratio as a sign of small deviation from chemical order. Se-poor glasses contain As-rich phases with no trace of 4-fold coordinated Arsenic structure unit ($Se=AsSe_{3/2}$). As atoms tend to cluster together leading to a minimal number of Ge-Ge homopolar bonds in these glasses. There is no identification of nanoscale phase separation since weakly bound isolated As-rich molecules are not observed in Se-poor glasses. Overall, the network connectivity of ternary $Ge_xAs_ySe_{100-x-y}$ glass system steadily increases from Se-rich through stoichiometric to Se-poor compositions.

Chapter 4

Thermal Properties of Ge-As-Se Glasses

4.1 Introduction

The nature of the glass transition is one of the most important but unsolved problems in the scientific community. It relates to the question of how structure changes when glass-forming liquids are cooled. A generally accepted notion is that the glass transition is a kinetic transition arising from the competition between the cooling rate and the time for structural relaxation. The process involves two important characteristics: the glass transition temperature (T_g) and sub-T_g relaxation. If the glass is held isothermally at a temperature below T_g, the system will evolves towards an equilibrium state via atomic rearrangement. This is also known as sub-T_g relaxation and leads to changes in the properties of the glass. Glass transition temperature T_g is a critical thermal parameter for characterization of glassy materials, which acts as an indication of changes in the connectivity and rigidity of glassy network. It has been pointed out that, for a given chalcogenide glass system, increasing the relative atomic mass of the chalcogen or its proportion in the glass will lead to a decrease in T_g owing to the reduced average bond strength [37]. Investigations on the T_g trends in $Ge_xAs_ySe_{100-x-y}$ ternary chalcogenide glasses therefore will be helpful for investigating the possible structural arrangements in this system.

Thermal analysis techniques, such as differential scanning calorimetry (DSC), thermogravimetric analysis (TGA) and thermomechanical analysis (TMA), enable a better understanding of the influence of temperature dynamics on a material's behavior. Among those, DSC measures changes in heat flow as a function of temperature or time. These changes are recorded as peaks in DSC curves (Figure 4.1). The peak area relates to the change of enthalpy and peak direction indicates whether the thermal event is endothermic or exothermic. This measurement is applicable to various types of materials and is easy to undertake. It allows the detection of transformations taking place in a sample, such as melting, the glass transition, phase changes and crystallization. For these reasons, DSC is the most common approach used in the laboratory for determining the glass transition temperature and for acquiring useful information about relaxation effects in glasses. Temperature-modulated differential scanning calorimetry (MDSC) is a new variant of DSC and has been applied to study glass transition of chalcogenide glasses. A programmed sinusoidal temperature profile is superposed on the liner heating ramp during the scan, then the total heat flow can be deconvoluted into two parts. One part tracks the temperature modulation and is known as the reversible heat-flow, which can be used to obtain T_g. Another one does not track the temperature modulation and is known as the non-reversing heat-flow, which can be used to obtain non-reversing enthalpy (ΔH_{nr}). Vanishing of ΔH_{nr} features the existence of intermediate phase in network glasses [181].

For various applications in photonics, the preparation of high quality chalcogenide thin films with stable physical properties has become the necessary prerequisite. Our previous work has reported that as-deposited $Ge_xAs_ySe_{100-x-y}$ thin films with mean coordination number $<r> \sim 2.45$ are thermally stable and have a bulk-like linear refractive index [182]. Recently, photostable thin films with $<r>$ in between 2.45 and 2.50 were also found in thermally evaporated $Ge_xAs_ySe_{100-x-y}$ film by members of our group [183]. Structural analysis confirmed that the stoichiometry and bond configurations of these particular films are basically the same as those present in bulk source materials, in spite of the fact they are formed under non-equilibrium conditions involving phase changes. The similarity in the bond structure of the as-deposited films and bulk glasses is believed to play an important role in controlling thermal and optical properties of thin films rather than the ratio of Ge/As [184]. It is interesting, therefore, to investigate whether existence of stable films with bulk-like properties requires some specific and definable property of the glass.

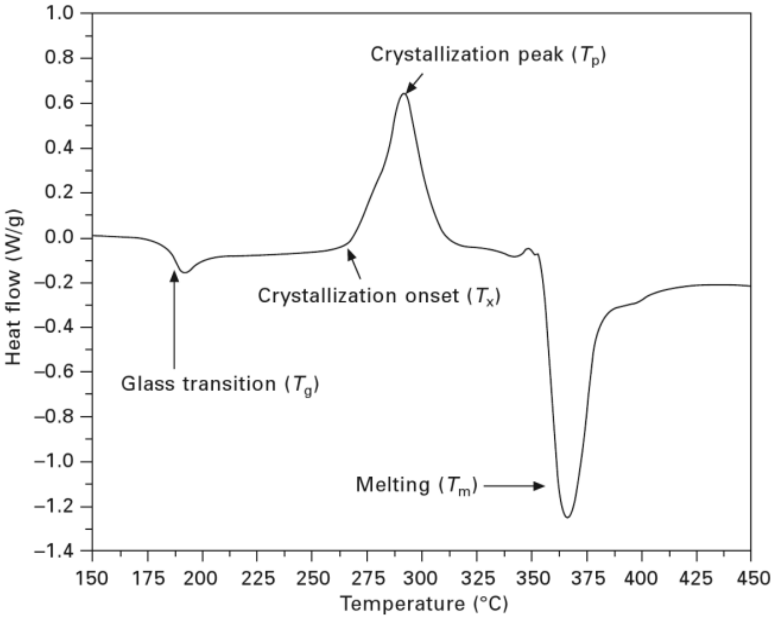

Figure 4.1. Typical DSC curve for a multicomponent chalcogenide glass [185].

In this chapter, therefore, the structural relaxation properties of glass forming liquids have been investigated by DSC. The composition dependences of the glass transition temperature (T_g), the activation energy for structural enthalpy relaxation (E_a) and the fragility index (m) have been measured. The resulting trends are used to rationalize previous empirical observations on both relaxation and photostability behavior of this family of glass.

4.2 Experiments

34 samples of $Ge_xAs_ySe_{100-x-y}$ glasses with compositions distributed across the glass forming region and covering a wide range of stoichiometry and mean coordination number were prepared. Details about sample preparation procedures have been described in **Section 3.2**.

DSC measurements were performed using a Mettler Toledo DSC1 equipped with an intercooler, and the data were analyzed with the STARe software. Indium and zinc standards were used to calibrate the temperature scale. About 20 mg of powder for each sample was sealed into an aluminum pan. In order to erase the thermal history of the glasses, all the studied samples were first heated far above T_g but below the crystallization onset temperature T_x then cooled far below T_g and reheated at the same rate. The temperature was scanned over a range from room temperature to 480 °C with different heating/cooling rates at 5, 10, 14, 20 and 30K/min, respectively, under a uniform nitrogen gas flow of 50 mL/min.

The chemical compositions of the glasses are reported in Table 4.1 and illustrated in Figure 4.2. The samples can be categorized as follows: (1) 20 compositions which can be divided into 5 groups with the same <*r*> = 2.30, 2.40, 2.50, 2.55 and 2.72, respectively (depicted by colored dots in Figure 4.2) (2) 14 other compositions distributed across the glass forming region (depicted by black dots in Figure 4.2).

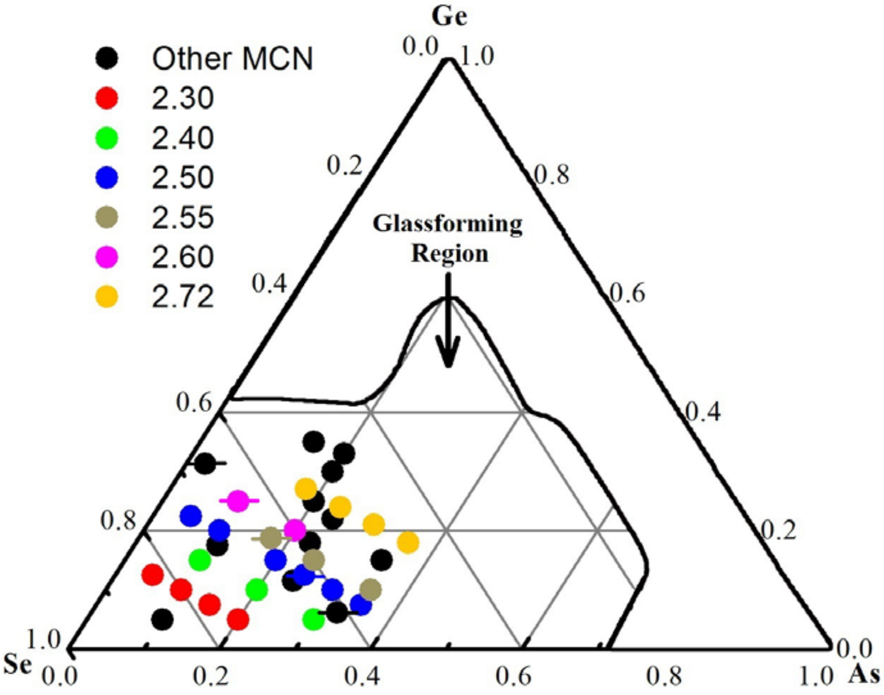

Figure 4.2. Glass formation domain of the $Ge_xAs_ySe_{100-x-y}$ ternary system showing the 34 compositions investigated in this study, color-coded according to their mean coordination number. Five stoichiometric compositions are marked as solid circles with horizontal lines through them.

4.3 Results

Figure 4.3(a) shows DSC traces obtained at heating rates ranging from 5 to 30 K/min for the $Ge_{6.25}As_{32.5}Se_{61.25}$ (<*r*> = 2.45) sample. The variation of T_g as a function of the mean coordination number <*r*> is shown in Figure 4.4. The value of T_g is shown to increase linearly with increasing <r>. It has been well established that the value of T_g closely correlates with the connectivity and rigidity of the vitreous network [186]. Indeed, increasing the concentration of the network forming elements such as Ge or As should lead to increased T_g, as is shown in the data. No global maximum was observed, which is consistent with earlier reported results [187].

The dependence of the glass transition temperature on the heating rate (Q) was found to obey the following equation [188]:

$$\frac{\mathrm{d}\ \ln \mathrm{Q}}{\mathrm{d}\left(\dfrac{1}{T_g}\right)} = -\frac{E_a}{R} \tag{4.1}$$

where E_a and R are the activation energy for the glass transition and the ideal gas constant, respectively. The variation of ln Q as a function of $1000/T_g$ is shown in Figure 4.3(b) for a series of representative glass samples with different <r> values. A linear dependence was obtained, and the activation energy E_a was then calculated from the slope of these plots.

The variation of E_a as a function of mean coordination number is displayed in Figure 4.5(a) and shows a sharp local minimum at <r> = 2.40. For comparison the variation of E_a is also plotted as a function of the departure from stoichiometry quantified as the degree to which the glasses were Se-rich or Se-poor. The data shown in Figure 4.5(b) exhibit much more scatter than those in Figure 4.5(a) especially for Se-poor glasses, although a very broad minimum is found for compositions containing a slight excess of Selenium. The E_a for Se-rich glasses are relatively lower than those for Se-poor ones.

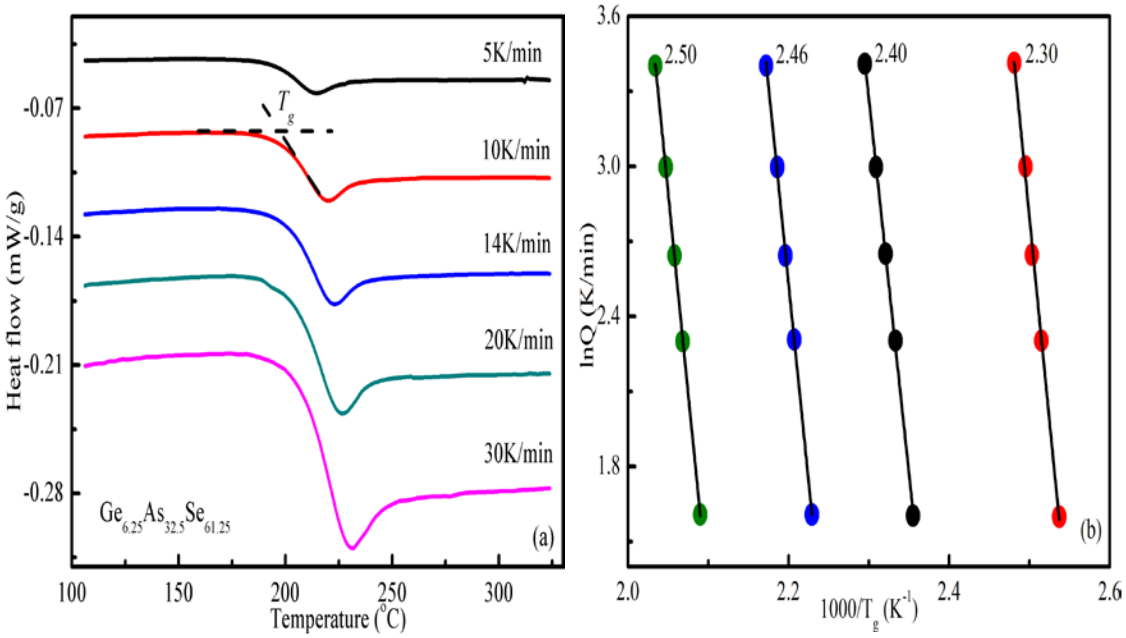

Figure 4.3. (a) DSC curves of a $Ge_{6.25}As_{32.5}Se_{61.25}$ glass obtained at different heating rates after cooling at the same rate from far above T_g. (b) Plot of ln Q as a function of 1000/T_g, showing the linear regression used to obtain E_a for the following glass compositions: $Ge_{10}As_{10}Se_{80}$ (<*r*> = 2.30), $Ge_{10}As_{20}Se_{70}$ (<*r*> = 2.40), $Ge_{17.5}As_{11}Se_{71.5}$ (<*r*> = 2.46) and $Ge_{22.5}As_{5}Se_{72.5}$ (<*r*> = 2.50).

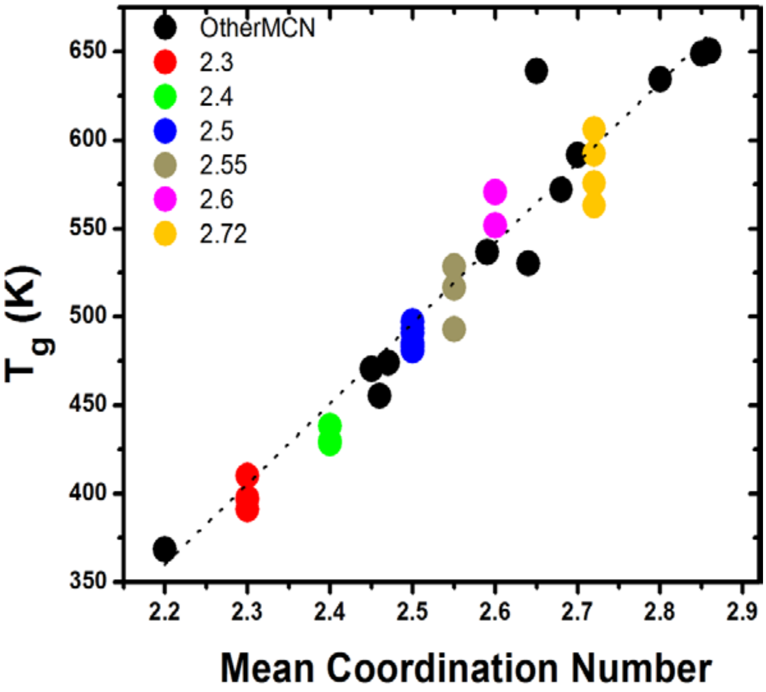

Figure 4.4. T_g as a function of mean coordination number at heating/cooling rate of 10K/min.

Table 4.1. Compositions and respective mean coordination number (<*r*>), glass transition temperature (T_g), activation energies (E_a) and fragility index (*m*) for $Ge_xAs_ySe_{100-x-y}$ glasses.

Compositions Ge-As-Se (at%)	<*r*>	Se-rich/-poor (at%)	T_g (°C)	E_a (kJ/mol)	*m*
5-10-85	2.20	+60	95.44	285.61	40.54
17.5-11-71.5	2.46	+20	182.22	258.57	29.93
11.5-24-64.5	2.47	+5.5	200.99	259.15	28.59
18-23-59	2.59	-11.5	263.39	304.91	29.73
20-20-60	2.60	-10	278.50	318.41	30.19
15-34-51	2.64	-30	257.16	332.88	32.79
22-24-54	2.68	-26	298.79	353.14	32.25
25-20-55	2.70	-25	318.41	367.61	32.43
30-20-50	2.80	-40	361.11	402.35	33.15
35-15-50	2.85	-42.5	375.85	422.61	33.98
33-20-47	2.86	-49	377.31	429.37	34.45
5-20-75	2.30	+35	136.88	262.44	33.43
7.5-15-77.5	2.30	+40	123.63	262.44	34.58
10-10-80	2.30	+45	124.39	268.23	35.20
12.5-5-82.5	2.30	+50	117.99	274.02	36.64
5-30-65	2.40	+10	165.16	241.21	28.77
10-20-70	2.40	+20	155.37	246.04	29.98
15-10-75	2.40	+30	156.78	251.83	30.60
7.5-35-57.5	2.50	-10	210.29	276.92	29.90
10-30-60	2.50	-5	220.23	273.06	28.93
12.5-25-62.5	2.50	0	224.32	266.30	27.98
15-20-65	2.50	+5	217.68	264.37	28.13
20-10-70	2.50	+15	207.78	265.34	28.81
22.5-5-72.5	2.50	+20	212.13	273.58	29.32
18.75-17.5-63.75	2.55	0	255.37	283.67	28.00
15-25-60	2.55	-7.5	243.35	289.46	29.30
10-35-55	2.55	-17.5	219.90	293.32	31.04
27-18-55	2.72	-26	332.88	357.96	30.89
24-24-52	2.72	-32	318.97	363.75	32.13
21-30-49	2.72	-38	302.63	370.51	33.63
18-36-46	2.72	-44	289.74	375.33	34.82
6.25-32.5-61.25	2.45	0	197.56	249.91	27.70
25-10-65	2.60	0	297.45	305.86	28.02
31.25-2.5-66.25	2.65	0	365.80	341.56	27.94

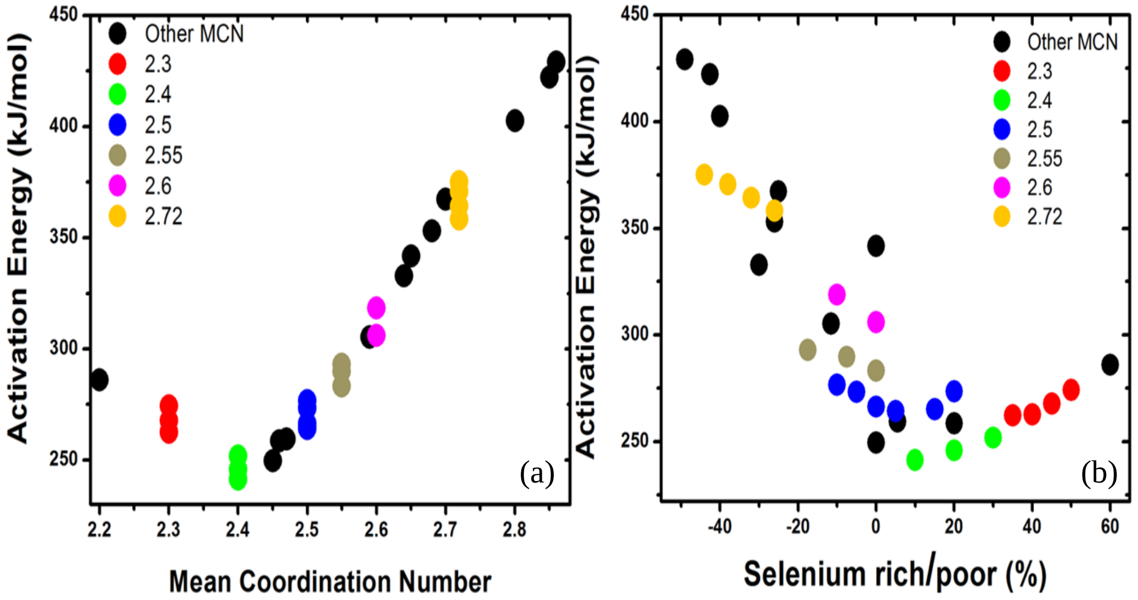

Figure 4.5. E_a (a) as a function of mean coordination number and (b) as a function of departure from stoichiometry in atomic percent of selenium.

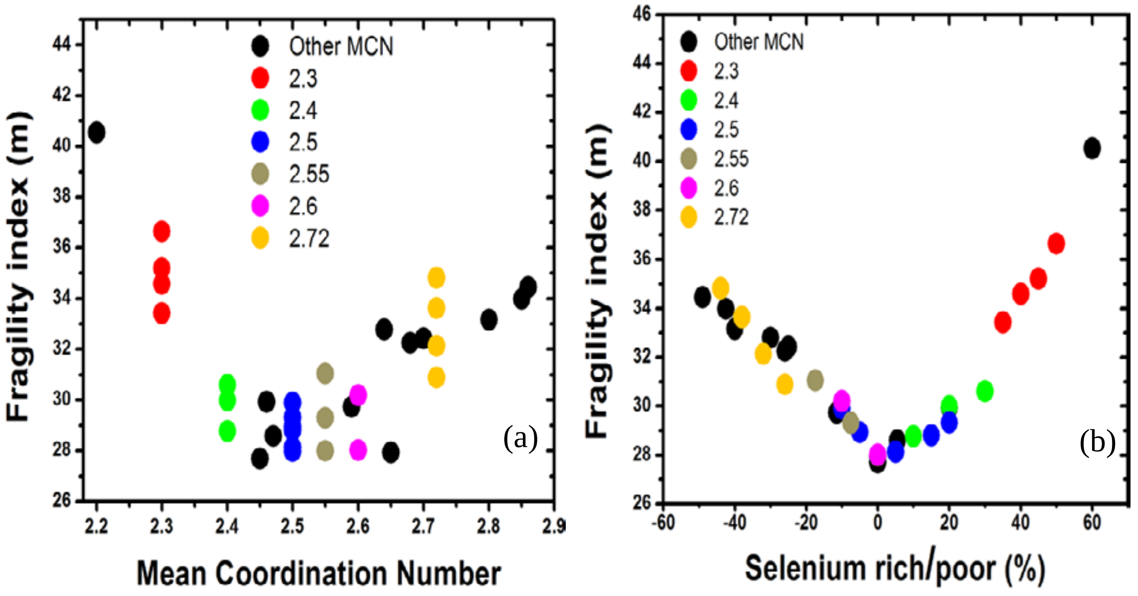

Figure 4.6. Fragility index as a function of (a) mean coordination number and (b) departure from stoichiometry in atomic percent of selenium.

The fragility or steepness index *m* characterizes and quantifies the extent to which glass forming liquids depart from the Arrhenius viscosity behavior as they approach the glass transition region. The fragility index can be calculated from T_g and E_a using the relation [189,190]:

$$m = \frac{E_a}{RT_{g*} \ln 10} \tag{4.2}$$

where E_a is the activation energy and T_{g*} is the glass transition temperature at heating/cooling rate of 10K/min. The fragility index for the complete set of glasses is plotted as a function of <*r*> and departure from equilibrium in Figure 4.6(a), (b) respectively. No clear trend is visible between fragility and mean coordination number <*r*> as depicted on Figure 4.6(a), although there is a very broad minimum of *m* at the intermediate values of <*r*>. In the region of <*r*> between 2.45 - 2.60 where stoichiometric compositions can exist, changes in fragility index are relatively small compared with those that occur at smaller and larger <*r*>. On the other hand, the fragility index exhibits a sharp minimum for glasses with stoichiometric compositions. Compositions containing an excess or deficiency in Se both become distinctly more fragile with increasing departure from stoichiometry. The sharp minimum in fragility is exemplified by the fact that all five stoichiometric samples almost perfectly overlap on Figure 4.6(b).

4.4 Discussion

4.4.1 Liquid, fragility and stoichiometry

The mean coordination is often invoked to explain various features of chalcogenide glasses; however, the results of Figure 4.6(b) emphasize that simple chemical effects such as deviation from stoichiometry appear to be more relevant in predicting fundamental physical properties such as fragility in the Ge-As-Se system. Indeed, the mean coordination is only properly defined at low temperature where all topological constraints are still intact. It can therefore be effectively correlated to low temperature properties such as molar volume [191] but may be inappropriate for predicting behaviors above T_g. As shown in Figure 4.5(a), the activation energy at T_g may correlate with $<r>$ because it reflects the energy required to gain mobility relative to a state where all constraints are intact. On the other hand, the fragility is defined by the rate at which these constraints are broken with increasing temperature above T_g, and this process appears to be rather independent of the mean coordination but instead is controlled by the departure from stoichiometry. A similar correlation between fragility index and deviation from stoichiometry has been observed in the Ge-As-S system [192], which again highlights the leading role of chemical stoichiometry in controlling thermodynamic fragility of chalcogenide glass-formers.

The cooperative relaxation theory of Adam Gibbs has been widely used to explain the transport properties and fragility of glass forming liquids. It constitutes the basis for some of the most recent viscosity models [193], and it is commonly used to correlate energy landscape formalisms and viscosity [76,194]. Its success derives from its explicit correlation between configurational entropy (S_c) and transport properties of supercooled liquids according to:

$$\eta = \eta_0 \exp \frac{C}{TS_c} \tag{4.3}$$

where η is the viscosity and η_0 and C are constants. Below we discuss how the structural features of Ge-As-Se glasses may affect the configurational entropy of the supercooled liquid and in turn the compositional dependence of the fragility in terms of energy landscape.

From an energy landscape point of view (Figure 4.7(a)), the fragility of a glass forming liquid can be correlated to the topography of the corresponding landscape (Figure 4.7(b)) [76,195,196]. A strong landscape has a uniform topology with basins (or local minima) of similar depth separated by saddles of similar height that progressively lead down to a general energy minimum (metabasin) corresponding to the ideal glass at the bottom of the landscape (upper part of Figure 4.7(b)). The activation energy required to sample neighboring basins during relaxation is therefore similar at high temperature (near the top of the landscape) and at low temperature (near the bottom of the landscape) thereby indicating an Arrhenius behavior characteristic of strong liquids. On the other hand, fragile landscapes have nonuniform topology with a high density of shallow basins at the top of the landscape interspersed between widely separated deep minima (lower part of Figure 4.7(b)). Sampling basins at high temperature therefore involve a small activation energy requiring the rearrangement of a few molecules. At low temperature, however, sampling widely separated basins involves the rearrangement of many molecules and overcoming large energy barriers (referred to as metabasin-metabasin transitions). The activation energy therefore increases steeply near T_g in a non-Arrhenius way characteristic of fragile glasses.

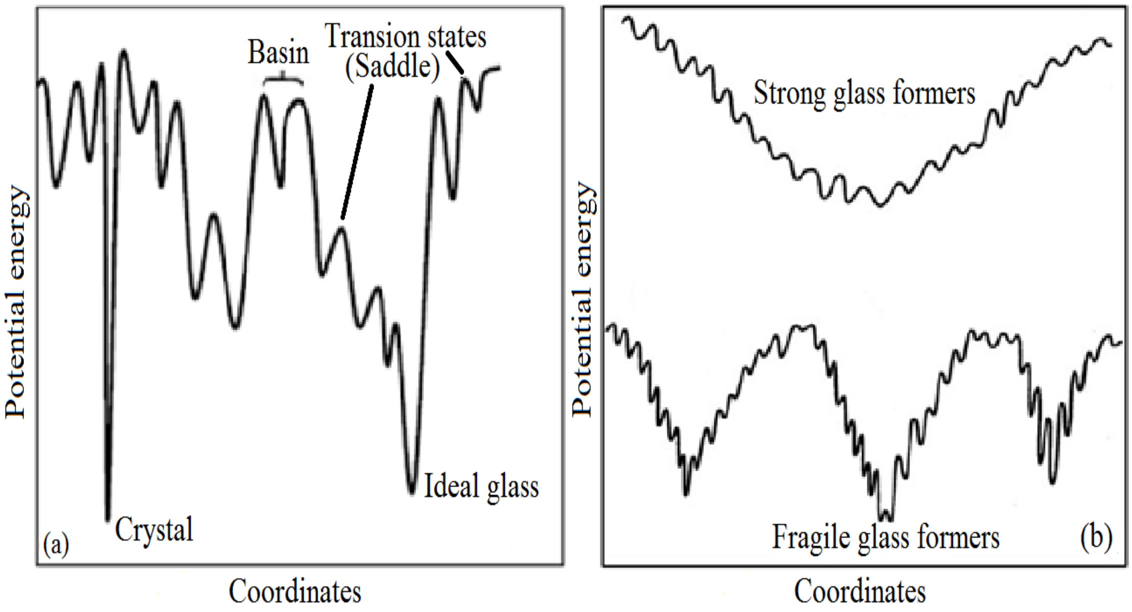

Figure 4.7. (a) Schematic illustration of an energy landscape; (b) Schematic illustration of the topographic distinction between energy landscapes for strong and fragile glass formers [76]. The potential energy increases in the vertical direction, and the horizontal direction represents all configurational coordinates.

The energy landscape formalism is consistent with the thermodynamic features observed in Ge-As-Se glasses. Stoichiometric glasses contain mainly heteropolar bonds [41] that require similar energy to be broken [197] and should therefore result in a uniform type of energy barrier throughout the entire landscape in a way similar to SiO_2 [76]. This feature leads to strong glass formers behavior (lowest fragility index) as observed experimentally in Figure 4.6(b). On the other hand, Se-rich compositions contain a disparity of structural domains exhibiting floppy and rigid behavior which can be associated with different well depths including shallow potential wells from floppy selenium chains and deeper wells from rigid heteropolar regions. A similarly heterogeneous topography is generated in Se-poor glasses where homopolar bonds (As-As bonds as described in **Section 3.3.1**) introduce shallow wells that can be easily sampled and result in greater degrees of freedom characteristic of fragile systems. Stoichiometric factors therefore appear to largely define the energy landscape topology of Ge-As-Se glasses and in turn their fragility.

4.4.2 Fragility and structural relaxation in glasses

The temperature dependence of melt viscosities is critical to most industrial glass fabrication processes such as molding, drawing, and floating, *etc*. An accurate knowledge of the fragility is, therefore, critical to optimize processes involving the liquid phase. However, the fragility is also a useful factor in predicting some properties of the glass below T_g. Indeed the fragility defines the rate at which the system departs from equilibrium upon losing ergodicity (ergodicity refers to the equivalence of time and ensemble averages of thermodynamic properties of a system. For glassy state, the system has insufficient time to relax to the equilibrium during the observation time of measurement, indicating that the condition of ergodicity is not satisfied and giving rise to the loss of ergodicity or broken ergodicity), and consequently it controls the glass tendency to undergo structural relaxation below T_g. This is particularly relevant for chalcogenide glasses because their low T_g enables significant relaxation processes even at room temperature [66,198]. The correlation between sub-T_g relaxation and fragility can be qualitatively illustrated by extrapolating fragility plots below the glass transition, as shown in Figure 4.8(a) for three hypothetical glass forming liquids spanning the whole range of fragility with m = 16, 55, and 200. These curves are plots of a modified version of the Vogel-Tamman-Fulcher (VTF) equation [199] that is normally used to fit viscosity data but has been converted to reduced entropy units following the analogy found by Martinez and Angell between excess entropy and viscosity for a wide range of glass forming liquids [200]. The excess entropy is scaled to its value at T_g, and the temperature is scaled to T_g so that each glass forming system can be compared on the same master curve. This provides a qualitative illustration of the entropy variation in glass formers with various m values. Of particular interest is the low temperature part of the plot in the region below T_g. The horizontal dashed line represents the frozen excess entropy of the glass that has solidified at T_g, while the solid lines represent the equilibrium entropy of the corresponding liquids cooled infinitely slowly. This plot then illustrates the departure from equilibrium of various glass formers as they vitrify at T_g.

To more clearly illustrate the correlation between fragility and the tendency for relaxation, the low T_g data in Figure 4.8(a) have been replotted in reversed units in Figure 4.8(b) in a form reminiscent of a Kauzmann plot for the same three glass formers, although the expected curvature for S_{exc} is not reflected due to the simplistic equation used. Nevertheless, Figure 4.8(b) qualitatively illustrates how fragile glassy systems depart from equilibrium at a faster rate than strong systems and consequently build up a larger driving force and large propensity for relaxation as the temperature drops below T_g. This is of prime importance for sensitive applications such as integrated infrared optics where relaxation processes can lead to volume and refractive index changes that may impair the device functions [8,182,201]. In this case, strong glasses with minimal tendency for relaxation are the optimal choice of material. In that respect, the results of Figure 4.6(b) effectively explain previous experimental results which showed that Ge-As-Se films of near stoichiometric compositions exhibited negligible relaxation upon annealing near T_g while far off-stoichiometry compositions exhibited significant relaxation, even those with a mean coordination of <*r*> = 2.40 [182]. Sub-T_g relaxation is therefore controlled by stoichiometric factors rather than topological factors.

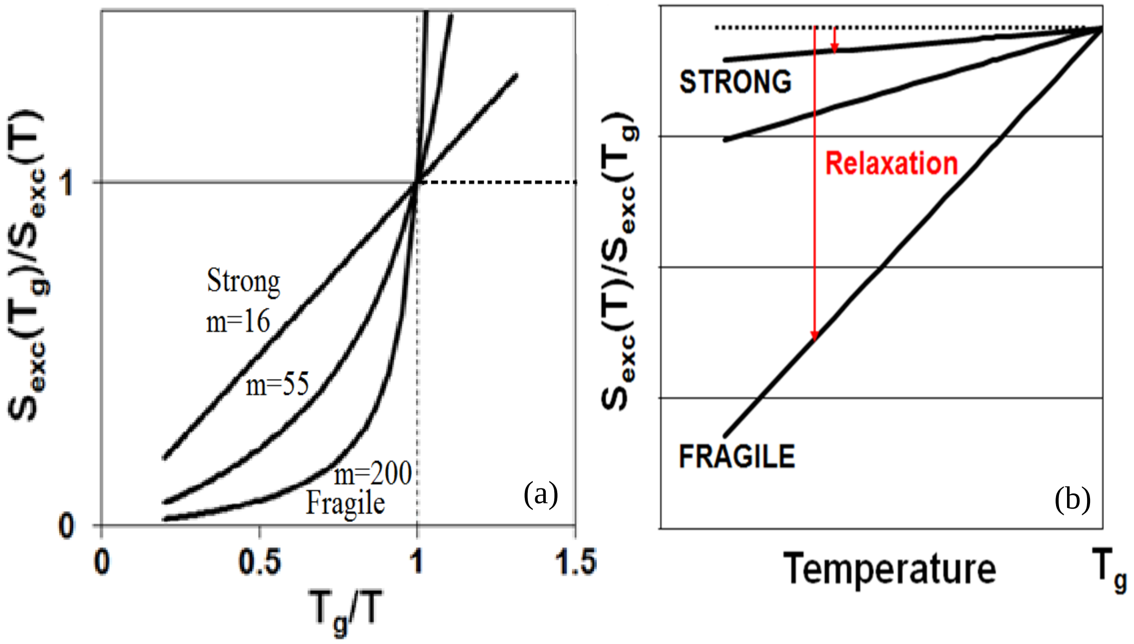

Figure 4.8. (a) Schematic representation of three hypothetical glass formers based on a modified VTF equation with *m* ranging from 16 to 200; (b) Variation of the equilibrium excess entropy below T_g in comparison to the value frozen at T_g showing the build up of the driving force for relaxation for glass formers of different *m*.

Studies of Ge-As-Se film samples suggest that glass compositions falling into a narrow region of <*r*> (around 2.45 - 2.50) seem to have the characteristics of strong glass formers where their structures do not change much through the transition. The results of Figure 4.6(a) give a direct evidence by demonstrating that the values of *m* are relatively smaller when <*r*> lies in the same region mentioned above, despite different compositions. Thermodynamically strong glasses acquire structural degrees of freedom at a lower rate than fragile glasses, resulting in a well preserved short- to medium-range order in vapors and thin films. Homogeneous structure with the least amount of homopolar bonds or molecular species manages to enhance thermal stability and reduce photosensitivity of these thin films. From this aspect, attempts to optimize the intrinsic chemical composition by suppress the formation of homopolar bonds as the means of obtaining stable films in Ge-As-Se glasses are viable and effective.

4.4.3 Absence of an intermediate phase

An intermediate phase has been previously suggested in the Ge-As-Se system using MDSC measurements performed on a subset of Ge-As-Se samples [63]. However, the present experimental data indicate that no intermediate phase is generally present in these glasses. Instead Figures 4.5(a) and 4.6(a) show a sharp minimum in transport properties at $<r> = 2.40$. This difference most likely arises from the fact that intermediate phases in chalcogenide glasses are only observed using measurements of nonreversible enthalpy (ΔH_{nr}). Yet it has been argued since the early days of MDSC that the nonreversible enthalpy does not have a well-defined physical meaning [202] and cannot be equated to the enthalpy relaxation [203]. Instead the MDSC signal should be interpreted in term of heat capacity spectroscopy using the real and imaginary components of the complex heat capacity [204-207]. This suggests that the observation of an intermediate phase in Ge-As-Se glasses is likely the result of an instrumental artifact associated with the nonreversible quantity ΔH_{nr}.

Similarly, the non-aging window observed in these glasses [62,208,209] is likely an artifact of experimental conditions. Indeed Figure 4.8 clearly shows that a glass falls out of thermodynamic equilibrium as it goes through T_g and significantly departs from its equilibrium entropy no matter how strong it is. A finite driving force for relaxation must therefore build up for any glass, but aging/relaxation can be kinetically prevented if the structural relaxation time is much longer than the observation time when low annealing temperatures are used. Nevertheless, raising the annealing temperature closer to T_g permits reduction of this relaxation time to the observation time scale. This was recently demonstrated by Zhao *et al.* in a series of Ge-Se glasses [65] which showed large relaxation effects for all glasses including compositions from the so-called “non-aging window” [62]. The magnitude of the relaxation enthalpy was shown to correlate well with the fragile behavior of the glasses, as expected from Figure 4.8(b). An identical observation was made by Calvez *et al.* in the Ge-As-Se system [210], where strong compositions relaxed significantly less that fragile ones when annealed at a fixed temperature below T_g. In addition, Shpotyuk *et al.* have reported that, marginality of ΔH_{nr} recorded for as-prepared or short-time aged glasses is not a sufficient criterion for identification of self-organized intermediate phases in chalcogenide glasses, especially for those with higer T_{g} [211]. For more reliable results on physical aging in a glass, the MDSC measurements should be repeated during relatively long time period. The absence of relaxation previously observed in the non-aging window is therefore likely the result of the low annealing temperature used in these experiments (room temperature [62,208,209]) far below T_g, where relaxation times quickly reach geological time scales and no slow relaxation process can be observed within the short measurement time.

4.5 Conclusions

The thermodynamic properties of a large number of Ge-As-Se glasses were measured using Differential Scanning Calorimetry. The activation energy for enthalpy relaxation shows a sharp minimum at the percolation threshold $<r> = 2.40$ but no clear trend with departure from stoichiometry. On the other hand, the fragility index shows a global minimum for glasses of stoichiometric compositions while no clear tendency is obtained as a function of $<r>$. These data reflect that chemical effects such as departure from stoichiometry appear to largely control the transport properties over a wide temperature range and in turn must control the topology of the energy landscape. Ge-As-Se glasses are of particular interest for integrated optic applications due to their high nonlinearity and wide optical transparency. However, their low T_g may result in significant relaxation during the lifetime of a device which could impair proper function. Selection of glass composition with minimal propensity for relaxation is, therefore, desirable. In that respect, a strong glass former with a high T_g would show a minimal driving force for relaxation and very slow relaxation kinetics which should be optimal for sensitive applications. The present results indicate that stoichiometry rather than mean coordination (topological effects) is the most relevant selection criteria for selecting such glasses. The existence of strong glass formers is confirmed within a specific range of mean coordination number. These findings rationalize previous experimental observation of thermal stability and photostable in Ge-As-Se thin film. Glass compositions, such as $Ge_{11.5}As_{24}Se_{64.5}$ and $Ge_{15}As_{20}Se_{65}$, with $<r> = 2.45$-2.50, high T_g and low m seem to be the best candidates for photonic device fabrication.

Chapter 5

Elastic Properties of Ge-As-Se Glasses

5.1 Introduction

As an important mechanical property, the elasticity of glasses reflects the structural characteristics of the material, including the interatomic bonding energy and the degree of polymerization. This connection was first discussed by He and Thorpe who calculated the elastic moduli of a series of glassy networks with different mean coordination number $\langle r \rangle$ [212]. The results showed that the elastic properties of the network are predominantly controlled by $\langle r \rangle$. An exponential increase in the elastic moduli starts to occur at $\langle r \rangle = 2.40$ where the rigidity is said to percolate through the structure and an elastically floppy network starts to become rigid. This simulation result was soon confirmed by an experiment designed to measure the elastic constants of Ge-As-Se systems [52]. Some other experiments, however, reported that elastic constants do not show a transition at such rigidity percolation threshold in Ge-Se and Ge-As-S glasses [213,214]. Instead, the elastic transitions were observed at higher values of $\langle r \rangle \approx 2.70$. Impurities in glass samples (contaminated by oxygen and some metal ions) and the neglect of medium-range structural order in the calculation are believed to be the main reasons for the discrepancy between experimental and theoretical investigations. It appears that chalcogenide glasses with $\langle r \rangle$ between 2.40 and 2.70 have a structural order of layer types, which evolves to a 3D rigidity phase at

<*r*> = 2.67 [215]. The layered structure consists of different atoms arranged in a two-dimensional sheet with intra-layer strong covalent bonds and inter-layer weak van der Waals bonds. The direct experimental evidence for the existence of medium-range order in chalcogenide glasses have come from the X-ray diffraction patterns [57,58]. The presence of so-called first sharp diffraction peak (FSDP) at low diffraction angles has been widely accepted as a signature of the layer structure. The position of FSDP relates to the distance between the layers, and the width of FSDP reflects the structural correlation length for the medium-range order [1]. In addition, simulations also provide evidence in favor of a structure with layer-like configurations in chalcogenides [215,216]. Meanwhile, the composition dependence of other physical properties, *e.g.* the high pressure resistivity in Ge-As-Te glasses [217], and the optical bandgap and thermal conductivity in Ge-Sb-Se glasses [218], all exhibit transition behaviors around <*r*> = 2.60. These experimental results on the correlation between <*r*> and various physical properties can be interpreted by the changes in the network topology due to the formation and development of a layered structure in the same way. It seems that the correlation between elastic properties and mean coordination number provides some insight into the short- and medium-range structural orders in chalcogenide glasses. Apart from the above-mentioned thresholds, elastic properties of several chalcogenide glasses show a distinct slope change at certain specific values of <*r*>, which is known as the chemical threshold [53,219]. The definition of chemical threshold, as yet, seems to be quite ambiguous [220], it has been found that this transition normally occurs at the stoichiometric composition in a glass system [221-224].

Chalcogenide glasses are relatively soft materials with Young's modulus $E < 25$ GPa and Poisson's ratio $v > 0.25$ respectively [84]. The elastic properties of chalcogenide glasses can be determined from calculations based on the measurement of densities and wave velocities. The density of bulk glasses are normally determined by the Archimedes method. The interferometric technique is one of the dynamic methods which is widely used to determine the elastic moduli of glasses and yield a relative high accuracy. During the experiment, a pair of phase-coherent pulses are first applied to a piezoelectric transducer and this is used to generate elastic waves, either longitudinal or transverse depending upon the polarization of the transducer, in a sample. When the wave propagates through that sample, reflection at the near and far end of the specimen will return to the transducer as an echo. The echo will be then recorded on an oscilloscope. Interference between the echo signals results in a series of alternating maxima and minima in the amplitude of the overlapped echoes as the carrier frequency varies. Each of these extrema corresponds to a situation in which the two-way path contains either an integral or half-integral number p of wavelengths of the elastic wave. Equivalently, the two-way travel time t contains the same integral or half-integral number p of carrier frequency periods ($1/f$), therefore $t = p/f$. The velocity thus can be calculated via the relation:

$$\text{Velocity} = \frac{d}{t/2} \tag{5.1}$$

where d is the thickness of the sample, t is the two-way travel time of the elastic wave through the sample. The elastic properties are then calculated from the wave velocities and density using the relations outlined in **Section 2.3.2**.

The variation of density (*ρ*), the elastic constants (the shear modulus *G*, Young's modulus *E*, bulk modulus *K* and Poisson's ratio *ν*) and molar volume (V_m) as a function of mean coordination number in $Ge_xAs_ySe_{100-x-y}$ ternary system are presented in this chapter. The results are used to examine topological and chemical threshold behaviors of Ge-As-Se glass system, which provide important information about microstructure and mechanical properties of this series of glass.

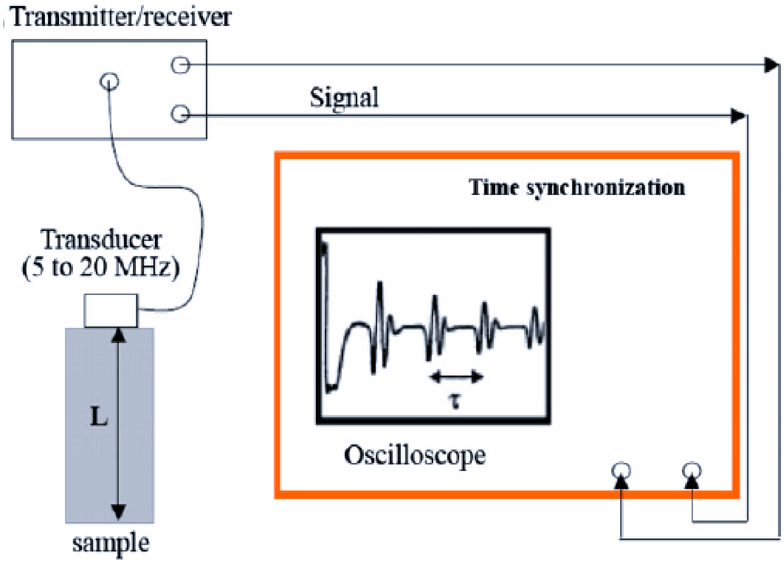

Figure 5.1. The schematic illustrations for the pulse echo overlap ultrasonic method [225].

5.2 Experiments

The density of bulk glass samples (*ρ*) was measured using a Mettler H20 balance with an MgO crystal ($\rho_{MgO} = 3.584$ g/cm^3) serving as a reference. Each sample as well as the reference was weighed five times in air and ethanol respectively at room temperature. The density then can be calculated using the relation:

$$\rho_{\text{sample}} = \frac{\rho_{\text{ethanol}} w_{\text{air}}}{(w_{\text{air}} - w_{\text{ethanol}})} \tag{5.2}$$

where $\rho_{\text{ethanol}} = \frac{\rho_{\text{MgO}}(w'_{\text{air}} - w'_{\text{ethanol}})}{w'_{\text{air}}}$, w_{air} (w'_{air}) and w_{ethanol} (w'_{ethanol}) is the mean value of measured weight of sample (MgO) in the air and in the ethanol respectively.

Ultrasonic pulse interferometry was employed to measure the travel times of both longitudinal and transverse waves through samples at room temperature within the transducer response envelope centered at a resonant frequency of 20 MHz. Polished samples were glued to the acoustic buffer rod to which the compressional or shear mode thin transducer disk was bonded. In order to reduce the effect of the bonding layer between the sample and the transducer, only a small amount of glue was used to keep the thickness of the interface to the minimum. According to the calculated longitudinal (V_l) and transverse wave velocities (V_t), the shear modulus (G), Young's modulus (E), bulk modulus (K) and Poisson's ratio (v) could subsequently be derived using Equation (2.6) - (2.9) described in **Section 2.3.2**. These equations are repeated as follows:

$$E = \rho \frac{3V_l^2 - 4V_t^2}{(V_l/V_t)^2 - 1}$$

$$G = \rho V_t^2$$

$$K = \frac{E}{3(1-2v)}$$

$$v = \frac{E}{2G} - 1$$

The chemical compositions and calculated elastic properties (E, G, K and v) of the $Ge_xAs_ySe_{100-x-y}$ glasses investigated in this study are listed in Table 5.1. The samples could be categorized as follows: (1) 25 compositions which can be divided into 8 groups with the same <*r*> = 2.30, 2.40, 2.50, 2.55, 2.60, 2.70, 2.72 and 2.80, respectively (depicted by colored dots in Figure 5.2); (2) 7 other compositions distributed across the glass-forming region (depicted by black dots in Figure 5.2); (3) $Ge_xAs_{10}Se_{90-x}$ and $Ge_xAs_{20}Se_{80-x}$ system with fixed As concentration (depicted by open dots with crosses and open dots with horizontal lines respectively in Figure 5.2).

5.3 Results

Figure 5.2(a) shows the density of $Ge_xAs_ySe_{100-x-y}$ glasses as a function of mean coordination number $<r>$. On average, the density increases with increasing $<r>$ up to $<r> \approx 2.40$ and then decreases until $<r> \approx 2.65$, which is followed by a sharp increase above $<r> = 2.70$. The same general pattern is more obvious for the $Ge_xAs_{10}Se_{90-x}$ and $Ge_xAs_{20}Se_{80-x}$ glasses with fixed As concentration. Two extrema, the maximum at $<r> = 2.40$ and the minimum at $<r> \approx 2.65$ are observed. At the stoichiometric composition $Ge_{25}As_{10}Se_{65}$ corresponding to $<r> = 2.60$, no local extremum or a change in slope was observed, indicating the absence of chemical threshold in the $Ge_xAs_{10}Se_{90-x}$ system. Compositions with higher As concentrations but the same Ge content exhibit higher densities. The effect of chemical compositions can be clearly seen for the eight families with the same $<r>$ respectively where the scatter in density arising from different chemical compositions vary between 0.064 g/cm^3 ($<r> = 2.70$) and 0.111 g/cm^3 ($<r> = 2.40$).

The molar volume, V_m, of the glass correlates with the molar mass and density, which can be expressed as:

$$V_m = \frac{\sum_i x_i M_i}{\rho} \tag{5.3}$$

where x_i, M_i are the atomic fraction and the atomic weight the *i*th element of the glass, respectively and ρ is the measured density of the glass. The molar volume for the complete set of glasses is plotted as a function of <*r*> in Figure 5.2(b). The general trend towards a local minimum at <*r*> ≈ 2.40 and a local maximum at <*r*> ≈ 2.65 can be observed.

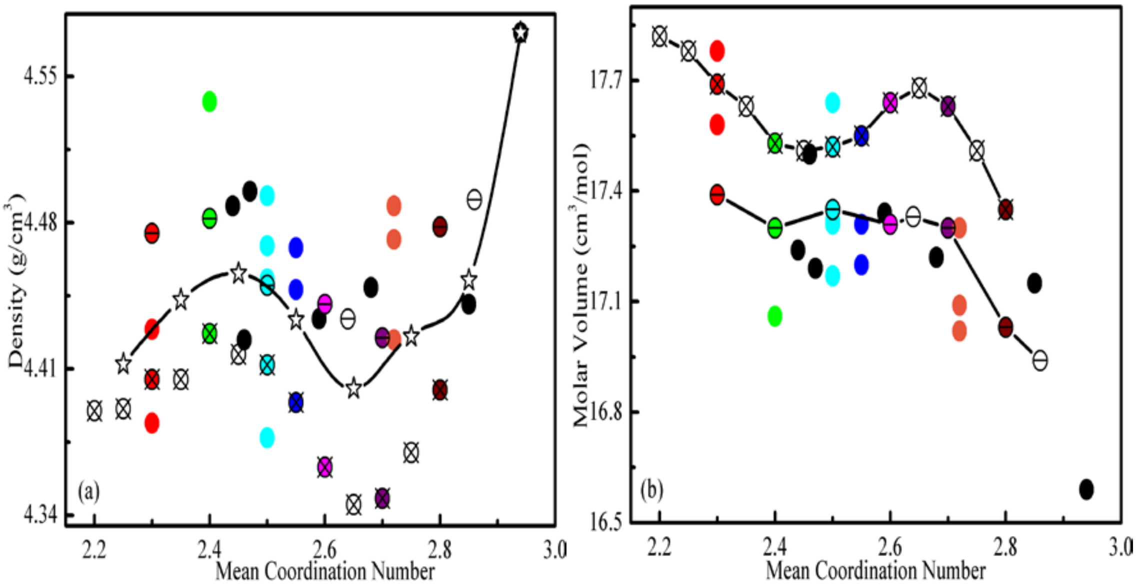

Figure 5.2. Density (a) and molar volume (b) of $Ge_xAs_ySe_{100-x-y}$ glasses as a function of mean coordination number. The red, green, cyan, blue, magenta, violet, orange and wine dots correspond to <*r*> = 2.30, 2.40, 2.50, 2.55, 2.60, 2.70, 2.72 and 2.80, respectively. Black dots correspond to random compositions. Open dots with crosses and with horizontal lines correspond to $Ge_xAs_{10}Se_{90-x}$ and $Ge_xAs_{20}Se_{80-x}$ system respectively. Open stars correspond to average density for all the glasses over an <*r*> space of 0.1. The solid lines are a guide for the eyes.

The variation of the elastic modulus of $Ge_xAs_ySe_{100-x-y}$ glasses as a function of mean coordination number is shown in Figure 5.3. The Young's modulus (*E*) are always higher than the shear modulus (*G*) and bulk modulus (*K*). The data seem scattered at first glance, the fitting results however suggest the existence of two transition thresholds, which may result from the structural changes in glassy networks [191].

This behavior can be more clearly observed for $Ge_xAs_{10}Se_{90-x}$ and $Ge_xAs_{20}Se_{80-x}$ glasses in particular. Figure 5.4. shows that all three elastic constants increase with increasing<*r*> until <*r*> = 2.50 - 2.55 in both two systems, and then remain fairly constant before further increasing at <*r*> = 2.65. As a consequence, two thresholds can be identified simultaneously in these ternary compositions. It is noteworthy that the elastic moduli are almost the same for glasses with the same <*r*>, though the concentration of arsenic doubles. The <*r*> dependence of Poisson's ratio (*v*) shows an overall downward trend, as shown in Figure 5.5. The values of v change between 0.21 and 0.32, which indicates that these glasses are compressible.

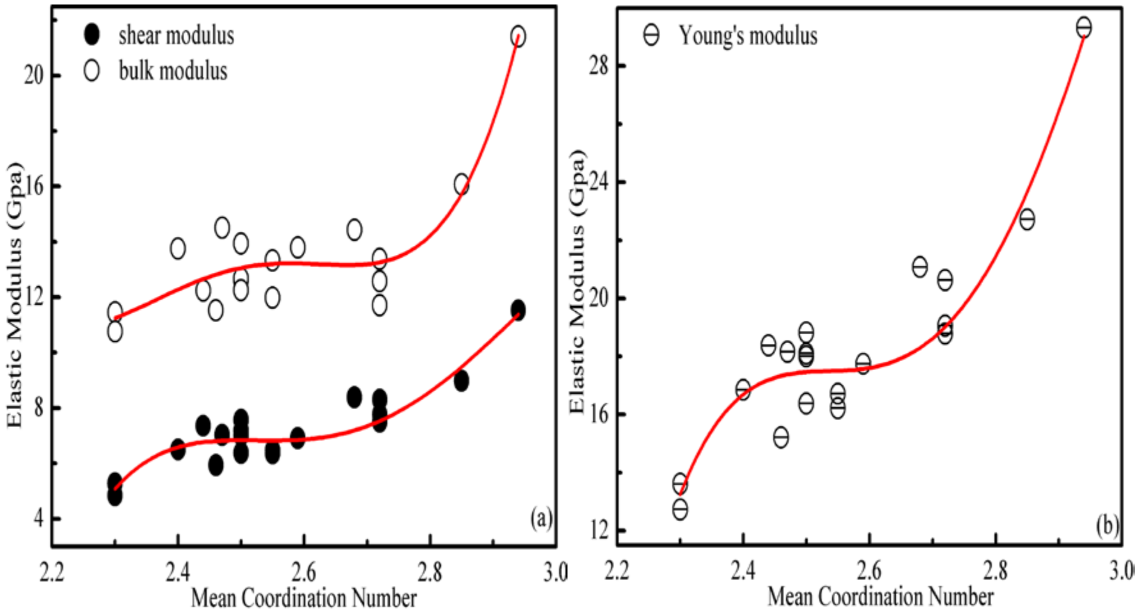

Figure 5.3. The shear modulus, Young’s modulus and bulk modulus of $Ge_xAs_ySe_{100-x-y}$ glasses. The solid lines correspond to polynomial least-squares fitting results.

Table 5.1. Compositions and respective mean coordination number (<*r*>), density (ρ), elastic moduli and molar volume (V_m) of $Ge_xAs_ySe_{100-x-y}$ glasses.

Compositions Ge-As-Se (at%)	<*r*>	Se-rich/-poor (at%)	ρ (g/cm^3)	*G* (GPa)	*E* (GPa)	*K* (GPa)	ν	V_m (cm^3/mol)
11-22-67	2.44	+12	4.488	7.35	18.38	12.24	0.25	17.24
17.5-11-71.5	2.46	+20	4.424	5.94	15.21	11.54	0.28	17.50
11.5-24-64.5	2.47	+5.5	4.495	7.03	18.16	14.51	0.29	17.19
18-23-59	2.59	-11.5	4.434	6.90	17.75	13.79	0.29	17.34
22-24-54	2.68	-26	4.449	8.39	21.08	14.43	0.26	17.22
35-15-50	2.85	-42.5	4.441	8.98	22.72	16.08	0.27	17.15
39-16-45	2.94	-57	4.571	11.52	29.32	21.41	0.27	16.59
5-20-75	2.30	+35	4.475	5.60	14.52	11.94	0.30	17.39
7.5-15-77.5	2.30	+40	4.429	5.28	13.61	10.76	0.29	17.58
10-10-80	2.30	+45	4.405	5.23	13.63	11.50	0.30	17.69
12.5-5-82.5	2.30	+50	4.384	4.84	12.73	11.45	0.32	17.78
5-30-65	2.40	+10	4.538	6.50	16.85	13.76	0.30	17.06
10-20-70	2.40	+20	4.482	6.18	16.01	13.00	0.30	17.30
15-10-75	2.40	+30	4.427	5.92	15.30	12.27	0.29	17.53
7.5-35-57.5	2.50	-10	4.450	7.57	18.82	12.25	0.24	17.31
10-30-60	2.50	-5	4.469	7.18	18.10	12.61	0.26	17.26
12.5-25-62.5	2.50	0	4.493	7.01	18.00	13.93	0.29	17.17
15-20-65	2.50	+5	4.450	7.08	18.24	14.07	0.28	17.35
20-10-70	2.50	+15	4.412	6.68	17.17	13.31	0.29	17.52
22.5-5-72.5	2.50	+20	4.384	6.38	16.38	12.68	0.29	17.64
10-35-55	2.55	-17.5	4.471	6.36	16.22	11.98	0.27	17.20
15-25-60	2.55	-7.5	4.448	6.47	16.71	13.34	0.29	17.31
22.5-10-67.5	2.55	+7.5	4.394	6.93	17.72	13.26	0.28	17.55
20-20-60	2.60	-10	4.441	6.97	17.88	13.67	0.28	17.31
25-10-65	2.60	0	4.363	7.09	18.09	13.49	0.28	17.64
30-10-60	2.70	-15	4.348	7.24	18.42	13.50	0.27	17.63
25-20-55	2.70	-25	4.425	7.35	18.69	13.61	0.27	17.30
18-36-46	2.72	-44	4.488	7.76	19.06	11.70	0.23	17.02
21-30-49	2.72	-38	4.472	7.51	18.79	12.58	0.25	17.09
27-18-55	2.72	-26	4.424	8.30	20.64	13.38	0.24	17.30
30-20-50	2.80	-40	4.478	8.70	21.99	15.51	0.26	17.03
35-10-55	2.80	-30	4.400	9.35	22.69	13.19	0.21	17.35
5-10-85	2.20	+60	4.390	4.72	12.38	10.95	0.31	17.82
7.5-10-82.5	2.25	+52.5	4.391	4.92	12.90	11.29	0.31	17.78
12.5-10-77.5	2.35	+37.5	4.410	5.54	14.38	11.87	0.30	17.63
17.5-10-72.5	2.45	+22.5	4.422	6.61	16.76	12.06	0.27	17.51
27.5-10-62.5	2.65	-7.5	4.345	6.87	17.56	13.24	0.28	17.68
32.5-10-57.5	2.75	-22.5	4.370	7.65	19.47	14.29	0.27	17.51
22-20-58	2.64	-16	4.430	6.91	17.71	13.37	0.28	17.33
33-20-47	2.86	-49	4.491	9.35	23.74	17.17	0.27	16.94

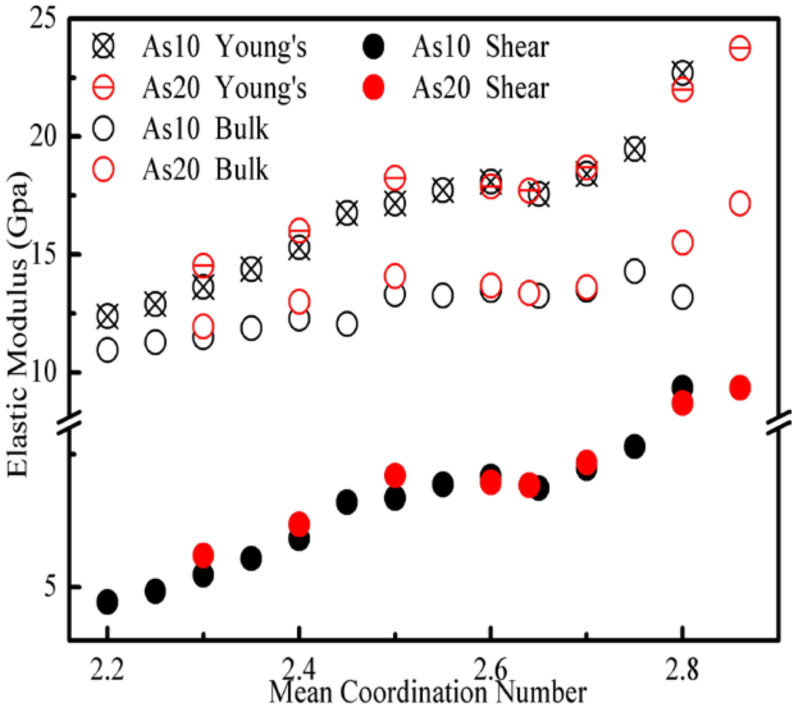

Figure 5.4. The shear modulus, Young's modulus and bulk modulus of $Ge_xAs_{10}Se_{90-x}$ and $Ge_xAs_{20}Se_{80-x}$ glasses.

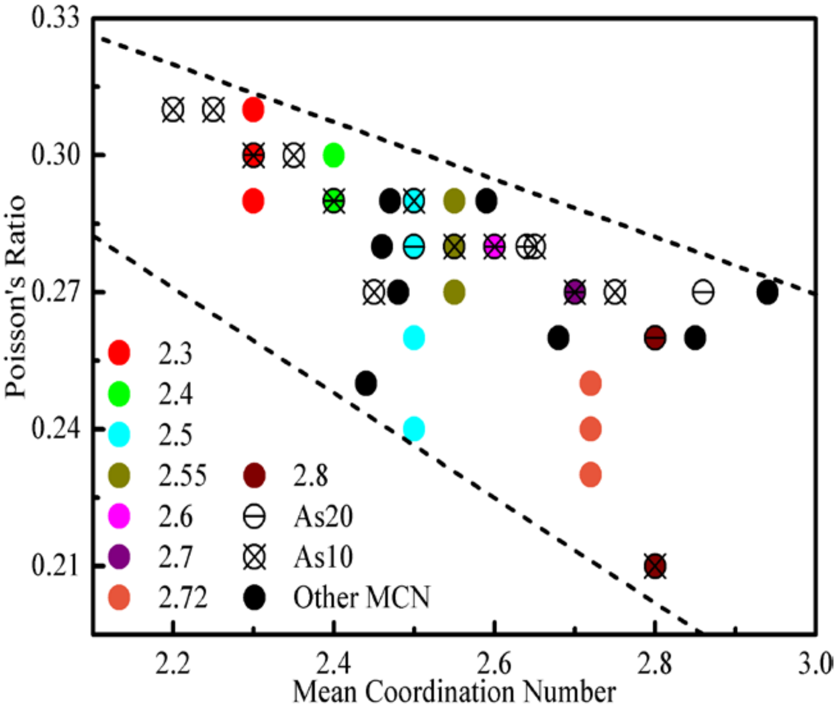

Figure 5.5. Poisson's ratio of $Ge_xAs_ySe_{100-x-y}$ glasses as a function of mean coordination number. Dashed lines are guides to the eyes.

5.4 Discussion

Density is an important parameter containing atomic packing information of materials. For the $Ge_xAs_{10}Se_{90-x}$ and $Ge_xAs_{20}Se_{80-x}$ glass system, if the arrangement of atoms is the same or quite similar, progressively replacing Se (78.96 g/mol) by Ge (72.64 g/mol) should lead to a monotonic decrease of molar mass with $<r>$. From this respect, the increase of density with $<r>$ below 2.40 and above 2.70 implies a significant change in the topological structure of the glasses. Amorphous selenium where $<r> = 2$ consists of disordered chains and rings [14]. Weak Van der Waals forces act between the chains and, therefore, the packing of the structural units is extremely loose. With the addition of 4-fold coordinated Ge and 3-fold coordinated As, the effect of covalent bonding starts to become pronounced. The formation of $GeSe_{4/2}$ tetrahedral and $AsSe_{3/2}$ pyramidal structural units will result in closer packing and a decrease in the molar volume. The local extrema at $<r> = 2.40$ as shown in Figure 5.2(a) and (b) confirms the presence of a topological transition, as expected from rigidity percolation theory. At this point, the optimized mechanical stability of the network where the network is isostatic and ideally constrained connected with tighter bonding and shorter bond lengths, results in the smallest molar volume and a maximum in density. Ge-As-Se glasses with $<r>$ between 2.40 and 2.67 are normally believed to have two-dimensional layered structural segments [58]. In this region, when more Ge and As atoms are incorporated into the layers, the formation of rigid structural units are subject to certain specific angles. This steric constraint could lead to the expansion of the layered structure, so that the density gradually decreases whereas the molar volume increases with further increasing $<r>$. At

$<r> \approx 2.67$, another topological threshold occurs where two-dimensional networks become stable in three-dimensional space [58]. After that, highly cross-linked structural units yield a close packed network, which is responsible for the significant rise and fall in density and molar volume respectively.

The elastic properties are often a macroscopic reflection of interatomic bonding and connectivity of glass materials. For example, Young's modulus, which is defined as the ratio of the stress to the strain, can be used to measure the stiffness of compositions. The shear modulus is more likely to be affected by the bonding energy between atoms. It is expected that the bulk modulus increase monotonically with the network dimensionality. For Ge-As-Se glasses with low $<r>$, the networks are composed of large floppy domains containing flexible one-dimensional structural units. When applying a stress, the chain-like structures in the soft glass matrix are easily deformed at the cost of almost no energy. This is reflected in their low values of bulk modulus. As $<r>$ increases, the isolated rigid units are gradually interconnected and the network connectivity improves. When two-dimensional layered structures have formed, a further increase in the Ge and As concentration first modifies the individual segments within the layers. The dimensionality of the network, however, remains substantially unchanged. Physical properties of these low-dimensional glasses would be mainly affected by weak inter-molecular forces, *e.g.*, van der Waals forces between layers. This explains why the elastic modulus remains nearly constant between $<r> = 2.50 - 2.55$ and $<r> = 2.65$. Eventually, the transition from a two-dimensional to three-dimensional network is complete at $<r> \approx 2.70$, after which fully cross-linked nature of the structure makes it harder to displace the atoms so that the resistance to an applied stress is considerably enhanced. Unlike earlier results [52,212], the elastic constants below $<r> = 2.40$ decrease steadily with decreasing $<r>$ in the present work. The differences could be caused by the presence of 6% - 8% oxygen impurity in previous reported glass samples and the complete neglect of van der Waals interactions and dihedral angle forces in the initial theoretical calculation.

The Poisson's ratio (v) is the negative ratio of transverse contraction strain to longitudinal extension strain in the direction of the applied force. It reflects the resistance to which a material opposes volume change when subjected to a shape change. It has been found that Poisson's ratio correlates well with the glass network connectivity and that the values of v decrease monotonically with an increase in the network cross linking [84]. Although the data of v in Figure 5.5 spread over a relatively large range, it is worth mentioning that glasses having the predominant chain-like features exhibit values higher than 0.3, whereas the highly cross-linked structures correspond to a smaller Poisson's ratio ($v < 0.25$). There seems to be an indication of changes in the way of connecting structural units when $<r>$ passes 2.80. The formation of large number of homopolar bonds somehow softens the 3D compact network, leading to a small increase in v.

For a network with purely covalent bonding, the rigidity percolation is expected to occur at $<r> = 2.40$. However, the behavior of the elastic modulus of Ge-As-Se glasses show some discrepancy between experimental results and the theoretic values as observed in Figure 5.4. The deviation from rigidity percolation theory may be due to the contribution from edge-sharing structural units in the glassy network. In **Section 3.3.1**, Raman spectra results confirm that edge-sharing tetrahedral $GeSe_{4/2}$ units exist in Se-rich glasses. The number of angular constraints of these clusters is smaller than those for corner-sharing structural units [226], which gives rise to soft elastic properties still remaining beyond $<r>$ = 2.40 which postpones the onset of rigidity in the glasses.

5.5 Conclusions

The density and elastic properties of bulk $Ge_xAs_ySe_{100-x-y}$ glasses covering mean coordination number from 2.20 to 2.94 have been investigated. The large glass-forming region of the ternary Ge-As-Se system makes it possible to distinguish the topological threshold from chemical threshold. No significant evidence of the chemical threshold is found in the studied Ge-As-Se glass system consisting of elements with similar atomic mass and radius. The density shows, on average, a maximum at $<r>$ = 2.40 and a minimum at $<r> \approx 2.65$, which underlines the topological effect. The changes in the slope of the dependence of density on $<r>$ correlate with floppy-to-rigid transition and two dimensional-to-three dimensional phase transition respectively. Two elastic transition thresholds are observed simultaneously. The measurements of the elastic moduli support the existence of edge-sharing $GeSe_{4/2}$ structural units in Se-rich glasses through observing a slightly upshift in the position of the rigidity transition threshold. It is obvious that, mean coordination number is capable of determining some physical properties of ternary Ge-As-Se chalcogenide glass system including density, molar volume and elastic constants, however, chemical compositions still can further affect the topological order to some extent.

Chapter 6

Optical Properties of Ge-As-Se Glasses

6.1 Introduction

Over the past decade, chalcogenide glasses have been quite widely used as platform for ultra-fast all-optical processing due to their high linear refractive indices (2.0 - 3.0 at 1.55 μm), high third order nonlinear refractive index, n_2 ($\approx$ 100 - 1000× silica) and femtosecond response time [13,227-230]. Furthermore, in many chalcogenide glasses two photon absorption (TPA) at telecommunications wavelengths is negligible and no free carrier effects are present. These characteristics provide a distinct advantage for third order nonlinear optics compared with materials such as crystalline silicon and III-V semiconductors [231-233] where two photon absorption and free carrier effects can markedly degrade the nonlinear optical response. For example, one of the best-known chalcogenide glasses, As_2S_3, has been successfully utilized in the form of fibres or waveguides for all-optical signal processing [7,111,234-238] However, As_2S_3 has the disadvantages of having only a moderate nonlinearity ($\approx$ 90× fused silica) [19] and also suffering from residual photosensitivity even at infrared (IR) wavelengths [239]. As a result, better chalcogenide glasses are needed which are more nonlinear and display no IR photosensitivity. It has been found that substituting more polarizable Se atoms for S will increase the nonlinear refractive index [227-230]. However, this can come at the expense of a reduced glass transition temperature, increasing two photon absorption and large photosensitivity. While glass compositions with low photosensitivity can be obtained in the ternary Ge-As-Se system [20,170,183], whether such photostable glasses exist in other glass systems remains an open question.

Several empirical or semi-empirical models have been proposed to predict the nonlinear optical properties of materials. Miller's rule is the earliest attempt to predict the second order nonlinear optical behavior of materials, which states as: $\chi^{(2)}(\omega_1, \omega_2, \omega_3) = \Delta \chi^{(1)}(\omega_1)\, \chi^{(1)}(\omega_2)\, \chi^{(1)}(\omega_3)$ [94], where Δ is a constant and $\chi^{(1)}$ is the linear susceptibility. Later, a generalized Miller's rule was suggested to estimate third order nonlinear optical coefficient, however, this relation is not universal and is only applicable for certain optical materials like ionic crystals [240]. Soon afterwards Wang proposed a different equation to describe the link between the linear and the third-order nonlinear optical susceptibilities $\chi^{(3)}$, where the estimations are accurate both for gases at low pressures and for ionic crystals [241]. On the basis of Wang's expression, another simple empirical relationship suggests that the nonlinear refractive index n_2 can be obtained from the linear refractive index n_0 and Abbé number v_d ($v_d = (n_d - 1) / (n_f - n_c)$, where n_d, n_f and n_c are the refractive index at 587.56 nm, 486.13 nm and 656.27 nm, respectively) [242]. It has also been found that nonlinear optical properties can be related to some structure parameters, such as anion valency (Z_a), the coordination number of the nearest-neighbor cation (N_c) as well as optical bandgap (E_g^{opt}) in the material [243,244].

Many different experimental techniques, such as degenerate four-wave mixing (DFWM) [245], the Z-scan technique [13], Mach-Zehnder interferometry (MZI) [246], and third-harmonic generation (THG) [247], have all been applied to determine the linear and nonlinear optical properties of chalcogenide glasses at various wavelengths. DFWM is especially applicable for thin films owing to its high sensitivity and relatively large resonant enhancement. However, DFWM signals may contain a mixture of different mechanisms such as electronic, orientational and thermal effects. This differs from THG where the sensitivity of the experiments is relatively low, but only electronic nonlinearity can be obtained [248]. As for Mach-Zehnder interferometry, it can provide information on the time response of optical nonlinearity but requires precise alignment of the beams to obtain good quality fringes [249].

The Z-scan measurement technique was developed by Shiek-Bahae *et al.* in 1990 [250]. It is a single-beam method capable of measuring both the nonlinear refractive index and nonlinear absorption coefficient simultaneously. During the experiment (Figure 6.1), the sample is moved along the propagation path of a focused Gaussian beam and the transmittance of the sample is measured as a function of its position (z) with a finite aperture (closed aperture) placed in the far field. In this case, the measured transmittance is sensitive to both nonlinear refraction and nonlinear absorption. The refractive part of the nonlinearity slightly modifies the phase front of the propagating wave so that the focus shifts towards or away from the aperture (depending on the sign of the nonlinearity) as the sample is translated and this changes the aperture transmission. If the measurement is conducted without an aperture, which is also known as open aperture measurement, the effect of nonlinear refraction is eliminated and the transmittance curve characterizes the nonlinear absorption of the sample. A reference detector is used to eliminate the possible noise due to laser power fluctuations during the scan. After analyzing “closed aperture” and “open aperture” curves, the nonlinear refractive index (n_2) and nonlinear absorption coefficient (β) can be determined separately.

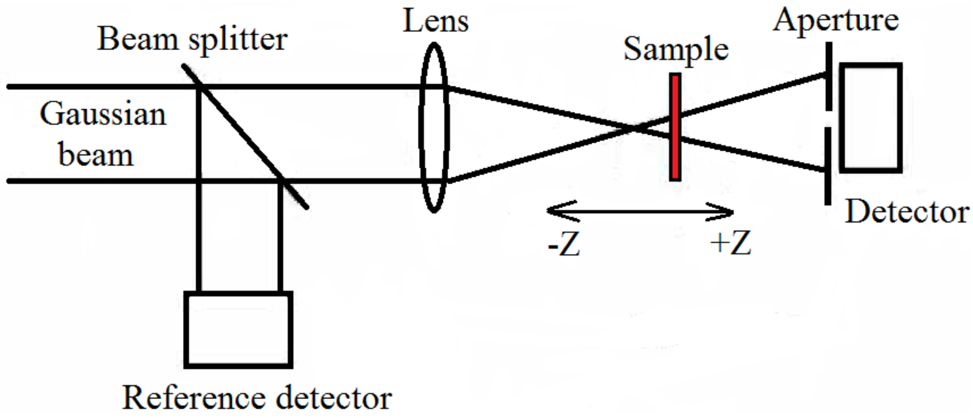

Figure 6.1. Schematic of Z-scan setup

The results of nonlinear measurements for certain chalcogenide glasses are summarized in Table 6.1. Unfortunately, the values of nonlinearity reported by these disparate methods are not always comparable especially once experimental uncertainties are included. Even when the same experimental method is used in different laboratories, reported values of the nonlinearity are inconsistent most likely, for example, because of uncertainties in estimates of the laser intensity [12,19] as well as extrinsic problems of glasses including structural inhomogeneities and non-parallel sample surfaces. Thus, it is not always possible to discern accurate trends from the published data. In this study, systematic measurements of the optical nonlinearity of a wide range of chalcogenide glasses using the Z-scan technique at telecommunications wavelengths were undertaken. Whilst a wide range of $Ge_xAs_ySe_{100-x-y}$ glasses were included, glasses from the

Table 6.1. Nonlinear properties of chalcogenide glasses

Compositions	Wavelength (nm)	n_2 (10^{-14} cm^2/W)	β (10^{-9} cm/W)	Method	Ref
As_2S_3	1064	2.5	2	Z-scan	[228]
	1550	0.4	0.03	Z-scan	[251]
	1064	5.0	0.08	MZI	[246]
	1064	4.3 ± 1.1	0.2 ± 0.05	MZI	[252]
	1250	6.5	0.16	SRTBC	[230]
	1550	5.5	<0.03	SRTBC	[230]
As_2Se_3	1250	30	2.8	SRTBC	[230]
	1550	23	0.14	SRTBC	[230]
	1064	18	4.5	Z-scan	[229]
	1430	10	0.01	Z-scan	[229]
	1500	12.5		Z-scan	[253]
	1064	14 ± 3.5	4.4 ± 1.1	MZI	[252]
Ge-As-Se	1064	12 - 24	1.5 - 5.9	Z-scan	[229]
	1430	8.5	0.01	Z-scan	[229]
	1064	10.2	10	Z-scan	[228]
	1250	13.25 - 30	0.14 - 7.4	SRTBC	[230]
	1550	11.25 - 15.5	0.03 - 0.24	SRTBC	[230]
	1540	6 - 24.6	0.4 - 0.5	Z-scan	[12]
Ge-As-S-Se	1250	4.75 - 15.25	0.04 - 0.24	SRTBC	[230]
	1550	3.25 - 9.75	<0.01 - 0.06	SRTBC	[230]
	1550	0.35	0.025	Z-scan	[252]
Ge-Sb-Se	1064	7.2 ± 0.3 - 15 ± 5	1.6±0.2 - 4.9±0.6	Z-scan	[13]
	1550	5.3 - 19	0.048 - 0.41	Z-scan	[254]
	1500	9		Z-scan	[253]
	1500	4.29 - 6.22	0.0314 - 0.0478	Z-scan	[255]
	1064	7.0±1.2 - 21.2±4.6	<0.7 - 21.4 ± 4.1	Z-scan	[172]
	1550	6.5±2.0 - 20.3±3.0	0.29 - 1.01	DTA	[172]

$Ge_xSb_ySe_{100-x-y}$ system, some binary glasses (As_2S_3 and As_2Se_3) and glasses in which the chalcogen was progressively changed from Se to S ($Ge_{11.5}As_{24}S_xSe_{64.5-x}$) were also added. By recording the data using a single experimental procedure and normalizing to a relatively well-established standard (As_2S_3), the relative nonlinearities of different glass compositions could be determined accurately which is particularly useful to discover trends that identify the best materials for nonlinear photonics.

This chapter, therefore, reports measurements of the nonlinearities of a large number of chalcogenide glasses using the Z-scan method at 1550 nm along with their linear indices. The spectral dispersion of the nonlinearities of five specific chalcogenide compositions (As_2S_3, $Ge_{11.5}As_{24}Se_{64.5}$, $Ge_{15}Sb_{10}Se_{75}$, $Ge_{15}Sb_{15}Se_{70}$ and $Ge_{12.5}Sb_{20}Se_{67.5}$) in the range of $<r> = 2.40 - 2.50$ was also investigated for wavelength between 1150 nm and 1686 nm. The results were used to quantify trends in the value of nonlinearity as the composition of the glass was changed and the measured dispersion was compared with the predictions of two widely discussed models for scaling of the nonlinearity of direct and indirect semiconductors introduced by Sheik-Bahae [256] and Dinu [257] respectively. The results provide direct insight into optimizing chalcogenide glass for third order nonlinear photonics and indicate that there is a upper bound on the value of nonlinearity before two photon absorption starts to dominate degrading the nonlinear response.

6.2 Experiments

Firstly the linear refractive indices (n_0) at 1550 nm were measured using a Metricon 2010 Prism Coupler to an accuracy of ± 0.001. As shown in Figure 6.2, in this method, the sample contacts with the base of a prism by pressure applied through a pneumatically-operated coupling head. When the sample and prism are rotated with respect to the static laser beam, light strikes the prism and will be usually totally reflected onto the photo-detector until the angle of incidence becomes less than the critical angle (θ_c), at which point the intensity of light reaching the detector drops abruptly. Since the index of the prism is known, the index of bulk glass can be then determined by the equation:

$$\theta_c = \arcsin(n / n_p) \tag{6.1}$$

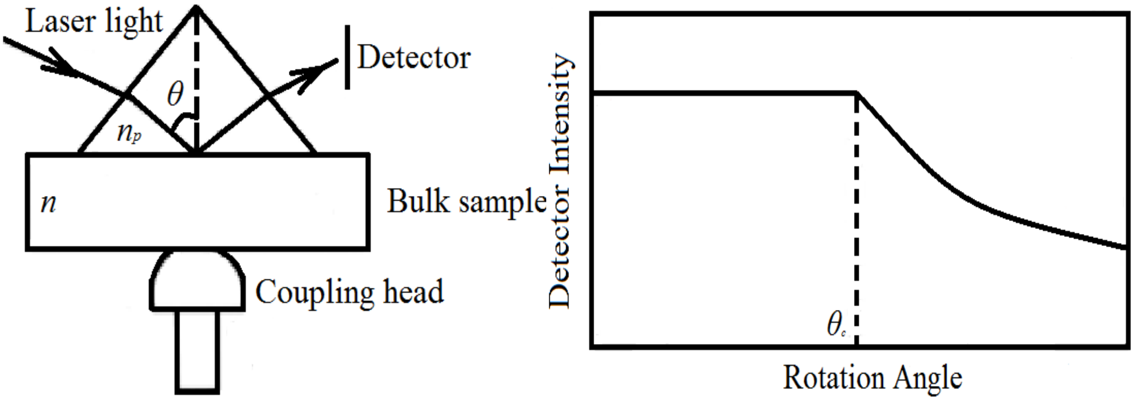

Figure 6.2. Schematic of prism coupler measurement for bulk material.

The transmission and absorption spectra were recorded using a dual beam Varian Cary 5000 UV-Vis-NIR spectrophotometer in the wavelength range from 500 to 2500 nm. Thickness of the bulk samples was around 2 mm. To measure the optical bandgap (E_g^{opt}), it is necessary to use relatively thin glass samples otherwise the Urbach tail [88] dominates the transmission measurements. A hot-pressing technique was, therefore, employed to produce thin samples from bulk glasses since polishing was impractical and films deposited by physical vapour deposition often have quite different properties (and composition) from the bulk. For hot-pressing a small amount (milligram) of bulk glass was first heated in an inert nitrogen atmosphere to a set point above the glass transition temperature. After the glass became sufficiently soft, it was pressed between polished sapphire windows using weights to control the thickness of the resulting sample. Once a uniform layer had formed, the sample was slowly cooled to ambient temperature to avoid cracking. The amorphous nature of each film was checked using X-ray diffraction (XRD) and no sharp peaks were observed for any composition. The absorption spectra of these layers, which were typically 10 - 20 μm thick, were measured at room temperature. From these data the optical bandgap of the material was extracted using a Tauc plot [87].

The nonlinearities were measured using 1 - 2 mm thick samples via the z-scan technique. The source used for these measurements consisted of ≈ 260 fs pulses at 1550 nm generated by a Quantronix Palitra OPA pumped with a Ti: sapphire laser (Clark-MXR CPA 2001) at a repetition of 1 kHz. The beam from the Palitra was truncated using an aperture to improve its spatial coherence and then focused onto the sample using a 125 mm focal length lens. The beam transmitted through the sample was intercepted in the far field by a rotating scattering screen (to reduce the speckle) and the light distribution on the screen was imaged onto a Xenics InGaAs camera. Around 300 frames were averaged and then stored for different positions of the sample as it was translated through the focus. These stored images could be reconstructed to create a “movie” of the z-scan signal and then post-processed to extract the open and closed aperture signals in National Instruments (NI) LabVIEW software. Errors resulting from non-parallel sample surfaces could be avoided by tracking the beam center throughout the scan. To further improve the accuracy of z-scan method, which can suffer from errors due to uncertainties in the beam profile or pulse shape, measurements were calibrated using an

As_2S_3 bulk glass sample as a reference since its nonlinearity is known accurately at 1550 nm from a wide range of experiments and has a value n_2 of (2.9 ± 0.3) × 10^{-14} cm^2/W [238]. For each sample, a series of open and closed aperture z-scan measurements were recorded for different incident intensities with the traces normalized against a “zero” power trace which contained distortions introduced by the sample. After division of the closed aperture by the open aperture traces, the nonlinear refractive index (n_2) in the absence of nonlinear absorption was evaluated by:

$$n_2 = \frac{\Delta\phi_0 \lambda}{2\pi I_0 L_{eff}} \tag{6.2}$$

where $\Delta\phi_0$ is the on-axis phase shift at the focus ($z = 0$), λ is the laser wavelength, $L_{eff} = (1 - e^{-\alpha L}) / \alpha$, L is the sample length, α is the linear absorption coefficient, and I_0 is the peak on-axis intensity at the focus. As nonlinear phase shift is proportional to the change in transmittance between the peak and valley in a closed aperture z-scan curve ($\Delta T_{pv} = T_p - T_v$), the amplitude of the phase shift can be approximated by a simplified I - ΔT_{pv} curve including reflection loss $R_l = (n_0 - 1)^2 / (n_0 + 1)^2$ as a correction factor. The slope of the curve against that of curve for As_2S_3 was then used to obtain the nonlinear refractive index of measured sample.

When an incident beam propagates through the sample exhibiting two-photon absorption, the change in intensity can be written as:

$$\frac{dI}{dz} = -\alpha I - \beta I^2 \tag{6.3}$$

where α and β are the one and two photon absorption coefficients respectively. The solution to Equation (6.3) is given by:

$$\frac{1}{T} = \exp(\alpha L) + \beta L I_0 \exp(\alpha L) \tag{6.4}$$

where T is the transmittance of the sample. The linear dependence between $1/T$ and I_0 is generally indicative of TPA. Then, the nonlinear absorption coefficient (β) can be deduced from fitting open aperture trace to the equation:

$$\beta \approx -\frac{2\sqrt{2}\Delta T\left(z\right)(1+Z^2/Z_0^2)}{I_0 L_{eff}} \tag{6.5}$$

where $\Delta T_{(z)}$ is the normalized change in transmittance, and Z_0 is the diffraction length of the focused beam. The corresponding figures of merit (FOM) for certain compositions were calculated using Equation (2.17) described in **Section 2.3.3**.

6.3 Results

Figures 6.3(a) and (b) show the transmission curve as a function of wavelength for some $Ge_xAs_{10}Se_{90-x}$ and $Ge_xAs_{20}Se_{80-x}$ samples, respectively. All glasses showed good transparency (60% - 70% transmission) in the near infrared region (1000 - 2500 nm) and no absorption bands were observed in this range. It is clear that for the set of $Ge_xAs_{10}Se_{90-x}$, the transmission edges shift towards shorter wavelength as the concentration of Ge increases, indicating a monotonic increase of optical bandgap. The transmission curves of $Ge_xAs_{20}Se_{80-x}$, on the other hand, show different behavior with increasing Ge content. The cut-on wavelengths display a blueshift as the Ge content reaches 20 at%; then the redshift of transmission curves becomes evident with further increase of Ge content. These features suggest that a threshold corresponding to the maximum bandgap may occur at $Ge_{20}As_{20}Se_{60}$ ($\langle r \rangle = 2.60$) for the $Ge_xAs_{20}Se_{80-x}$ group.

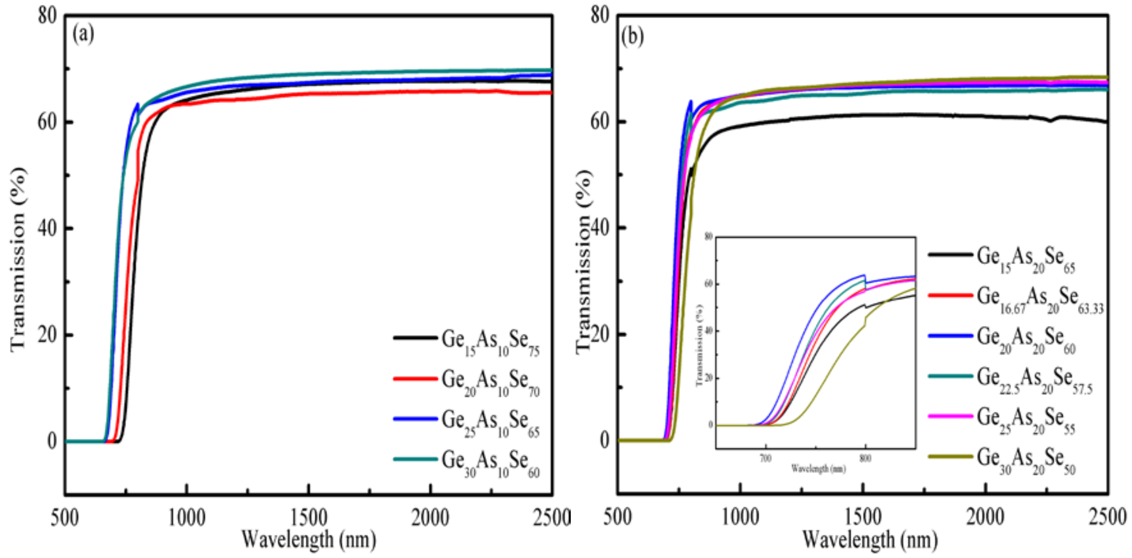

Figure 6.3. Transmission curves as a function of wavelength for (a) $Ge_xAs_{10}Se_{90-x}$ and (b) $Ge_xAs_{20}Se_{80-x}$ glasses. The insert graph shows a close-up view of the data.

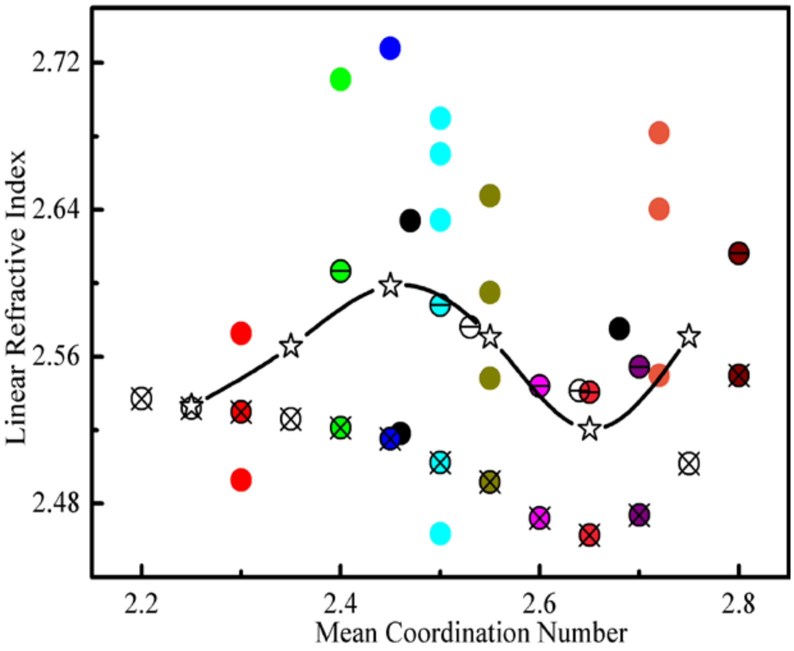

Figure 6.4. Linear refractive index (n_0) of $Ge_xAs_ySe_{100-x-y}$ glasses as a function of mean coordination number at 1550 nm. The red, green, blue, cyan, dark yellow, magenta, pink, violet, orange and wine dots correspond to <*r*> = 2.30, 2.40, 2.45, 2.50, 2.55, 2.60, 2.70, 2.65, 2.70, 2.72 and 2.80, respectively. Black dots correspond to random compositions. Open dots with crosses and with horizontal lines correspond to $Ge_xAs_{10}Se_{90-x}$ and $Ge_xAs_{20}Se_{80-x}$ system respectively. Open stars correspond to average linear refractive index for all the glasses over an <*r*> space of 0.1. The solid line is a guide for the eyes.

Table 6.2. Compositions and respective mean coordination number (<*r*>), linear refractive index (n_0), As/Ge ratio and nonlinear refractive index (n_2) of all glass samples.

Compositions	<*r*>	As/Ge ratio	n_0	n_2 (10^{-14} cm^2/W)
$Ge_{12.5}As_5Se_{82.5}$	2.30	0.40	2.493	
$Ge_{7.5}As_{15}Se_{77.5}$	2.30	2	2.573	
$Ge_5As_{30}Se_{65}$	2.40	6	2.711	
$Ge_{6.25}As_{32.5}Se_{61.25}$	2.45	5.20	2.728	
$Ge_{17.5}As_{11}Se_{77.5}$	2.46	0.63	2.518	
$Ge_{11.5}As_{24}Se_{64.5}$	2.47	2.09	2.634	7.33
$Ge_{22.5}As_{7.5}Se_{72.5}$	2.50	0.22	2.464	
$Ge_{12.5}As_{25}Se_{62.5}$	2.50	2	2.635	
$Ge_{10}As_{30}Se_{60}$	2.50	3	2.670	
$Ge_{7.5}As_{35}Se_{57.5}$	2.50	4.67	2.690	
$Ge_{18.75}As_{17.5}Se_{63.75}$	2.55	0.93	2.548	
$Ge_{15}As_{25}Se_{60}$	2.55	1.67	2.595	
$Ge_{10}As_{35}Se_{55}$	2.55	3.50	2.648	
$Ge_{22}As_{24}Se_{54}$	2.68	1.09	2.575	
$Ge_{27}As_{18}Se_{55}$	2.72	0.67	2.550	
$Ge_{21}As_{30}Se_{49}$	2.72	1.43	2.640	
$Ge_{18}As_{36}Se_{46}$	2.72	2	2.682	
$Ge_5As_{10}Se_{85}$	2.20	2	2.537	7.28
$Ge_{7.5}As_{10}Se_{82.5}$	2.25	1.33	2.532	7.28
$Ge_{10}As_{10}Se_{80}$	2.30	1	2.530	7.24
$Ge_{12.5}As_{10}Se_{77.5}$	2.35	0.80	2.526	7.29
$Ge_{15}As_{10}Se_{75}$	2.40	0.67	2.521	6.62
$Ge_{17.5}As_{10}Se_{72.5}$	2.45	0.57	2.515	6.41
$Ge_{20}As_{10}Se_{70}$	2.50	0.50	2.502	5.08
$Ge_{22.5}As_{10}Se_{67.5}$	2.55	0.44	2.492	5.80
$Ge_{25}As_{10}Se_{65}$	2.60	0.40	2.472	5.42
$Ge_{27.5}As_{10}Se_{62.5}$	2.65	0.36	2.463	5.92
$Ge_{30}As_{10}Se_{60}$	2.70	0.33	2.474	5.12
$Ge_{32.5}As_{10}Se_{57.5}$	2.75	0.31	2.502	6.26
$Ge_{35}As_{10}Se_{55}$	2.80	0.29	2.550	5.90
$Ge_{10}As_{20}Se_{70}$	2.40	2	2.607	8.58
$Ge_{15}As_{20}Se_{65}$	2.50	1.33	2.588	7.48
$Ge_{16.67}As_{20}Se_{63.33}$	2.53	1.20	2.576	6.84
$Ge_{20}As_{20}Se_{60}$	2.60	1	2.544	4.88
$Ge_{22}As_{20}Se_{58}$	2.64	0.91	2.541	5.62
$Ge_{22.5}As_{20}Se_{57.5}$	2.65	0.89	2.541	6.52

$Ge_{25}As_{20}Se_{55}$	2.70	0.80	2.554	6.90
$Ge_{30}As_{20}Se_{50}$	2.80	0.67	2.616	7.31
$Ge_{7.5}Sb_{10}Se_{82.5}$	2.25	-	2.628	10.16
$Ge_{10}Sb_{10}Se_{80}$	2.30	-	2.624	9.03
$Ge_{12.5}Sb_{10}Se_{77.5}$	2.35	-	2.610	8.00
$Ge_{15}Sb_{10}Se_{75}$	2.40	-	2.598	8.16
$Ge_{17.5}Sb_{10}Se_{72.5}$	2.45	-	2.589	9.69
$Ge_{20}Sb_{10}Se_{70}$	2.50	-	2.576	6.65
$Ge_{22.5}Sb_{10}Se_{67.5}$	2.55	-	2.558	5.95
$Ge_{25}Sb_{10}Se_{65}$	2.60	-	2.533	7.17
$Ge_{27.5}Sb_{10}Se_{62.5}$	2.65	-	2.570	6.13
$Ge_{30}Sb_{10}Se_{60}$	2.70	-	2.625	7.05
$Ge_{15}Sb_{15}Se_{70}$	2.45	-	2.690	10.34
$Ge_{17.5}Sb_{15}Se_{67.5}$	2.50	-	2.670	8.00
$Ge_{20}Sb_{15}Se_{65}$	2.55	-	2.647	7.51
$Ge_{20.83}Sb_{15}Se_{64.17}$	2.57	-	2.635	7.12
$Ge_{22.5}Sb_{15}Se_{62.5}$	2.60	-	2.661	7.95
$Ge_{25}Sb_{15}Se_{60}$	2.65	-	2.713	8.92
$Ge_{10}Sb_{20}Se_{70}$	2.40	-	2.821	14.29
$Ge_{12.5}Sb_{20}Se_{67.5}$	2.45	-	2.803	12.70
$Ge_{15}Sb_{20}Se_{65}$	2.50	-	2.778	9.79
$Ge_{16.67}Sb_{20}Se_{63.33}$	2.53	-	2.756	10.73
$Ge_{17.5}Sb_{20}Se_{62.5}$	2.55	-	2.768	10.82
$Ge_{20}Sb_{20}Se_{60}$	2.60	-	2.819	13.42
$Ge_{22.5}Sb_{20}Se_{57.5}$	2.65	-	2.863	14.89
$Ge_{11.5}As_{24}S_{64.5}$	2.47	-	2.265	2.08
$Ge_{11.5}As_{24}S_{48.375}Se_{16.125}$	2.47	-	2.356	2.82
$Ge_{11.5}As_{24}S_{32.25}Se_{32.25}$	2.47	-	2.446	3.73
$Ge_{11.5}As_{24}S_{16.125}Se_{48.375}$	2.47	-	2.539	5.46
As_2S_3	2.40	-	2.430	2.92
As_2Se_3	2.40	-	2.837	12.72

The linear refractive index (n_0) of all the glass samples at 1550 nm and the corresponding mean coordination number <*r*> are shown in Table 6.2. The dependence of n_0 and <*r*> for $Ge_xAs_ySe_{100-x-y}$ glasses are illustrated in Figure 6.4. The trend of this graph is very similar to that of density variation with <*r*> in Figure 5.1. The data exhibit notable scatter but if the linear refractive index of the glasses are averaged over a mean coordination number space of 0.1, a global trend towards a maximum at <*r*> = 2.45 and a minimum at <*r*> = 2.65 is revealed as shown by the solid line. When the concentration of As was fixed, increasing the Ge content led initially to a decrease in n_0, followed by a marked increase when <*r*> exceeds 2.65. Furthermore, it has been found that the n_0 correlates to the As/Ge ratio as shown in Figure 6.5. Roughly speaking, the higher the ratio of As content to Ge content is, the higher the refractive index. These provide direct evidence that mean coordination number plays an important role in determining the refractive index of Ge-As-Se glasses. The results about the correlation between mean coordination number and the refractive index in present $Ge_xSb_ySe_{100-x-y}$ glasses were published elsewhere [223,258].

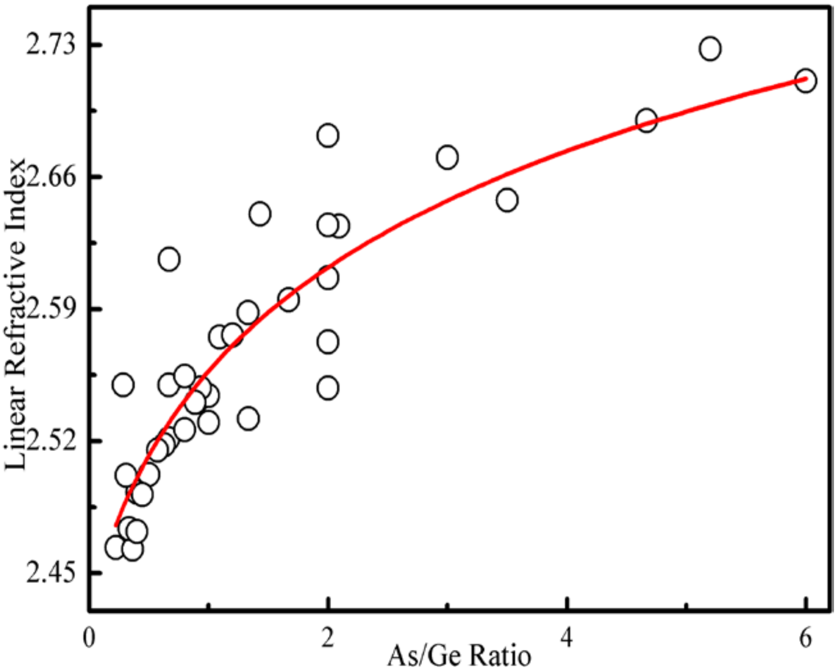

Figure 6.5. Linear refractive index of $Ge_xAs_ySe_{100-x-y}$ glasses as a function of the ratio of As content to Ge content. The solid line is a guide for the eyes.

Figure 6.6 shows typical normalized closed aperture and open aperture transmittance curves for $Ge_{11.5}As_{24}Se_{64.5}$ at 1550 nm for three different intensities, from 0.56 GW/cm^2

to 2.02 GW/cm^2. As the beam intensity increases, the peak transmittance of the closed aperture increases while the valley decreases, indicating an increase in nonlinear phase shift. The open aperture traces show no sign of nonlinear absorption. The nonlinear refraction values of $Ge_xAs_ySe_{100-x-y}$ glasses as well as comparative results on $Ge_xSb_ySe_{100-x-y}$ system, $As_2S(Se)_3$ and $Ge_{11.5}As_{24}S_xSe_{64.5-x}$ at the telecommunication wavelength of 1550 nm are presented in Table 6.2. Nonlinearities around 100 - 800 times those of fused silica can be achieved. On average, the glasses in the Ge-Sb-Se system have higher nonlinearities than those in the Ge-As-Se system for the same As(Sb) concentration. The nonlinearity of Ge-As-S-Se quaternary glasses increases steadily as Se is substituted for S. The nonlinear refractive index of As_2Se_3 is approximately four times as large as that of As_2S_3 glass, which is consistent with previous reports [7]. No significant correlation between n_2 and $<r>$ was found in the Ge-Sb-Se system. However, it is of interest to find that the average values of the nonlinear refractive index for Ge-As-Se glasses appear to have a global minimum around $<r> = 2.65$ (Figure 6.7).

The optical bandgap, E_g^{opt}, is estimated by well-known Tauc relationship, which expressed as Equation (2.11). The variations of $(\alpha h\nu)^{1/2}$ with $h\nu$ depicted in Figure 6.8 show good linearity over a wide range of photon energies, which indicates that studied compositions obey the rule of indirect allowed transition. The optical band gap E_g^{opt} is determined by extrapolating the linear portion of the curve to the horizontal axis which $(\alpha h\nu)^{1/2} = 0$. The estimated values of E_g^{opt} for five selected samples are listed in Table 6.3. It is evident that As_2S_3 glass has the widest optical bandgap, and the smallest value is obtained in $Ge_{12.5}Sb_{20}Se_{67.5}$.

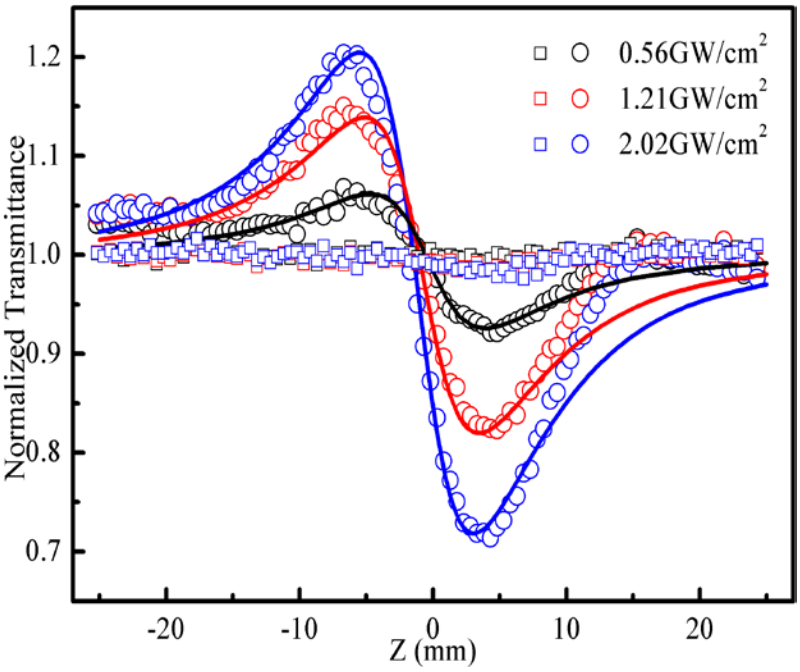

Figure 6.6. Normalized transmittance obtained from closed aperture and open aperture Z-scan measurement for $Ge_{11.5}As_{24}Se_{64.5}$ for different intensities at 1550 nm. The open circles and squares are experimental data and the solid lines are theoretical fitting.

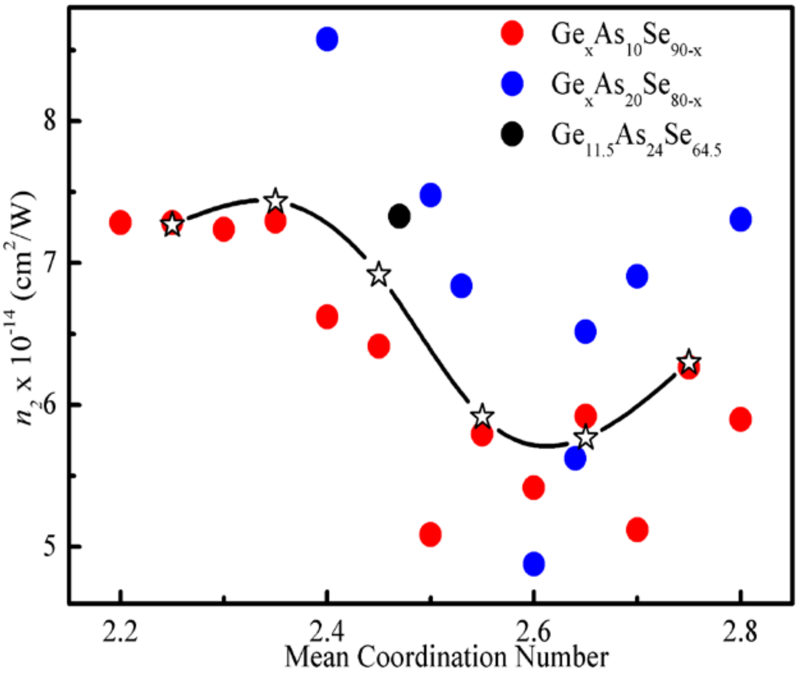

Figure 6.7. Nonlinear refractive index (n_2) as a function of mean coordination number (<*r*>) for $Ge_xAs_ySe_{100-x-y}$ system. Open stars correspond to average values of nonlinear refractive index over an <*r*> space of 0.1. The solid line is a guide for the eyes.

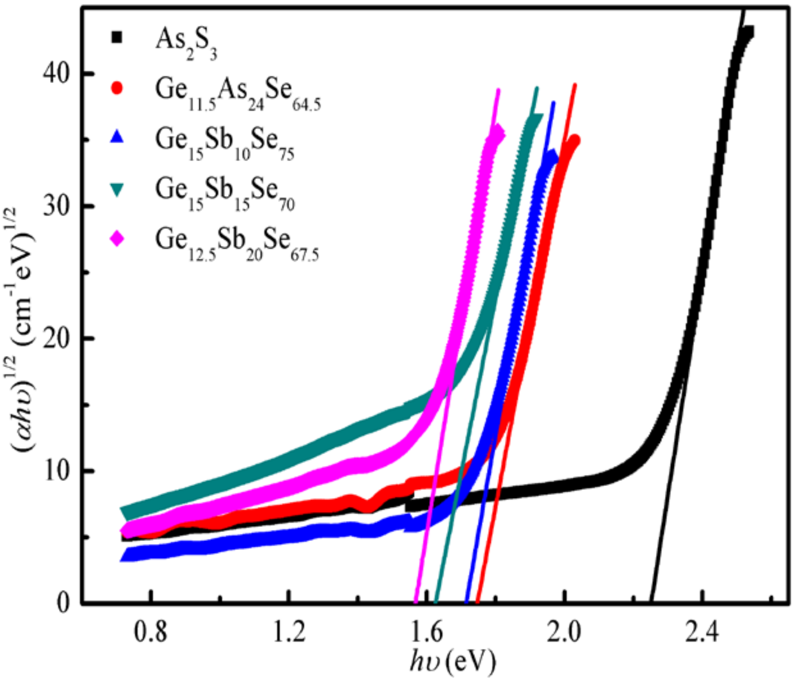

Figure 6.8. Plots of $(\alpha hv)^{1/2}$ versus hv for five films.

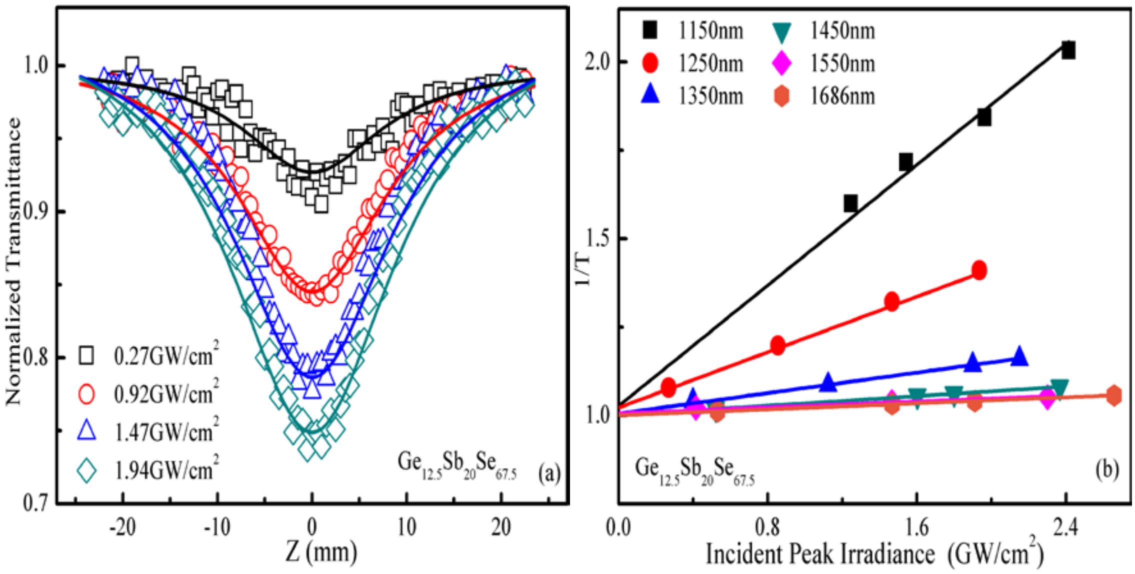

Figure 6.9. (a) Typical open aperture traces and their corresponding fit to a numerical model for $Ge_{12.5}Sb_{20}Se_{67.5}$ for different intensities at a wavelength of 1250 nm. (b) The inverse of transmittance for $Ge_{12.5}Sb_{20}Se_{67.5}$ is plotted against irradiance at different wavelengths. Theoretical fits are shown in solid lines.

Figure 6.9(a) shows a series of normalized open aperture traces for $Ge_{12.5}Sb_{20}Se_{67.5}$ at a wavelength of 1250 nm which exhibits the most distinct nonlinear absorption of the five selected samples. An obvious reduction in transmittance at the focus is noted with increasing of excitation intensity, implying an increase in the nonlinear absorption. In order to obtain reliable nonlinear absorption data, the reciprocal of transmittance $1/T$ (at the focus of open aperture traces) was plotted as a function of the peak on-axis irradiance for this sample for different wavelengths as shown in Figure 6.9(b). The inverse transmittance increases with the incident light intensities. The linear intensity dependent characteristic confirms that two-photon absorption is the dominant nonlinear absorption process at these wavelengths. By applying fitting theory based on Equation (6.5), the nonlinear absorption coefficient, β, could be deduced from these open aperture Z-scan data. Table 6.3 summarizes the wavelength dependent nonlinear optical parameters of the five selected glasses for which bandgap measurements were made from pressed films.

It is evident from Table 6.3 that n_2 and β both decrease with increasing wavelength. The large nonlinear refractive indices in Ge-Sb-Se samples appear at the cost of increasing nonlinear absorption. For As_2S_3 glass, within experiment limitation, no nonlinear absorption was observed at any wavelength. Similarly nonlinear absorption was negligible for $Ge_{11.5}As_{24}Se_{64.5}$ and $Ge_{15}Sb_{10}Se_{75}$ glasses at the telecommunication wavelength around 1550 nm. The figures of merit for As_2S_3, $Ge_{11.5}As_{24}Se_{64.5}$ and $Ge_{15}Sb_{10}Se_{75}$ are much higher than 10 at 1550 nm, indicating that these glasses satisfy the criterion for all-optical devices mentioned in **Section 2.3.3**.

Table 6.3. Compositions, optical bandgap (E_g^{opt}), nonlinear optical properties (n_2, β and FOM) of five selected chalcogenide glasses.

Compositions	E_g^{opt} (eV)	Wavelength (nm)	n_2 (10^{-14} cm^2/W)	β (10^{-9} cm/W)	*FOM*
As_2S_3	2.22	1150	4.33	< 0.01	> 30
		1250	3.67	< 0.01	> 25
		1350	3.50	< 0.01	> 24
		1450	3.23	< 0.01	> 22
		1550	2.85	< 0.01	> 20
		1686	2.79	< 0.01	> 19
$Ge_{11.5}As_{24}Se_{64.5}$	1.75	1150	11.8	1.20	1
		1250	10.4	0.35	2
		1350	8.83	0.11	6
		1450	7.67	< 0.01	> 57
		1550	7.90	< 0.01	> 59
		1686	6.83	0.10	4
$Ge_{15}Sb_{10}Se_{75}$	1.72	1150	12.5	1.27	1
		1250	9.00	0.35	2
		1350	7.67	0.12	5
		1450	8.30	0.05	11
		1550	7.50	< 0.01	> 52
		1686	7.33	< 0.01	> 51
$Ge_{15}Sb_{15}Se_{70}$	1.62	1150	15.5	5.94	0.2
		1250	14.9	2.78	0.4
		1350	13.7	0.81	1
		1450	12.2	0.49	2
		1550	10.0	0.35	2
		1686	10.0	0.27	2
$Ge_{12.5}Sb_{20}Se_{67.5}$	1.57	1150	20.3	7.44	0.2
		1250	17.5	3.05	0.5
		1350	13.5	0.94	1
		1450	12.0	0.45	2
		1550	11.4	0.37	2
		1686	9.40	0.22	3

Typical traces for the frequency dependence of n_2 for these five glasses are shown in Figure 6.10(a), which shows a monotonic increase with normalized photon energy $h\upsilon/E_g^{opt}$. This trend is consistent with previous studies for As-S-Se, Ge-As-S-Se and Ge-Sb-Se glasses [13,230]. Figure 6.10(b) shows that β also increases monotonically with $h\upsilon/E_g^{opt}$ and the threshold for observable two photon absorption is around $h\upsilon/E_g^{opt}$ = 0.5 as expected.

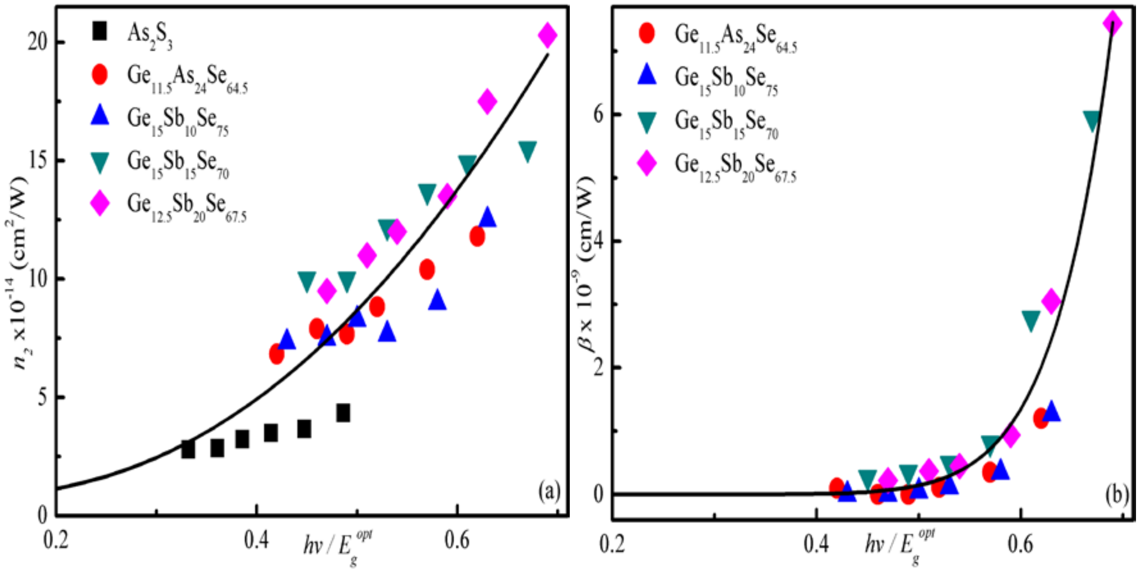

Figure 6.10. Plot of n_2 (a) and β (b) as a function of normalized photon energy for the glasses listed in Table 6.3. The solid lines are a guide for the eyes.

6.4 Discussion

6.4.1 Linear optical properties of Ge-As-Se glasses

Predicting the exact value of the linear refractive index of a glass is complicated. According to the most widely used Lorentz-Lorenz equation, the refractive index n_0 can be described by the following expression [85]:

$$\frac{n_0^2-1}{n_0^2+2}=\frac{R_m}{V_m}=\frac{R_m}{(\frac{M}{\rho})} \tag{6.6}$$

where V_m is the molar volume; M is the mean atomic weight; ρ is the density; R_m is the molar refraction and has a clear connection with polarizability α by introducing the

Avogadro constant N_A as [85]:

$$R_m = \frac{4\pi N_A \alpha}{3} \tag{6.7}$$

At 1550 nm where the refractive index has been measured in this work, the contribution to polarizability is almost entirely from electronic transitions. The magnitude of α generally depends on the number of electrons. Generally speaking, the greater the number of electrons in the molecule, the larger is its electronic polarizability. In addition, the relationship between polarizability and unshared electron pairs cannot be neglected. Lone-pair electrons are easier to distort than those electrons shared in the covalent bonds, causing an increase in polarizability. The molecular shapes also influence polarizability. Elongated chains have electrons that can be easily deformed; therefore they are more polarizable than compact and symmetrical molecules. For the $Ge_xAs_ySe_{100-x-y}$ system, it is normally assumed that every As and Se atom has one and two unshared electron pairs respectively, while Ge atom has none. With the increase of atomic percentage of germanium and arsenic, the number of total electrons and lone-pair electrons will decrease gradually. However, glasses with higher <*r*> tend to form more rigid and tight 3D structure, which would be partially offset the reduction in polarizability. Considering the trend of molar volume with <*r*> discussed in **Chapter** 5 and all factors mentioned above resulting in the variation of molar refraction (or electronic polarizability), it is somewhat natural to understand the changes in n_0 with <*r*> and As/Ge ratio as shown in Figure 6.4 and 6.5 respectively.

6.4.2 Nonlinear optical properties of Ge-As-Se glasses

The lone electron pairs theory has been successfully used to explain the connection between the nonlinear refractive index and the glass structure for binary chalcogenide systems [228]. It has been suggested that for Ge_xSe_{100-x} glasses, the concentration of lone electron pairs and nonlinear refractive index n_2 both decrease with the increase of germanium amount. A large number of lone electron pairs appear to be the key to obtain high nonlinearities in this system. However, no such correlation has been found in this study and in the Ge-Sb-S-Se system bringing such a conclusion into doubt [13]. Thus, the influence of lone electron pairs is inconclusive. Certainly this parameter seems not to be the predominant factor determining nonlinear properties of ternary or multicomponent chalcogenide systems.

As is evident from Table 6.2, glasses with higher linear refractive indices also have the higher nonlinearities. According to the generalized Miller's rule, the third-order susceptibility $\chi^{(3)}$ (esu) is given by [94,240]:

$$\chi^{(3)} = \frac{n_2 n_0^2}{0.0395} = A\left[\chi^{(1)}\right]^4 = A\left[\frac{\left(n_0^2\text{-}1\right)}{4\pi}\right]^4 \tag{6.8}$$

where A is assumed to be a constant. Figure 6.11(a) plots the $\chi^{(3)}$ as a function of $\chi^{(1)}$ and demonstrates that a good linear relation is achieved using a value of 3×10^{-10} for A. This value is consistent with that reported for ionic crystals [241], various oxide glasses, optical crystals [259], and some chalcogenide glasses [244]. Based on the above fitting result, Equation (6.8) can be transformed into:

$$n_2 = \frac{3\times10^{-10}\times0.0395}{(4\pi)^4}\frac{\left(n_0^2-1\right)^4}{n_0^2} = 4.75\times10^{-16}\frac{\left(n_0^2-1\right)^4}{n_0^2}cm^2/W \qquad (6.9)$$

The relationship between the nonlinear refractive index (n_2) and linear refractive index (n_0) of the samples is shown in Figure 6.11(b). It is worth noting that in the measurements, some errors exist because of imperfections in the samples which could account for some of the scatter in the data. Nevertheless, the scatter represents only about ± 10% uncertainty in the experimental values of nonlinear refractive index which is comparable with or smaller than the uncertainties in most experiments especially when comparing data from different laboratories. Thus, it is safe to conclude on the basis of these data that the generalized Miller's rule is a rather effective and, therefore, probably the best predictor of the relative nonlinear coefficients of chalcogenide glasses, at least at wavelengths where linear and nonlinear absorption is small.

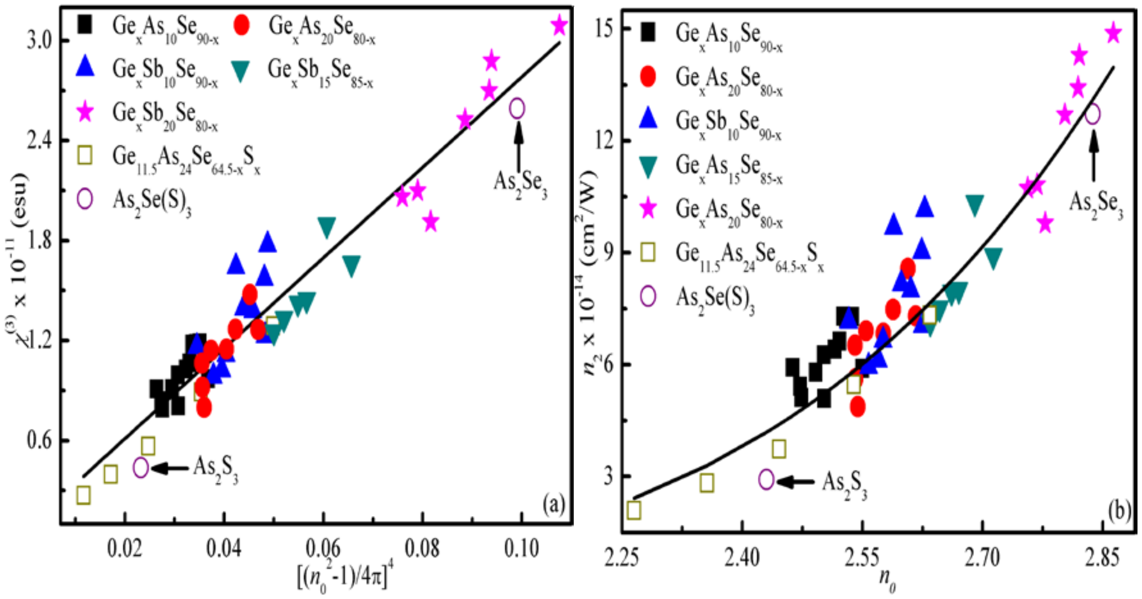

Figure 6.11. (a) The variation of the third order nonlinear susceptibility ($\chi^{(3)}$) as a function of linear susceptibility ($\chi^{(1)}$). Solid line is the theoretical fitting curve basing on Equation (6.8). (b) Plot of the nonlinear refractive index (n_2) as a function of linear refractive index (n_0) and the theoretical fitting curve according to Equation (6.9).

Chalcogenide glasses are regarded as amorphous semiconductors, whose nonlinear properties depend greatly on the optical bandgap E_g^{opt}. For direct gap semiconductors, universal relationships for predicting bound-electronic nonlinearities have been developed by Sheik-Bahae *et al.* [256]. This two-parabolic-band model provides information about the dispersion, band-gap scaling as well as the relation between the nonlinear refractive index and two-photon absorption through Kramer-Kronig (K-K) transformation. The comparatively simple yet accurate expression can be given as:

$$n_2 = \frac{AG}{n_0^2 (E_g^{opt})^4} \left(\frac{h\nu}{E_g^{opt}}\right) \tag{6.10}$$

$$\beta = \frac{BF}{n_0^2 (E_g^{opt})^3} \left(\frac{h\nu}{E_g^{opt}}\right) \tag{6.11}$$

where A and B are both material-independent constants; G($h\nu/E_g^{opt}$) and F($h\nu/E_g^{opt}$) are both dispersion functions. Both n_2 and β depend strongly on E_g^{opt}, while the dependences of n_2 and β upon n_0 become much less predominant. It has been indicated that when normalized photon energy ($h\nu/E_g^{opt}$) approaches 0.53 where two photon absorption starts to occur, the dispersion function G is greatly enhanced which gives rise to maximum value of n_2. At the same time, the function F shows a broad peak at $h\upsilon/E_g^{opt} \approx 0.7$ and β reaches its maximum. A different model was proposed by Dinu [257] for the case of indirect gap semiconductors where the situation is somewhat more complex. The spectral dependences of nonlinear optical properties show that the nonlinear refractive index is always positive below the indirect bandgap and has a maximum when $h\upsilon/E_g^{opt} \approx 0.65$. Compared to direct gap semiconductors, the dispersion of two photo absorption is reduced where β passes through a maximum slightly above the indirect bandgap at $h\upsilon/E_g^{opt} \approx 7/6$.

To compare our data with the theoretical nonlinear dispersion spectral presented in previous studies [256,257], the experimental values for n_2 and β were multiplied by factors of $n_0^2(E_g^{opt})^4$ and $n_0^2(E_g^{opt})^3$ and are replotted in Figure 6.12(a), (b) respectively. Clearly the scaled values of n_2 as a function of $h\upsilon/E_g^{opt}$ neither shows any sign of the maximum at $h\upsilon/E_g^{opt} \approx 0.53$ predicted by the Sheik-Bahae model (dashed line), nor extends far enough to confirm the existence of the maximum around 0.65 as analyzed by the Dinu model (solid line), although in most respects the experimental data shown in Figure 6.12 are well located around the theoretical curve for indirect semiconductors (within a standard deviation of 12%). The residual scatter in the data, especially in Figure 6.12(a), could easily originate from uncertainty in the value of the optical bandgap. Since even using thin samples, the influence of tail states due to disorder and defects is difficult to eliminate from the Tauc plots and neither of two models takes such states into account. The dispersion of Kerr nonlinear coefficient and two photon absorption coefficient may not exactly correspond to either of the published models, the overall feature shown in Figure 6.12, however, do suggest that it is possible to predict the magnitude of third-order nonlinear optical parameters (n_2 and β) in chalcogenide glasses by a general relationship between the photon energy ($h\nu$), optical bandgap (E_g^{opt}) and linear index (n_0). Meanwhile, caution should be exercised when this relation is applied to estimate nonlinearities. Since different methods are used to define the optical bandgap of chalcogenide glasses [13,19,230], this sometimes can cause considerable discrepancy between the theory and measurements. We stress that accurate measurements using Tauc plots in thin samples are essential to reveal the trends in Figure 6.12.

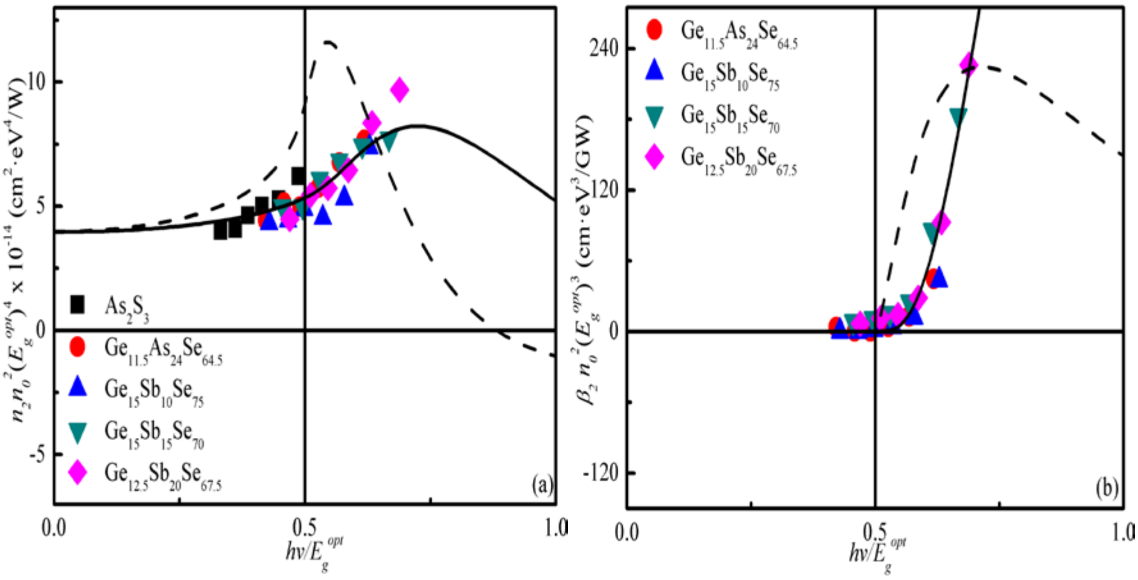

Figure 6.12. (a) Normalized nonlinear refractive index, $n_2 n_0^2(E_g^{opt})^4$, plotted as a function of normalized photon energy. (b) Normalized two photon absorption, $\beta n_0^2(E_g^{opt})^3$, plotted as a function of normalized photon energy. The solid line is fitting according to Dinu's model [257] and the dashed line is Sheik-Bahae's model [256].

For nonlinear devices, a high figure of merit, equivalent to a large nonlinear refractive with minimal absorption is preferable. As shown in Figure 6.12, β is negligible when $h\upsilon/E_g^{opt} \leq 0.5$ for both experimental and theoretical results; therefore it is expected that chalcogenide glasses with $E_g^{opt} \geq 1.65$ eV are suitable for signal processing in the telecommunications band (1500 - 1550 nm). Table 6.3 suggest that As_2S_3, $Ge_{11.5}As_{24}Se_{64.5}$ and $Ge_{15}Sb_{10}Se_{75}$ glasses appear to be the best candidates for nonlinear photonics operating at optical communication wavelengths, since figures of merit for these glasses are much higher than 10 at 1550 nm which satisfies the criterion for use in all-optical processing devices. It also suggests that there will be a limit to the nonlinearity that can be obtained since in general the optical bandgap becomes smaller as the linear (and nonlinear) index increases. Thus, it becomes impossible to obtain the highest nonlinear index without strong two-photon absorption. In practice this appears to limit the maximum nonlinearity of the chalcogenides for all-optical processing at telecommunications wavelengths to about 10^{-13} cm^2/W.

6.5 Conclusions

The linear and nonlinear optical properties of a wide range of chalcogenide glasses have been systematically studied. The linear refractive indices (n_0) of these glasses are closely correlated to their molar volumes as well as electronic structures which are sensitive to composition. A simple but very good estimate of nonlinear refractive indices n_2 can be obtained by easily measuring n_0 and the semi-empirical Miller's rule is probably the best way of predicting the nonlinearity of chalcogenides. The dispersion of the nonlinearities do not seem to reproduce some of the more pronounced details of the direct gap semiconductor model introduced by Sheik-Bahae but is quite consistent with the Dinu model for indirect gap semiconductors. It has been found that higher optical nonlinearities of chalcogenide glasses may correlate intrinsically with their smaller optical bandgap. $Ge_{11.5}As_{24}Se_{64.5}$ and $Ge_{15}Sb_{10}Se_{75}$ glasses show larger nonlinear refractive index with negligible nonlinear absorption at the telecommunication wavelengths. The optimized figures of merit demonstrate that these compositions have great potential for all-optical switching and processing.

Chapter 7

Conclusions and Future Work

7.1 Summary of results

The work presented in this thesis aimed to understand how the chemical compositions and mean coordination numbers can affect the structure and physical properties of ternary $Ge_xAs_ySe_{100-x-y}$ bulk chalcogenide glasses, and ultimately to identify the best materials for photonic devices.

In **Chapter 3**, two experimental techniques, *viz*. Raman scattering and Extended X-ray Absorption Fine Structure spectroscopy were employed to investigate structure of Ge-As-Se compositions. It was found that each constituent atom follows the 8-*N* rule, suggesting that the coordination numbers of Ge, As, Se are 4, 3 and 2 respectively. Selenium chains and ring-like molecules are the dominant structural units in Se-rich glasses with lower mean coordination number $<r>$, which follows chemically ordered network model. With increasing of germanium and arsenic concentrations, the length of selenium chains is reduced and ring-like molecules are broken as they are progressively crosslinked by atoms having higher coordination numbers. $GeSe_{4/2}$ tetrahedral and $AsSe_{3/2}$ pyramidal structural units become the backbone of the network, leading to increased network dimensionality from 1D chains type of structures into a 3D-like continuous network. When there are not enough Se atoms to covalently bond to Ge and

As atoms, As-As bonds are the first homopolar bonds to form in the slightly and moderately Se-poor glasses with higher <*r*>. The existence of arsenic rich clusters does not destroy the connectivity of network. It seems that chemically ordered network model fails to predict atomic bonding in Se-poor glasses.

In **Chapter 4**, the glass transition temperature T_g, the activation energy for enthalpy relaxation E_a and fragility index m of Ge-As-Se system have been investigated by Differential Scanning Calorimetry (DSC). T_g monotonically increases as the values of mean coordination number <*r*> change from 2.20 to 2.86, which indicates an increase in structural rigidity and bond strength. Meanwhile, there is no evidence of intermediate phase. Activation energy shows a single minimum at <*r*> = 2.40 but no clear relation to the deviation from stoichiometry. The trend in the fragility index, however, shows an opposite behavior. A net minimum of the fragility index is found for stoichiometric compositions while no clear tendency is obtained as a function of <*r*>.

In **Chapter 5**, the elastic properties (the shear modulus G, Young’s modulus E, bulk modulus K and Poisson’s ratio v) of Ge-As-Se chalcogenide have been investigated in depth. The variation of density ρ and molar volume V_m as a function of mean coordination number <*r*> both show local extrema at <*r*> = 2.40 and <*r*> ≈ 2.65, which correspond to rigidity percolation threshold (floppy to rigid transition) and structural dimensionality threshold (2D to 3D transition) respectively. The dependence of elastic moduli on <*r*> shows two transition thresholds as well, although there are minor differences in values of <*r*>. This implies that elastic properties of Ge-As-Se system are more sensitive to the structural characteristics of medium range order.

In **Chapter 6**, the variation of averaged linear refractive index n_0 with mean coordination number <*r*> in Ge-As-Se system follows the same changing trend as density, with a local maximum at <*r*> = 2.45 and a minimum at <*r*> = 2.65. It was found that electronic polarizability, density and structural configuration of glasses all contribute to changes in the linear refractive index. The result shows that estimation of the linear refractive index of chalcogenide glasses from other physical parameters is practicable. The measured values of nonlinear refractive index n_2 at 1550 nm are in agreement with the semi-empirical Miller's rule, implying that glasses with high linear refractive index are expected to have high nonlinear refractive index. Substituting antimony for arsenic into the glass matrix will increase the third order nonlinearity but reduce the optical bandgap accompanied by significant two-photon absorption. The dispersion of normalized real and imaginary part of the nonlinearity seems to fit the indirect gap semiconductors models to a large extent, which could be helpful for obtaining desirable nonlinearities for various optical device applications.

The main questions posed in **Section 1.2** as the objectives of this study, at last, can be briefly answered below:

1. How do chemical compositions and structures affect variations of different physical properties within Ge-As-Se system?

- The stoichiometric or near stoichiometric Ge-As-Se compositions containing small amount of Se-Se homopolar bonds exhibit the lowest values of fragility index. The existence of layer-like structures in Ge-As-Se system seems to have little effect on their elastic constants. As/Ge ratio can directly affect the changes of linear refractive index and correspondingly shows indirect effects on third-order nonlinearity of materials.

2. Which factor, chemical effects or topological effects, is more effective in controlling the diverse physical properties of ternary Ge-As-Se glasses?

- The fragility of Ge-As-Se chalcogenide system appears to be effectively controlled by the chemical effects. The density, molar volume, elastic constants, linear and nonlinear refractive index of Ge-As-Se glasses, however, are all predominantly determined by the topological effects.

3. Is it possible to predict any property changes in Ge-As-Se glass family?

- It is quite clear that the variations of mechanical and optical properties of Ge-As-Se glass family are highly predictable due to their close relationships with the mean coordination number.

4. What would be the probable applications of these bulk materials in the coming decades?

- Since strong glass formers possess covalently bonded network with high resistance against structural degradation, the stoichiometric and slightly Se-rich (≤ 10%) $Ge_xAs_ySe_{100-x-y}$ chalcogenide glasses with mean coordination number between 2.45 and 2.50 seem to be the most potential compositions for application in photonics. Meanwhile the present results suggest that, some compositional selection criteria for Ge-As-Se chalcogenide glasses to be used in photonic devices should also be met including high glass transition temperature (T_g > 200°C), the high ratio of As to Ge (As/Ge > 1) and large figures of merit (FOM > 10).

7.2 Suggestions for future work

Though the structure of chalcogenide glasses have been studying for decades, the atomic packing in these materials is still not well understood, even for some simple binary chalcogenides. Most of the structural theories or models, unfortunately, can be merely applied to the limited chalcogenide systems. Meanwhile the existence of intermediate phase as characterized by vanishing of non-reversing enthalpy (ΔH_{nr}) of T_g is also arguable. For these reasons, structural analysis should be further conducted both experimentally and numerically. More sensitive experimental techniques, such as X-ray photoelectron spectra and nuclear magnetic resonance spectra, along with the practical simulation methods can be used to get precise details of the local chemical and geometric environment surrounding each atom in Ge-As-Se chalcogenide glasses. The more universal structural models thus can be developed for reliable glass property predictions.

For Ge-As-Se glasses, several other important physical properties, including hardness and thermal conductivity, need to be studied afterwards. Meanwhile, the similar systematic studies of arsenic-free chalcogenide systems like Ge-Sb-Se and Ge-Sb-Se-Te on their structural, thermal, mechanical and optical properties are significant and necessary, since arsenic is a toxic element and arsenic-containing glasses must be avoided in some applications for health and safety concerns. The results of the investigations are not only a complement to the glass property databases but also vital for designing and fabricating future miniaturized chalcogenide-based devices. In addition, conventional methods, for example thermal evaporation, may not entirely suitable for producing highly-integrated devices with complex structures or particular patterns any more. Thus, further work should also focus on the development and improvement of fabrication techniques.

Publications

Journal Article

[1] T. Wang, X. Gai, W. H. Wei, R. P. Wang, Z. Y. Yang, X. Shen, S. Madden, and B. Luther-Davies, “Systematic z-scan measurements of the third order nonlinearity of chalcogenide glasses,” Optical Materials Express **4**, 1011-1022 (2014).

[2] T. Wang, O. Gulbiten, R. P. Wang, Z. Y. Yang, A. Smith, B. Luther-Davies, and P. Lucas, “Relative contribution of stoichiometry and mean coordination to the fragility of Ge-As-Se glass forming liquids,” Journal of Physical Chemistry B, **118**,1436-1442 (2014).

[3] T. Wang, W. H. Wei, X. Shen, R. P. Wang, B. Luther-Davies, and I. Jackson, “Elastic transition thresholds in Ge-As(Sb)-Se glasses,” Journal of Physics D: Applied Physics, **46**, 165302 (2013).

[4] Y. Yu, X. Gai, T. Wang, P. Ma, R. P. Wang, Z. Y. Yang, D. Y. Choi, S. Madden, and B. Luther-Davies, “Mid-infrared supercontinuum generation in chalcogenides,” Optical Materials Express, **3**, 1075-1086 (2013).

[5] R. P. Wang, D. Bulla, A. Smith, T. Wang, and B. Luther-Davies, “Structure and physical properties of $Ge_xAs_ySe_{1-x-y}$ glasses with the same mean coordination number of 2.5,” Journal of Applied Physics, **109**, 023517 (2011).

Conference Paper

[1] T. Wang, R. P. Wang, B. Luther-Davies, “EXAFS study of the local order in Ge-As-Se glasses,” Physics Procedia, **48**, 89-95 (2013).

[2] R. P. Wang, T. Wang, D. Y. Choi, S. Madden, and B. Luther-Davies, “Transition thresholds in $Ge_xAs_ySe_{1-x-y}$ glasses,” International conference on advances in condensed and nano materials, AIP Conference Proceedings, **1394**, 34-37 (2011).

References

[1] K. Tanaka, and K. Shimakawa, *Amorphous chalcogenide semiconductors and related materials* (Springer, New York, 2011).

[2] B. J. Eggleton, B. Luther-Davies, and K. Richardson, "Chalcogenide Photonics," Nature Photon. **5**, 141-148 (2011).

[3] Z. U. Borisova, *Glassy semiconductors* (Plenum Press, New York, 1981).

[4] G. Chen, H. Jain, S. Khalid, J. Li, D. A. Drabold, and S. R. Elliott, "Study of structural changes in amorphous As_2Se_3 by EXAFS under in situ laser irradiation," Solid. State. Commun. **120**, 149-153 (2001).

[5] S. Onari, K. Matsuishi, and T. Arai, "Two phonon vibration spectra of amorphous Ge-S and Ge-Se systems," J. Non-Cryst. Solids **77&78**, 1121-1124 (1985).

[6] Y. Wang, K. Tanaka, T. Nakaoka, and K. Murase, "Effect of nanophase separation on crystallization process in Ge-Se glasses studied by Raman scattering," Physica B **316-317**, 568-571 (2002).

[7] V. G. Ta'eed, N. J. Baker, L. B. Fu, K. Finsterbusch, M. R. E. Lamont, D. J. Moss, H. C. Nguyen, B. J. Eggleton, D. Y. Choi, S. Madden, and B. Luther-Davies, "Ultrafast all-optical chalcogenide glass photonic circuits," Opt. Express **15**, 9205-9221 (2007).

[8] X. Gai, T. Han, A. Prasad, S. Madden, D. Y. Choi, R. P. Wang, D. Bulla, and B. Luther-Davies, "Progress in optical waveguides fabricated from chalcogenide glasses," Opt. Express **18**, 26635-26646 (2010).

[9] K. Suzuki, Y. Hamachi, and T. Baba, "Fabrication and characterization of chalcogenide glass photonic crystal waveguides," Opt. Express **25**, 22393-22400 (2009).

[10] D. Marchese, M. De Sario, A. Jha, A. K. Kar, and E. C. Smith, "Highly nonlinear GeS_2-based chalcohalide glass for all-optical twin-core-fiber switching," J. Opt. Soc. Am. B **15**, 2361-2370 (1998).

[11] P. A. Thielen, L. B. Shaw, P. C. Pureza, V. Q. Nguyen, J. S. Sanghera, and

I. D. Aggarwal, “Small-core As-Se fiber for Raman amplification,” Opt. Lett. **28**, 1406-1408 (2003).

[12] J. T. Gopinath, M. Soljačić, E. P. Ippen, V. N. Fuflyigin, W. A. King, and M. Shurgalin, “Third order nonlinearities in Ge-As-Se-based glasses for telecommunications applications,” J. Appl. Phys. **96**, 6931-6933 (2004).

[13] L. Petit, N. Carlie, H. Chen, S. Gaylord, J. Massera, G. Boudebs, J. Hu, A. Agarwal, L. Kimerling, and K. Richardson, “Compositional dependence of the nonlinear refractive index of new germanium-based chalcogenide glasses,” J. Solid State Chem. **182**, 2756-2761 (2009).

[14] P. J. Webber, and J. A. Savage, “Some physical properties of Ge-As-Se infrared optical glasses,” J. Non-Cryst. Solids **20**, 271-283 (1976).

[15] M. A. Popescu, *Non-Crystalline chalcogenides* (Kluwer Academic, Dordrecht, 2001).

[16] H. L. Ma, X. H. Zhang, J. Lucas, H. Senapati, R. Bohmer, and C. A. Angell, “Covalent bond connectivity, medium range order, and physical properties in TeX and TeXAs glasses,” J. Solid State Chem. **96**, 181-191 (1992).

[17] J. C. Phillips, “Topological of covalent non-crystalline solids I: short-range order in chalcogenide alloys,” J. Non-Cryst. Solids **34**, 153-181 (1979).

[18] M. F. Thorpe, “Continuous deformations in random networks,” J. Non-Cryst. Solids **57**, 355-370 (1983).

[19] A. Prasad, C. J. Zha, R. P. Wang, A. Smith, S. Madden, and B. Luther-Davies, “Properties of $Ge_xAs_ySe_{1-x-y}$ glasses for all-optical signal processing,” Opt. Express **16**, 2804-2815 (2008).

[20] G. Yang, H. S. Jain, A. T. Ganjoo, D. H. Zhao, Y. S. Xu, H. D. Zeng, and G. R. Chen, “A photo-stable chalcogenide glass,” Opt. Express **16**, 10565-10571 (2008).

[21] Y. Yu, X. Gai, T. Wang, P. Ma, R. P. Wang, Z. Y. Yang, D. Y. Choi, S. Madden, and B. Luther-Davies, “Mid-infrared supercontinuum generation in chalcogenides,” Opt. Mater. Express **3**, 1075-1086 (2013).

[22] K. Tanaka, “Photoinduced processes in chalcogenide glasses”, Curr. Opin. Solid

State Mater. Sci. **1**, 567-571 (1996).

[23] J. S. Sanghera, L. B. Shaw, and I. D. Aggarwal, "Applications of chalcogenide glass optical fibers," C. R. Chimie **5**, 873-883 (2002).

[24] A. Zakery, and S. R. Elliott, "Optical properties and applications of chalcogenide glasses: a review," J. Non-Cryst. Solids **330**, 1-12 (2003).

[25] B. J. Eggleton, "Chalcogenide photonics: fabrication, devices and applications introduction", Opt. Express, **18** , 26632-26634 (2010).

[26] R. Frerichs, "New optical glasses transparent in the infrared up to 12μ", Phys. Rev. **78**, 643 (1950).

[27] R. Frerichs, "New optical glasses with good transparency in the infrared", J. Opt. Soc. Am. **43**, 1153-1157 (1953).

[28] F. W. Glaze, D. H. Blackburn, J. S. Osmalov, D. Hubbard, and M. H. Black, "Properties of arsenic sulfide glass," J. Res. Nat. Bur. Stand. **59**, 83-92 (1957).

[29] J. A. Savage, and S. Nielsen, "Chalcogenide glasses transmitting in the infrared between 1 and 20μ – a state of the art review," Infrared Phys. **5**, 195-204 (1965).

[30] A. R. Hilton, "Nonoxide chalcogenide glasses as infrared optical materials," Appl. Opt. **5**, 1877-1882 (1966).

[31] B. T. Kolomiets, "Vitreous semiconductors (I)," Phys. Status Solidi B **7**, 359-372(1964).

[32] B. T. Kolomiets, "Vitreous Semiconductors (II)," Phys. Status Solidi B **7**, 713-731 (1964).

[33] M. A. Green, K. Emery, Y. Hishikawa, and W. Warta, "Solar cell efficiency tables (version 37)," Prog. Photovolt.: Res. Appl. **19**, 84-92 (2011).

[34] S. R. Ovshinsky, "Reversible electrical switching phenomena in disordered structures," Phys. Rev. Lett. **21**, 1450-1453 (1968).

[35] S. R. Ovshinsky, "An introduction of ovonic research," J. Non-Cryst. Solids **2**, 99-106 (1970).

[36] G. Pfister, "Electronic properties of chalcogenide glasses and their use in xerography," J. Electron. Mater. **8**, 789-837 (1979).

[37] A. B. Seddon, "Chalcogenide glasses: a review of their preparation, properties

and applications, J. Non-Cryst. Solids **184**, 44-50 (1995).

[38] J. S. Sanghera, and I. D. Aggarwal, “Active and passive chalcogenide glass optical fibers for IR applications: a review,” J. Non-Cryst. Solids **256&257**, 6-16 (1999).

[39] B. Bureau, X. H. Zhang, F. Smektala, J. L. Adam, J. Troles, H. L. Ma, C. B. Plèdel, J. Lucas, P. Lucas, D. L. Coq, M. R. Riley, and J. H. Simmons, “Recent advances in chalcogenide glasses,” J. Non-Cryst. Solids **345&346**, 276-283 (2004).

[40] S. R. Elliott, “Medium-range structural order in covalent amorphous solids,” Nature **354**, 445-452 (1991).

[41] S. Sen, and B. G. Aitken, “Atomic structure and chemical order in Ge-As selenide and sulfoselenide glasses: An x-ray absorption fine structure spectroscopic study,” Phys. Rev. B **66**, 134204 (2002).

[42] P. Armand, A. Ibanez, H. Dexpert, D. Bittencourt, D. Raoux, and E. Philippot, “Structural approach of Ge-X, GeX2-Ag2X (X=S, Se) glassy systems”, J. Phys. IV **C2**, 189-194 (1992).

[43] M. Popescu, F. Sava, and A. Lőrinczi, “A new model for the structure of chalcogenide glasses: The closed cluster model”, J. Non-Cryst. Solids **355**, 1815-1819 (2009).

[44] R. Svoboda, “Relaxation processes in Se-rich chalcogenide glasses: Effect of characteristic structural entities”, Acta Mater. **61**, 4534-4541 (2013).

[45] W. H. Zachariasen, “The atomic arrangement in glass,” J. Am. Chem. Soc. **54**, 3841-3851 (1932).

[46] N. F. Mott, “Electrons in disordered structures,”Adv. in Phys. **16**, 49-144 (1967).

[47] F. Betts, A. Bienenstock, and S. R. Ovshinsky, “Radial distribution studies of amorphous Ge_xTe_{1-x} alloy,” J. Non-Cryst. Solids **4**, 554-563 (1970).

[48] R. W. Fawcett, C. N. J. Wagner, and G. S. Cargill III, “Radial distribution studies of amorphous Ge_xSe_{1-x} alloy films,” J. Non-Cryst. Solids **8-10**, 369-375 (1972).

[49] G. Lucovsky, and T. M. Hayes, “Short-range order in amorphous

semiconductors” in *Amorphous semiconductors*, M. H. Brodsky (ed.) (Springer-Verlag, Berlin, 1979).

[50] J. C. Phillips, “Topological of covalent non-crystalline solids I: short-range order in chalcogenide alloys,” J. Non-Cryst. Solids **34**, 153-181 (1979).

[51] M. F. Thorpe, “Continuous deformations in random networks,” J. Non-Cryst. Solids **57**, 355-370 (1983).

[52] B. L. Halfpap, and S. M. Lindsay, “Rigidity percolation in the germanium-arsenic-selenium alloy system,” Phys. Rev. Lett. **57**, 848-849 (1986).

[53] S. Mahadevan, and A, Giridhar, “On the chemical and mechanical thresholds of some chalcogenide glasses,” J. Non-Cryst. Solids **110**, 118-121 (1989).

[54] A. K. Varshneya, “Some comments on physical properties of chalcogenide glasses,” J. Non-Cryst. Solids **273**, 1-7 (2000).

[55] R. J. Nemanich, “Low-frequency inelastic light scattering from chalcogenide glasses and alloys” Phys. Rev. B, **16**, 1655-1674 (1977).

[56] A. A. Vaipolin, and E. A. Porai-Koshits, “Structural models of glasses and the structures of crystalline chalcogenides,” Sov. Phys-Solid State **5**, 497-500 (1963).

[57] J. C. Phillips, “Topological of covalent non-crystalline solids II: Medium-range order in chalcogenide alloys and a-Si(Ge),” J. Non-Cryst. Solids **43**, 37-77 (1981).

[58] K. Tanaka, “Structural phase transitions in chalcogenide glasses,” Phys. Rev. B **39**, 1270-1279 (1989).

[59] M. Popescu, and H. Bradaczeka, “Microparacrystalline model for medium-range order in non-crystalline chalcogenide,” J. Optoelectron. Adv. Mater. **3**, 249-254 (2001).

[60] V. S. Minaev, “Polymorphous-crystalloid structure and relaxation process in some chalcogenide glass-forming substances,” J. Optoelectron. Adv. Mater. **3**, 233-248 (2001).

[61] P. Boolchand, D. G. Georgiev, and B. Goodman, “Discovery of the intermediate phase in chalcogenide glasses,” J. Optoelectron. Adv. Mater. **3**,

703-720 (2001).

[62] F. Wang, S. Mamedov, P. Boolchand, B. Goodman, and M. Chandrasekhar, “Pressure Raman effects and internal stress in network glasses,” Phys. Rev. B **71**, 1742018 (2005).

[63] Y. Wang, P. Boolchand, and M. Micoulaut, “Glass structure, rigidity transitions and the intermediate phase in the Ge-As-Se ternary,” Europhys. Lett. **52**, 633-639 (2000).

[64] P. Boolchand, P. Chen, and U. Vempati1, “Intermediate Phases, structural variance and network demixing in chalcogenides: The unusual case of group V sulfides,” J. Non-Cryst. Solids **355**, 1773-1785 (2009).

[65] H. Y. Zhao, Y. P. Koh, M. Pyda, S. Sen, and S. L. Simon, “The kinetics of the glass transition and physical aging in germanium selenide glasses,” J. Non-Cryst. Solids **368**, 63-70 (2013).

[66] H. L. Ma, X. H. Zhang, J. Lucas, and C. T. Moynihan, “Relaxation near room temperature in tellurium chalcohalide glasses,” J. Non-Cryst. Solids **140**, 209-214 (1992).

[67] J. Rault, “Origin of the Vogel-Fulcher-Tammann law in glass-forming materials: the α-β bifurcation,” J. Non-Cryst. Solids **271**, 177-217 (2000).

[68] D. Turnbull, and M. H. Cohen, “Free-volume model of the amorphous phase: glass transition,” J. Chem. Phys. **34**, 120-125 (1961).

[69] J. H. Gibbs, and E. A. Dimarzio, “Nature of the glass transition and the glassy state,” J. Chem. Phys. **28**, 373-383 (1958).

[70] K. L. Ngai, “Modification of the Adam-Gibbs model of glass transition for consistency with experimental data,” J. Phys. Chem. B **103**, 5895-5902 (1999).

[71] C. T. Moynihan, and P. K. Gupta, “The order parameter model for structural relaxation in glass,” J. Non-Cryst. Solids **29**, 143-158 (1978).

[72] G. H. Fredrickson, and H. C. Andersen, “Kinetic ising model of the glass transition,” Phys. Rev. B **53**, 1244-1247 (1984).

[73] O. S. Narayanaswamy, “A model of structural relaxation in glass,” J. Am. Ceram. Soc. **54**, 491-498 (1971).

[74] M. Goldstein, “Viscous liquids and the glass transition: a potential energy barrier picture,” J. Chem. Phys. **51**, 3728-3739 (1969).

[75] P. W. Anderson, “Through the glass lightly,” Science **267**, 1609-1618 (1995).

[76] P. G. Debenedetti, and F. H.Stillinger, “Supercooled liquids and the glass transition,” Nature **410**, 259-267 (2001).

[77] G. B. McKenna, “Diverging views on glass transition,” Nature Phys. **4**, 673-674 (2008).

[78] R. Kerner, and M. Micoulaut, “On the glass transition temperature in covalent glasses,” J. Non-Crys. Solids **210**, 298-305 (1997).

[79] W. Kauzmann, “The nature of the glassy state and the behavior of liquids at low temperatures,” Chem. Rev. **43**, 219-256 (1948).

[80] K. Tanaka, “Glass transition of covalent glasses,” Solid State Commun. **54**, 867-869 (1985).

[81] A. N. Sreeram, D. R. Swiler, and A. K. Varshneya, “Gibbs-DiMarzio equation to describe the glass transition temperature trends in multicomponent chalcogenide glasses,” J. Non-Cryst. Solids **127**, 287-297 (1991).

[82] L. Tichý, and H. Tichá, “Covalent bond approach to the glass-transition temperature of chalcogenide glasses,” J. Non-Cryst. Solids **189**, 141-146 (1995).

[83] J. E. Shelby, *Introduction to glass science and technology*, 2nd edition (Royal Society of Chemistry, Cambridge, 2005).

[84] T. Rouxel, “Elastic properties and short-to medium-range order in glasses,” J. Am. Ceram. Soc. **90**, 3019-3039 (2007).

[85] J. S. Mccloy, “Methods for prediction of refractive index in glasses for the infrared,” Proc. SPIE **8016**, 80160G (2011).

[86] S. H. Wemple, and M. Didomenico, Jr., “Behavior of the electronic dielectric constant in covalent and ionic materials,” Phys. Rev. B **3**, 1338-1351 (1971).

[87] J. Tauc, “Optical properties and electronic structure of amorphous Ge and Si,” Mater. Res. Bull. **3**, 37-46 (1968).

[88] F. Urbach, “The long-wavelength edge of photographic sensitivity and of the

electronic absorption of solids," Phys. Rev. **92**, 1324 (1953).

[89] R. C. Zeller, and R. O. Pohl, "Thermal conductivity and specific heat of noncrystalline solids," Phys. Rev. B **4**, 2029-2041 (1971).

[90] J. Singh, and K. Shimakawa, *Advances in amorphous semiconductors* (Taylor & Francis, London, 2003)

[91] J. Singh, "Radiative lifetime of excitons in chalcogenide glasses" J. Optoelectron. Adv. Mater. **9**, 3013-3020 (2007).

[92] K. Morigaki, *Physics of amorphous semiconductors* (Imperial College Press, London, 1999).

[93] K. Shimakawa, "On the compositional dependence of the optical gap in amorphous semiconductor alloys," J. Non-Cryst. Solids **43**, 229-244 (1981).

[94] R. W. Boyd, *Nonlinear Optics* (Academic Press, San Diego, 1992).

[95] V. Mizrahi, K. W. DeLong, G. I. Stegeman, M. A. Saifi, and M. J. Andrejco, "Two-photon absorption as a limitation to all-optical switching," Opt. Lett. **14**, 1140-1142 (1989).

[96] K. Tanaka, "Two-photon absorption spectroscopy of As_2S_3 glass," Appl. Phys. Lett. **80**, 177-179 (2002).

[97] G. Boudebs , S. Cherukulappurath , M. Guignard , J. Troles , F. Smektala, and F. Sanchez, "Experimental observation of higher order nonlinear absorption in tellurium based chalcogenide glasses," Opt. Commun. **232**, 417-423 (2004).

[98] J. S. Sanghera, C. M. Florea, L. B. Shaw, P. Pureza, V. Q. Nguyen, M. Bashkansky, Z. Dutton, and I. D. Aggarwal, "Non-linear properties of chalcogenide glasses and fibers," J. Non-Cryst. Solids **354**, 462-467 (2008).

[99] N. F. Mott, and E. A. Davis, *Electronic process in non-crystalline materials* (Oxford University Press Inc, New York, 2012).

[100] J. M. Marshall, and A. E. Owen, "Drift mobility studies in vitreous arsenic triselenide," Philos. Mag. **24**, 1281-1305 (1971).

[101] M. H. Cohen, H. Fritzsche, and S. R. Ovshinsy, "Simple band model for amorphous semiconductor alloys," Phys. Rev. Lett. **22**, 1065-1072 (1969).

[102] D. Emin, C. H. Seager, and R. K. Quinn, "Small-polaron hopping motion in

some chalcogenide glasses," Phys. Rev. Lett. **28**, 813-816 (1972).

[103] M. Kastner, "Bonding bands, lone-pair bands, and impurity states in chalcogenide semiconductors," Phys. Rev. Lett. **28**, 355-357 (1972).

[104] S. R. Ovshinsky, "Reversible electrical switching phenomena in disordered structures," Phys. Rev. Lett. **21**, 1450-1453 (1968).

[105] M. Popescu, "Disordered chalcogenide optoelectronic materials: phenomenon and applications," J. Optoelectron. Adv. Mater. **7**, 2189-2210 (2005).

[106] B. Bureau, C. Boussard, S. Cui, R. Chahal, M. L. Anne, V. Nazabal, O. Sire, O. Loréal, P. Lucas, V. Monbet, J. L. Doualan, P. Camy, H. Tariel, F. Charpentier, L. Quetel, J. L. Adam, and J. Lucas, "Chalcogenide optical fibers for mid-infrared sensing," Opt. Eng. **53**, 027101 (2014).

[107] M. Asobe, T. Kanamori, and K. Kubodera, "Applications of highly nonlinear chalcogenide glass fibers in ultrafast all-optical switches," IEEE J. Quantum Electron **29**, 2325-2333 (1993).

[108] M. Asobe, T. Ohara, I. Yokohama, and T. Kaino, "Low power all-optical switching in a nonlinear optical loop mirror using chalcogenide glass fibre," Electron. Lett. **32**, 1396-1397 (1996).

[109] M. D. Pelusi, V. G. Ta'eed, M. R. E. Lamont, S. Madden, D. Y. Choi, B. Luther-Davies, and B. J. Eggleton, "Ultra-high nonlinear As_2S_3 planar waveguide for 160-Gb/s optical time-division demultiplexing by four-wave mixing," IEEE Photon. Technol. Lett. **19**, 1496-1498 (2007).

[110] M. Galili, J. Xu, H. C. H. Mulvad, L. K. Oxenløwe, A. T. Clausen, P. Jeppesen, B. Luther-Davies, S. Madden, A. Rode, D. Y. Choi, M. Pelusi, F. Luan, and B. J. Eggleton, "Breakthrough switching speed with an all-optical chalcogenide glass chip: 640 Gbit/s demultiplexing," Opt. Express **17**, 2182-2187 (2009).

[111] T. D. Vo, H. Hu, M. Galili, E. Palushani, J. Xu, L. K. Oxenløwe, S. J. Madden, D. Y. Choi, D. A. P. Bulla, M. D. Pelusi, J. Schröder, B. Luther-Davies, and B. J. Eggleton, "Photonic chip based transmitter optimization and receiver demultiplexing of a 1.28 Tbit/s OTDM signal," Opt. Express **18**, 17252-17261 (2010).

[112] L. B. Fu, M. Rochette, V. G. Ta'eed, D. J. Moss, and B. J. Eggleton, "Investigation of self-phase modulation based optical regeneration in single mode As_2Se_3 chalcogenide glass fiber," Opt. Express **13**, 7637-7644 (2005).

[113] V. G. Ta'eed, M. Shokooh-Saremi, L. B. Fu, D. J. Moss, M, Rochette, I. C. M. Littler, B. J. Eggleton, Y. L. Ruan, and B. Luther-Davies, "Integrated all-optical pulse regenerator in chalcogenide waveguides," Opt. Lett. **30**, 2900-2902 (2005).

[114] M. D. Pelusi , F. Luan, S. Madden, D. Y. Choi, D. A. Bulla, B. Luther-Davies, and B. J. Eggleton, "Wavelength conversion of high-speed phase and intensity modulated signals using a highly nonlinear chalcogenide glass chip," IEEE Photon. Technol. Lett. **22**, 3-5 (2010).

[115] V. G. Ta'eed, M. R. E. Lamont, D. J. Moss, B. J. Eggleton, D. Y. Choi, S. Madden, and B. Luther-Davies, "All optical wavelength conversion via cross phase modulation in chalcogenide glass rib waveguides," Opt. Express **14**, 11242-11247 (2006).

[116] M. R. E. Lamont, V. G. Ta'eed, M. A. F. Roelens, D. J. Moss, B. J. Eggleton, D. Y. Choi, S. Madden, and B. Luther-Davies, "Error-free wavelength conversion via cross-phase modulation in 5cm of As_2S_3 chalcogenide glass rib waveguide," Electron. Lett. **43**, 945-947 (2007).

[117] J. Fick, É. J. Knystautas, A. Villeneuve, F. Schiettekatte, S. Roorda, and K. A. Richardson, "High photoluminescence in erbium-doped chalcogenide thin films," J. Non-Cryst. Solids **272**, 200-208 (2000).

[118] J. J. Hu, V. Tarasov, N. Carlie, N. N. Feng, L. Petit, A. Agarwal, K. Richardson, and L. Kimerling, "Si-CMOS-compatible lift-off fabrication of low-loss planar chalcogenide waveguides," Opt. Express **15**, 11798-11807 (2007).

[119] J. A. Frantz, L. B. Shaw, J. S. Sanghera, and I. D. Aggarwal "Waveguide amplifiers in sputtered films of Er^{3+}-doped chalcogenide glass," Opt. Express **14**, 1797-1803 (2006).

[120] T. Sabapathy, A. Ayiriveetil, A. K. Kar, S. Asokan, and S. J. Beecher "Direct ultrafast laser written C-band waveguide amplifier in Er-doped chalcogenide

glass," Opt. Mater. Express **2**, 1556-1561 (2012).

[121] T. Schweizer, F. Goutaland, E. Martins, D. W. Hewak, and W. S. Brocklesby, "Site-selective spectroscopy in dysprosium-doped chalcogenide glasses for 1.3 micron optical-fiber amplifiers," J. Opt. Soc. Am. B **18**, 1436-1442 (2001).

[122] J. Heo, "Rare-earth doped chalcogenide glasses for fiber-optic amplifier," J. Non-Cryst. Solids **326 & 327**, 410-415 (2003).

[123] M. D. Sario, L. Mescia, F. Prudenzano, F. Smektala, F. Deseveday, V. Nazabal, J. Troles, and L. Brilland, "Feasibility of Er^{3+}-doped, $Ga_5Ge_{20}Sb_{10}S_{65}$ chalcogenide microstructured optical fiber amplifiers," Opt. Laser Technol. **41**, 99-106 (2009).

[124] S. P. Smith, F. Zarinetchi, and S. Ezekiel, "Narrow-linewidth stimulated Brillouin fiber laser and applications," Opt. Lett. **16**, 393-395 (1991).

[125] G. J. Cowle, and D. Y. Stepanov, "Multiple wavelength generation with Brillouin/Erbium fiber lasers," IEEE Photon. Tech. Lett. **8**, 1465-1467 (1996).

[126] H. H. Kee, G. P. Lees, and T. P. Newson, "All-fiber system for simultaneous interrogation of distributed strain and temperature sensing by spontaneous Brillouin scattering," Opt. Lett. **25**, 695-697 (2000).

[127] K. Kotate, and M. Tanaka, "Distributed fiber Brillouin strain sensing with 1-cm spatial resolution by correlation-based continuous-wave technique," IEEE Photon. Tech. Lett. **14**, 179-181 (2002).

[128] C. N. Pannell, P. St. J. Russell, and T. P. Newson, "Stimulated Brillouin scattering in optical fibers: the effect of optical amplification," J. Opt. Soc. Am. B **10**, 684-690 (1993).

[129] M. Ferreira, J. Rocha, and J. Pinto, "Analysis of the gain and noise characteristics of fibre Brillouin amplifiers," Opt. Quant. Electron. **26**, 35-44 (1994).

[130] R. Pant, C. G. Poulton, D. Y. Choi, H. Mcfarlane, S. Hile, E. B. Li, L. Thevenaz, B. Luther-Davies, S. J. Madden, and B. J. Eggleton, "On-chip stimulated Brillouin scattering," Opt. Express **19**, 8285-8290 (2011).

[131] B. J. Eggleton, C. G. Poulton, and R. Pant, "Inducing and harnessing stimulated

Brillouin scattering in photonic integrated circuits," Adv. Opt. Photonics **5**, 536-587 (2013).

[132] A. Byrnes, R. Pant, E. B. Li, D. Y. Choi, C. G. Poulton, S. H. Fan, S. Madden, B. Luther-Davies, and B. J. Eggleton, "Photonic chip based tunable and reconfigurable narrowband microwave photonic filter using stimulated Brillouin scattering," Opt. Express **20**, 18845-18854 (2012).

[133] R. Pant, E. B. Li, C. G. Poulton, D. Y. Choi, S. Madden, B. Luther-Davies, and B. J. Eggleton, "Observation of Brillouin dynamic grating in a photonic chip," Opt. Lett. **38**, 305-307 (2013).

[134] I. V. Kabakova, R. Pant, D. Y. Choi, S. Debbarma, B. Luther-Davies, S. J. Madden, and B. J. Eggleton, "Narrow linewidth Brillouin laser based on chalcogenide photonic chip," Opt. Lett. **38**, 3208-3211 (2013).

[135] R. R. Gattass, L. B. Shaw, V. Q. Nguyen, P. C. Pureza, I. D. Aggarwal, and J. S. Sanghera, "All-fiber chalcogenide-based mid-infrared supercontinuum source," Opt. Fiber Techno. **18**, 345-348 (2012).

[136] Dong-Il Yeom, M. R. E. Lamont, B. Luther-Davies, and B. J. Eggleton "Supercontinuum generation in chalcogenide glass waveguides," in *Supercontinuum generation in optical fiber*, J. M. Dudley, and T. R. Taylor (ed.) (Cambridge University Press, New York, 2010).

[137] Y. Yu, X. Gai, P. Ma, D. Y. Choi, Z. Y. Yang, R. P. Wang, S. Debbarma, S. J. Madden, and B. Luther-Davies, "A broadband, quasi-continuous, mid-infrared supercontinuum generated in a chalcogenide glass waveguide," Laser Photonics Rev. **8**, 1-7 (2014).

[138] J. A. Savage, "Glass-forming region and DTA survey of some glasses in the Si-Ge-As-Te threshold switching glass system," J. Mater. Sci. **7**, 64-67 (1972).

[139] M. J. Lee, D. Lee, S. H. Cho, J. H. Hur, S. M. Lee, D. H. Seo, D. S. Kim, M. S. Yang, S. Lee, E. Hwang, M. R. Uddin, H. Kim, U. I. Chung, Y. Park, and I. K. Yoo, "A plasma-treated chalcogenide switch device for stackable scalable 3D nanoscale memory," Nat. Commun. **4**, 3629 (2013).

[140] W. Czubatyj, and S. J. Hudgens, "Invited paper: Thin film Ovonic threshold

switch: its operation and application in modern integrated circuits," Electron. Mater. Lett. **8**, 157-167 (2012).

[141] R. G. Neale, and J. A. Aseltine, "The application of amorphous materials to computer memories," IEEE Trans. on Electron Devices **20**, 195-205 (1973).

[142] S. Tyson, G. Wicker, T. Lowrey, S. Hudgens, and K. Hunt, "Nonvolatile, high density, high performance phase-change memory," IEEE Aerospace Conf. Proc. **5**, 385-390 (2000).

[143] S. Hudgens, and B. Johnson, "Overview of phase-change chalcogenide nonvolatile memory technology," MRS Bull. **29**, 829-832 (2004).

[144] A. L. Lacaita, "Phase change memories: state-of-the-art, challenges and perspectives," Solid State Electron. **50**, 24-31 (2006).

[145] F. Q. Huang, C. Y. Yang, and D. Y. Wan, "Advanced solar materials for thin-film photovoltaic cells," Front. Phys. **6**, 177-196 (2011).

[146] Y. E. Romanyuk, H. Hagendorfer, P. Stücheli, P. Fuchs, A. R. Uhl, C. M. Sutter-Fella, M. Werner, S. Haass, J. Stückelberger, C. Broussillou, Pierre-Philippe Grand, V. Bermudez, and A. N. Tiwari, "All solution-processed chalcogenide solar cells-from single functional layers towards a 13.8% efficient CIG device," Adv. Funct. Mater. **25**, 12-27 (2015).

[147] J. Portier, "Halogenide, chalcogenide and chalcogenide glasses: materials, models, applications," J. Non-Cryst. Solids **112**, 15-22 (1989).

[148] B. Prasai, and D. A. Drabold, "Ab initio simulation of solid electrolyte materials in liquid and glassy phases," Phys. Rev. B **83**, 094202 (2011).

[149] I. Kaban, P. Jóvári, T. Wagner, M. Frumar, S. Stehlik, M. Bartos, W. Hoyer, B. Beuneu, and M. A. Webb, "Atomic structure of As_2S_3-Ag chalcogenide glasses," J. Phys: Condens. Matter **21**, 395801 (2009).

[150] R. Golovchak, A. Kovalskiy, A. C. Miller, H. Jain, and O. Shpotyuk, "Structure of Se-rich As-Se glasses by high-resolution x-ray photoelectron spectroscopy," Phys. Rev. B **76**, 125208 (2007).

[151] R. Golovchak, O. Shpotyuk, S. Kozyukhin, A. Kovalskiy, A. C. Miller, and H. Jain, "Structural paradigm of Se-rich Ge-Se glasses by high-resolution x-ray

photoelectron spectroscopy," J. Appl. Phys. **105**, 103704 (2009).

[152] O. N. Bolebrukh, N. Y. Sinyavsky, I. P. Korneva, B. Dobosz, M. Ostafin, B. Nogaj , and R. Krzyminiewski, "Experimental study of the structure of chalcogenide glassy semiconductors in three-component systems of Ge-As-Se and As-Sb-Se by means of NQR and EPR spectroscopy," Cent. Eur. J. Phys. **11**, 1686-1693 (2013).

[153] R. Müllmann, B. D. Mosel and H. Eckert, "Physical and chemical threshold behavior in chalcogenide networks: ^{119}Sn Mössbauer spectroscopy of Ge(Sn)-As-Se glasses" Phys. Chem. Chem. Phys. **1**, 2543-2550 (1999).

[154] X. W. Feng, W. J. Bresser, and P. Boolchand, "Direct evidence for stiffness threshold in chalcogenide glasses," Phys. Rev. Lett. **78**, 4422-4425 (1997).

[155] I. P. Kotsalas, and C. Raptis, "Structural Raman studies of Ge_xS_{1-x} chalcogenide glasses," J. Optoelectron. Adv. Mater. **3**, 675-684 (2001).

[156] M. S. Iovu, E. I. Kamitsos, C. P. E. Varsamis, P. Boolchand, and M. Popescu, "Raman spectra of As_xSe_{100-x} and $As_{40}Se_{60}$ glasses doped with metals," Chalcogenide Lett. **2**, 21-25 (2005).

[157] P. Tronc, M. Bensoussan, and A. Brenac, "Optical-absorption edge and Raman scattering in Ge_xSe_{1-x} glasses," Phys. Rev. B **8**, 5947-5956 (1973).

[158] P. M. Bridenbaugh, G. P. Espinosa, J. E. Griffiths, J. C. Phillips, and J. P. Remeika, "Microscopic origin of the companion A_1 Raman line in glassy $Ge(S,Se)_2$," Phys. Rev. B **20**, 4140-4144 (1977).

[159] N. Mateleshko, V. Mitsa, M. Veresa, and M. Koosa, "Investigation of nanophase separation in glassy $As_{40}Se_{60}$ using Raman scattering and Ab initio calculations," Chalcogenide Lett. **1**, 139-144 (2004).

[160] W. Q. Zhou, M. Paesler, and D. E. Sayers, "Structure of germanium-selenium glasses: An x-ray-absorption fine-structure study," Phys. Rev. B **43**, 2315-2321 (1991).

[161] J. Ledru, J. M. Saiter, G. Saffarini, and S. Benazeth, "An EXAFS investigation of the local order around indium in Ge-Se-In glasses," J. Non-Cryst. Solids **232-234**, 634-637 (1998).

[162] J. L. Wang, J. C. Tsai, C. T. Liu, P. Nachimuthu, L. Y. Jang, R. G. Liu, and J. M. Chen, “Structural properties of the glass system As-Se-S studied by x-ray absorption spectroscopy,” J. Appl. Phys. **88**, 2533-2540 (2000).

[163] G. Vlaic, and L. Olivib, “EXAFS spectroscopy: a brief introduction,” Croat. Chem. Acta **77**, 427-433 (2004).

[164] G. N. Greaves, “X-ray absorption spectroscopy,” in *Glass science and technology*, D. R. Uhlmann, and N. J. Kreidl (ed.) (Academic Press, San Diego, 1990).

[165] R. Parthasarathy, K. J. Rao and C. N. R. Rao, “EXAFS studies of arsenic chalcogenide glasses,” J. Phys. C: Solid State Phys. **15**, 3649-3655 (1982).

[166] P. Fons, “Sub-nanosecond structural snapshots of the optical recording process,” Spring-8 Info. **14**, 159-166 (2009).

[167] M. Popescu, “Photo-induced transformations in glass,” in *Semiconducting chalcogenide glass I: glass formation, structure, and stimulated transformations in chalcogenide glasses*, R. Fairman, and B. Ushkov (ed.) (Academic Press, Amsterdam, 2004).

[168] J. M. Saiter, ‘‘Physical ageing in chalcogenide glasses,’’ J. Optoelectron. Adv. Mater. **3**, 685-694 (2001).

[169] B. Ravel, and M. Newville, “ATHENA, ARTEMIS, HEPHAESTUS: data analysis for X-ray absorption spectroscopy using IFEFFIT,” J. Synchrotron Radiat. **12**, 537-541 (2005).

[170] P. Němec, S. Zhang, V. Nazabal, K. Fedus, G. Boudebs, A. Moreac, M. Cathelinaud, and X. H. Zhang, “Photo-stability of pulsed laser deposited $Ge_xAs_ySe_{100-x-y}$ amorphous thin films,” Optics Express **18**, 22944-22957 (2010).

[171] O. Shpotyuk, R.Golovchak and A. Kozdras, “Physical aging of chalcogenide glasses,” in *Chalcogenide glasses: preparation, properties and applications*, J. L. Adam, and X. H. Zhang (ed.) (Woodhead Publishing, Cambridge, 2014).

[172] M. Olivier, J. C. Tchahame, P. Němec, M. Chauvet, V. Besse, C. Cassagne, G. Boudebs, G. Renversez, R. Boidin, E. Baudet, and V. Nazabal, “Structure, nonlinear properties, and photosensitivity of $(GeSe_2)_{100-x}(Sb_2Se_3)_x$ glasses,” Opt.

Mater. Express **4**, 525-540 (2014).

[173] N. Mateleshko, V. Mitsa, M. Veres, M. Koos, and A. Stronski, "Investigation of nanophase separation in IR optical glasses $As_{40}Se_{60}$ using resonant Raman scattering," Semiconductor Physics, Quantum Electronics and Optoelectronics **7**, 171-174 (2004).

[174] L. Pauling , *The natural of the chemical bond*, (Cornell University Press, New York, 1960).

[175] P. S. Salmon, and I. Petri, "Structure of glassy and liquid $GeSe_2$" J. Phys.: Condens. Matter **15**, S1509-S1528 (2003).

[176] P. Biswas, D. N. Tafen, R. Atta-Fynn, and D. Drabold, "Inclusion of experimental information in first principles modeling of materials," J. Phys.: Condens. Matter **16**, S5173-S5182 (2004).

[177] D. A. Drabold, J. Li, and D. N. Tafen, "Simulations of arsenic selenide glasses," J. Phys.: Condens. Matter **15**, S1529- S1536 (2003).

[178] M. Bauchy, and M. Micoulaut, "Structure of As_2Se_3 and As-Se network glasses: Evidence for coordination defects and homopolar bonding," J. Non-Cryst. Solids **377**, 34-38 (2013).

[179] P. Boolchand, D. G. Georgiev, and M. S. Iovua, "Molecular structure and quenching of photodarkening in As_2Se_3:Sn_x amorphous films," Chalcogenide Lett. **2**, 27-34 (2005).

[180] R. P. Wang, A. Smith, A. Prasad, D. Y. Choi, and B. Luther-Davies, "Raman spectra of $Ge_xAs_ySe_{1-x-y}$ glasses," J. Appl. Phys. **106**, 043520 (2009).

[181] P. Boolchand, D. G. Georgiev, and M. Micoulaut, "Nature of glass transition in chalcogenides," J. Optoelectron. Adv. Mater. **4**, 823-836 (2002).

[182] D. A. P. Bulla, R. P. Wang, A. Prasad, A. V. Rode, S. J. Madden, and B. Luther-Davies, "On the properties and stability of thermally evaporated Ge-As-Se thin films," Appl. Phys. A: Mater. Sci. Process. **96**, 615-625 (2009).

[183] X. Q. Su, R. P. Wang, B. Luther-Davies, and L. Wang, "The dependence of photosensitivity on composition for thin films of $Ge_xAs_ySe_{1-x-y}$ chalcogenide glasses," Appl. Phys. A **113**, 575-581 (2013).

[184] P. Khan, H. Jain, and K. V. Adarsh, “Role of Ge:As ratio in controlling the light-induced response of *a*-$Ge_xAs_{35-x}Se_{65}$ thin films” Sci. Rep. **4**, 4029 (2014).

[185] J. D. Musgraves, S. Danto, and K. Richardson, “Thermal properties of chalcogenide glasses,” in *Chalcogenide glasses: preparation, properties and applications*, J. L. Adam, and X. H. Zhang (ed.) (Woodhead Publishing, Cambridge, 2014).

[186] R. P. Wang, C. J. Zha, A. V. Rode, S. J. Madden, and B. Luther-Davies, “Thermal characterization of Ge-As-Se glasses by differential scanning calorimetry,” J. Mater. Sci.: Mater. Electron. **18**, S419-S422 (2007).

[187] M. Tatsumisago, B. L. Halfpap, J. L. Green, S. M. Lindsay, and C. A. Angell, “Fragility of Ge-As-Se glass-forming liquids in relation to rigidity percolation, and the Kauzmann paradox,” Phys. Rev. Lett. **64**, 1549-1552 (1990).

[188] C. T. Moynihan, A. J. Easteal, J. Wilder, and J. Tucker, “Dependence of the glass transition temperature on heating and cooling rate,” J. Phys. Chem. **78**, 2673-2677 (1974).

[189] L. M. Wang, V. Velikov, and C. A. Angell, “Direct determination of kinetic fragility indices of glassforming liquids by differential scanning calorimetry: Kinetic versus thermodynamic fragilities,” J. Chem. Phys. **117**, 10184-10192 (2002).

[190] K. J. Crowley, and G. Zografi, “The use of thermal methods for predicting glass-former fragility,” Thermochim. Acta **380**, 79-93 (2001).

[191] R. P. Wang, A. Smith, B. Luther-Davies, H. Kokkonen, and I. Jackson, “Observation of two elastic thresholds in $Ge_xAs_ySe_{1-x-y}$ glasses,” J. Appl. Phys. **105**, 056109 (2009).

[192] Y. Yang, B. Zhang, A. P. Yang, Z. Y. Yang, and P. Lucas, “Structural origin of fragility in Ge-As-S glasses investigated by calorimetry and Raman spectroscopy,” J. Phys. Chem. B **119**, 5096-5101 (2015).

[193] J. C. Mauro, Y. Z. Yue, A. J. Ellison, P. K. Gupta, and D. C. Allan, “Viscosity of glass-forming liquids,” Proc. Natl. Acad. Sci. U. S. A. **106**, 19780-19784 (2009).

[194] C. A. Angell, “Relaxation in liquids, polymers and plastic crystals –

strong/fragile patterns and problems," J. Non-Cryst. Solids **131-133**, 13-31 (1991).

[195] F. H. Stillinger, "Supercooled liquids, glass transitions, and the Kauzmann paradox," J. Chem. Phys. **88**, 7818-7825 (1988).

[196] R. Golovchak, A. Kovalskiy, O. Shpotyuk, and H. Jain, "In search of energy landscape for network glasses,"Appl. Phys. Lett. **98**, 171905 (2011).

[197] A. Feltz, *Amorphous Inorganic Materials and Glasses*, (Wiley-VCH, New York, 1993).

[198] P. Lucas, E. A. King, Y. Gueguen, J. C. Sangleboeuf, V. Keryvin, R. G. Erdmann, G. Delaizir, C. Boussard-Pledel, B. Bureau, X. H. Zhang, and T. Rouxel, "Correlation between thermal and mechanical relaxation in chalcogenide glass fibers," J. Am. Ceram. Soc. **92**, 1986-1992 (2009).

[199] R. Böhmer, K. L. Ngai, C. A. Angell, and D. J. Plazek, "Nonexponential relaxations in strong and fragile glass formers," J. Chem. Phys. **99**, 4201-4209 (1993).

[200] L. M. Martinez, and C. A. Angell, "A thermodynamic connection to the fragility of glass-forming liquids," Nature **410,** 663-667 (2001).

[201] D. Y. Choi, S. Madden, A. Rode, R. P. Wang, and B. Luther-Davies, "Fabrication of low loss $Ge_{33}As_{12}Se_{55}$ (Amtir-1) planar waveguides," Appl. Phys. Lett. **91**, 011115 (2007).

[202] J. E. K. Schawe, "A comparison of different evaluation methods in modulated temperature DSC," Thermochim. Acta **260**, 1-16 (1995).

[203] J. M. Hutchinson, A. B. Tong, and Z. Jiang, "Aging of polycarbonate studied by temperature modulated differential scanning calorimetry," Thermochim. Acta **335**, 27-42 (1999).

[204] J. E. K. Schawe, "Modulated temperature DSC measurements: the influence of the experimental conditions," Thermochim. Acta **271**, 127-140 (1996).

[205] J. E. K. Schawe, "Principles for the interpretation of modulated temperature DSC measurements. Part 1. Glass transition," Thermochim. Acta **261**, 183-194 (1995).

[206] O. Gulbiten, J. C. Mauro, and P. Lucas, "Relaxation of enthalpy fluctuations during sub-T_g annealing of glassy selenium," J. Chem. Phys. **138**, 244504 (2013).

[207] G. Yang, O. Gulbiten, Y. Gueguen, B. Bureau, J. C. Sangleboeuf, C. Roiland, E. A. King, and P. Lucas, "Fragile-strong behavior in the As_xSe_{1-x} glass forming system in relation to structural dimensionality," Phys. Rev. B **85**, 144107 (2012).

[208] S. Chakravarty, D. G. Georgiev, P. Boolchand, and M. Micoulaut, "Ageing, fragility and the reversibility window in bulk alloy glasses," J. Phys.: Condens. Matter **17**, L1-L7 (2005).

[209] P. Chen, P. Boolchand, and D. G. Georgiev, "Long term aging of selenide glasses: evidence of sub-T_g endotherms and pre-T_g exotherms," J. Phys.: Condens. Matter **22**, 065104 (2010).

[210] L. Calvez, Z. Y. Yang, and P. Lucas, "Light-induced matrix softening of Ge-As-Se network glasses," Phys. Rev. Lett. **101**, 177402 (2008).

[211] O. Shpotyuk, A. Kozdras, R. Golovchak, and M. Iovu, "Is the marginality of non-reversible heat flow in MDSC experiments a sufficient criterion for self-organization in network glass-formers?" Phys. Status Solidi C **8**, 3043-3046 (2011).

[212] H. He, and M. F. Thorpe, "Elastic properties of glasses," Phys. Rev. Lett. **54**, 2107-2110 (1985).

[213] K. Tanaka, "Elastic properties of covalent glasses," Solid State Commun. **60**, 295-297 (1986).

[214] J. Y. Duquesne, and G. Bellessa, "Ultrasonic study of percolation rigidity in Se-Ge glasses," Euorphys. Lett. **9**, 453-458 (1989).

[215] K. Tanaka, "Medium-range structure in chalcogenide glasses," Jpn. J. Appl. Phys. **37**, 1747-1753 (1998).

[216] M. Popescu, "Modelling of the structure and structural transformations in amorphous chalcogenides," J. Optoelectron. Adv. Mater. **3**, 279-286 (2001).

[217] A. Srinivasan, K. Ramesh, K. N. Madhusoodanan, and E. S. R. Gopal, "High-pressure studies on the critical composition in Ge-As-Te glasses," Philos.

Mag. Lett. **65**, 249-253 (1992).

[218] A. Srinivasan, K. N. Madhusoodanan, and E. R. Gopal, “Observation of a threshold behavior in the optical band gap and thermal diffusivity of Ge-Sb-Se glasses,” Phys. Rev. B **45**, 8112-8115 (1992).

[219] A. N. Sreeram, A. K. Varshneya, and D. R. Swiler, “Molar volume and elastic properties of multicomponent chalcogenide glasses,” J. Non-Cryst. Solids **128**, 294-309 (1991).

[220] L. Tichý, and H. Tichá, “Is the chemical threshold in certain chalcogenide glasses responsible for the threshold at the mean coordination number of approximately 2.7?” Philos. Mag. B **79**, 373-380 (1999).

[221] L. Tichý, and H. Tichá, “On the chemical threshold in chalcogenide glasses,” Mater. Lett. **21**, 313-319, (1994)

[222] S. Asokan, M. V. N. Prasad, G. Parthasarathy, and E. S. R. Gopal, “Mechanical and chemical thresholds in IV-VI chalcogenide glasses,” Phys. Rev. Lett. **62**, 808-810 (1989).

[223] W. H. Wei, L. Fang, X. Shen, and R. P. Wang, “Transition threshold in $Ge_xSb_{10}Se_{90-x}$ glasses,” J. Appl. Phys. **115**, 113510 (2014).

[224] S. Mahadevan, and A. Giridhar, “Coexistence of topological and chemical effects in Ge-Ga-Se glasses,” J. Non-Cryst. Solids **152**, 42-49 (1993).

[225] W. H. Wang, “The elastic properties, elastic models and elastic perspectives of metallic glasses,” Prog. Mater. Science **57**, 487-656 (2012).

[226] P. Lucas “Mean coordination and topological constraints in chalcogenide network glasses,” in *Chalcogenide glasses: preparation, properties and applications*, J. L. Adam, and X. H. Zhang (ed.) (Woodhead Publishing, Cambridge, 2014).

[227] F. Smektala, C. Quemard, L. Leneindre, J. Lucas, A. Barthélémy, and C. De Angelis, “Chalcogenide glasses with large non-linear refractive indices,” J. Non-Cryst. Solids **239**, 139-142 (1998).

[228] C. Quémard, F. Smektala, V. Couderc, A. Barthélémy, and J. Lucas, “Chalcogenide glasses with high non linear optical properties for

telecommunications," J. Phys. Chem. Solids **62**, 1435-1440 (2001).

[229] J. M. Harbold, F. Ö. Ilday, F. W. Wise, J. S. Sanghera, V. Q. Nguyen, L. B. Shaw, and I. D. Aggarwal, "Highly nonlinear As-S-Se glasses for all-optical switching," Opt. Lett. **27**, 119-121 (2002).

[230] J. M. Harbold, F. Ö. Ilday, F. W. Wise, and B. G. Aitken, "Highly nonlinear Ge-As-Se and Ge-As-S-Se glasses for all-optical switching," IEEE Photon. Technol. Lett. **14**, 822-824 (2002).

[231] X. Gai, Y. Yu, B. Kuyken, P. Ma, S. J. Madden, J. V. Campenhout, P. Verheyen, G. Roelkens, R. Baets, and B. Luther-Davies, "Nonlinear absorption and refraction in crystalline silicon in the mid-infrared," Laser Photon. Rev. **7**, 1054-1064 (2013).

[232] C. C. Yang, A. Villeneuve, G. I. Stegeman, C. H. Lin, and H. H. Lin, "Anisotropic two-photon transitions in GaAs/AlGaAs multiple quantum well waveguides," IEEE J. Quantum Electron. **29**, 2934-2939 (1993).

[233] J. S. Aitchison, M. K. Oliver, E. Kapon, E. Colas, and P. W. E. Smith, "Role of two-photon absorption in ultrafast semiconductor optical switching devices," Appl. Phys. Lett. **56**, 1305-1307 (1990).

[234] M. Pelusi, F. Luan, T. D. Vo, M. R. E. Lamont, S. J. Madden, D. A. Bulla, D. Y. Choi, B. Luther-Davies, and B. J. Eggleton, "Photonic-chip-based radio-frequency spectrum analyser with terahertz bandwidth," Nature Photon. **3**, 139-143 (2009).

[235] M. D. Pelusi, F. Luan, E. Magi, M. R. E. Lamont, D. J. Moss, B. J. Eggleton, J. S. Sanghera, L. B. Shaw, and I. D. Aggarwal, "High bit rate all-optical signal processing in a fiber photonic wire," Opt. Express **16**, 11506-11512 (2008).

[236] M. El-Amraoui, G. Gadret, J. C. Jules, J. Fatome, C. Fortier, F. Désévédavy, I. Skripatchev, Y. Messaddeq, J. Troles, L. Brilland, W. Gao, T. Suzuki, Y. Ohishi, and F.Smektala, "Microstructured chalcogenide optical fibers from As_2S_3 glass: towards new IR broadband sources," Opt. Express **18**, 26655-26665 (2010).

[237] X. Gai, D. Y. Choi, S. Madden, and B. Luther-Davies, "Interplay between

Raman scattering and four-wave mixing in As_2S_3 chalcogenide glass waveguides,” J. Opt. Soc. Am. B **28**, 2777-2784 (2011).

[238] S. J. Madden, D. Y. Choi, D. A. Bulla, A. V. Rode, B. Luther-Davies, V. G. Ta’eed, M. D. Pelusi, and B. J. Eggleton, “Long, low loss etched As_2S_3 chalcogenide waveguides for all-optical signal regeneration,” Opt. Express **15**, 14414-14421 (2007).

[239] N. Hô, J. M. Laniel, R. Vallée, and A. Villeneuve, “Photosensitivity of As_2S_3 chalcogenide thin films at 1.5μm,” Opt. Lett. **28**, 965-967 (2003).

[240] J. J. Wynne, “Optical third-order mixing in GaAs, Ge, Si, and InAs,” Phys. Rev. **178**, 1295-1303 (1969).

[241] C. C. Wang, “Empirical relation between the linear and the third-order nonlinear optical susceptibilities ,” Phys. Rev. B. **2**, 2045-2048 (1970).

[242] N. L. Boling, A. J. Glass, and A. Owyoung, “Empirical relationships for predicting nonlinear refractive index changes in optical solids,” IEEE J. Quantum Electron. **QE-14**, 601-608 (1978).

[243] K. Petkov, and P. J. S. Ewen, “Photoinduced changes in the linear and non-linear optical properties of chalcogenide glasses,” J. Non-Cryst. Solids **249**, 150-159 (1999).

[244] H. Tichá, and L. Tichý, “Semiempirical relation between non-linear susceptibility (refractive index), linear refractive index and optical gap and its application to amorphous chalcogenides,” J. Optoelectron. Adv. Mater. **4**, 381-386 (2002).

[245] H. Kanbara, S. Fujiwara, K. Tanaka, H. Nasu, and K. Hirao, “Third-order nonlinear optical properties of chalcogenide glasses,” Appl. Phys. Lett. **70**, 925-927 (1997).

[246] G. Boudebs, F. Sanchez, J. Troles, and F. Smektala, “Nonlinear optical properties of chalcogenide glasses: comparison between Mach-Zehnder interferometry and Z-scan techniques,” Opt. Commun. **199**, 425-433 (2001).

[247] C. Monat, M. Spurny, C. Grillet, L. O’Faolain, T. F. Krauss, B. J. Eggleton, D. Bulla, S. Madden, and B. Luther-Davies, “Third-harmonic generation in

slow-light chalcogenide glass photonic crystal waveguides," Opt. Lett. **36**, 2818-2820 (2011).

[248] R. A. Norwood, "Four wave mixing," in *Characterization techniques and tabulations for organic nonlinear optical materials,* M. G. Kuzyk, and C. W. Dirk (ed.) (Marcel Dekker Inc, New York, 1998).

[249] R. L. Sutherland, *Handbook of nonlinear optics*, Second edition (Marcel Dekker Inc, New York, 2003).

[250] M. Sheik-Bahae, A. A. Said, T. H. Wei, D. J. Hagan, and E. W. Van stryland, "Sensitive measurement of optical nonlinearities using a single beam," IEEE J. Quantum Electron. **26**, 760-769 (1990).

[251] K. A. Cerqua-Richardson, J. M. McKinley, B. Lawrence, S. Joshi, and A. Villeneuve, "Comparison of nonlinear optical properties of sulfide glasses in bulk and thin film form," Opt. Mater. **10**, 155-159 (1998).

[252] J. Troles, F. Smektala, G. Boudebs, and A. Monteil, "Third order nonlinear optical characterization of new chalcohalogenide glasses containing lead iodine," Opt. Mater. **22**, 335-343 (2003).

[253] G. Lenz, J. Zimmermann, T. Katsufuji, M. E. Lines, H. Y. Hwang, S. Spälter, R. E. Slusher, S.-W. Cheong, J. S. Sanghera, and I. D. Aggarwal, "Large Kerr effect in bulk Se-based chalcogenide glasses," Opt. Lett. **25**, 254-256 (2000).

[254] S. X. Dai, F. F. Chen, Y. S. Xu, Z. Xu, X. Shen, T. F. Xu, R. P. Wang, and W. Ji, "Mid-infrared optical nonlinearities of chalcogenide glasses in Ge-Sb-Se ternary system," Opt. Express **23**, 1300-1307 (2015).

[255] L. Y. Chen, F. F. Chen, S. X. Dai, G. M. Tao, L. H. Yan, X. Shen, H. L. Ma, X. H. Zhang, and Y. S. Xu, "Third-order nonlinearity in Ge-Sb-Se glasses at mid-infrared wavelengths," Mater. Res. Bull.**70**, 204-208 (2015).

[256] M. Sheik-bahae, D. J. Hagan, and E. W. Vanstryland, "Dispersion and band-gap scaling of the electronic Kerr effect in solids associated with two-photon absorption," Phys. Rev. Lett. **65**, 96-99 (1990).

[257] M. Dinu, "Dispersion of phonon-assisted nonresonant third-order nonlinearities," IEEE J. Quantum Electron. **39**, 1498-1503 (2003).

[258] W. H. Wei, R. P. Wang, X. Shen, L. Fang, and B. Luther-Davies, “Correlation between structural and physical properties in Ge-Sb-Se glasses,” J. Phys. Chem. C **117**, 16571-16576 (2013).

[259] R. Adair, L. L. Chase, and S. A. Payne, “Nonlinear refractive index of optical crystals,” Phys. Rev. B **39**, 3337-3350 (1989).